From graphene synthesis to applications

Claudia Cirillo

Unione Europea

*Ministero dell'Istruzione,
dell'Università e della Ricerca*

UNIVERSITÀ DEGLI
STUDI DI SALERNO

Department of Industrial Engineering

*Ph.D. Course in Chemical Engineering
(XII Cycle-New Series)*

FROM GRAPHENE SYNTHESIS TO APPLICATIONS

Supervisor   **Ph.D. student**
Prof. Maria Sarno   *Claudia Cirillo*

Scientific Referees
Prof. Paolo Ciambelli
Prof. Adolfo Senatore
Prof. Massimiliano Polichetti

Ph.D. Course Coordinator
Prof. Paolo Ciambelli

Acknowledgements

It is always a great pleasure to acknowledge people who have inspired, motivated and supported me by sharing their knowledge and wisdom.

First and foremost I want to thank my advisor Professor Maria Sarno for her teachings, guidance and encouragement during these past three years. I have always admired her extraordinary energy and enthusiasm in everything that she does. It has been an honor to be her first Ph.D. student.

I would like to thank Professor Paolo Ciambelli for his precious teachings and advises received in these years. He is an amazing scientist and mentor.

Many thanks to Professor Adolfo Senatore, member of my Ph.D. committee, for the tribological tests and for the stimulating discussions. His support and helpful suggestions were deeply welcome.

Thanks so much to Professor Massimiliano Polichetti, member of my Ph.D. committee, for the magnetic measurements and fruitful discussions. His academic support and his comments were greatly appreciated.

I sincerely thank Professor Stefano Riemma for his advices throughout my Ph.D. career.

Finallly, thanks to my lab-mates, T3 and T1, for contributing to achieve this result with support and friendship.

Publications list

- P. Ciambelli, M. Sarno, C. Leone, C. Cirillo, "The effect of the critical parameters on the CCVD growth of graphene on Ni foil". AIRI/Nanotech IT - Veneto Nanotech - CNR – IIT - The annual Italian showcase for Nanotechnologies - Nanotechitaly 2011. 287-288 Nanotechitaly 2011. Venezia, Italy, November 23 – 25, 2011 ISBN: 9788660750275

- M. Sarno, C. Cirillo, C. Leone, R. Piscitelli, P. Ciambelli, "Study of the process parameters on the CCVD growth of graphene on Cu foil", Book of Abstract Granada'12; 9-13 September 2012. Edited by Blanca Biel, Marıa J. Lopez and Elvira Romera Copyright: Universidad de Granada Deposito Legal: GR 2550-2012. pag. 89. ISBN: 978-84-695-4635-2

- M. Sarno, C. Cirillo, C. Leone, R. Piscitelli, P. Ciambelli, "Reaction yield and H_2 crucial role, for the uniform graphene growth on Ni foil", Proceedings of the International Conference on Diamond and Carbon Materials, Granada, Spain, September 3 – 6, 2012

- M. Sarno, C. Cirillo, P. Ciambelli "Nanoparticelle magnetiche ricoperte di grafene per applicazioni biomediche", Convegno GRICU 2012, Montesilvano (PE), Italy, September 16 – 19, 2012

- M. Sarno, C. Cirillo, C. Altavilla, R. Piscitelli, P. Ciambelli, "Synthesis of carbon nanomaterials for healthcare, energy, electronics and other applications", Nanotechitaly 2012

- M. Sarno, C. Cirillo, R. Piscitelli, P. Ciambelli, "A study of the key parameters, including the crucial role of H_2 for uniform graphene growth on Ni foil" Journal of Molecular Catalysis A: Chemical 366 (2013) 303– 314

- V. D'Agostino, A. Senatore, V. Petrone, P. Ciambelli, M. Sarno, C. Cirillo, "On the friction reduction mechanism introduced by graphene nanosheets as additive in oil lubricated contacts" World Tribology Congress 2013 Torino, Italy, September 8 – 13, 2013

- M. Sarno, A. Senatore, C. Cirillo, V. Petrone, P. Ciambelli, "Oil Lubricant Tribological Behaviour Improvement Through Dispersion of Few Layer Graphene Oxide", Journal of Nanoscience and Nanotechnology 14 (2014) 4960 – 4968

- P. Ciambelli, M. Sarno, A. Senatore, C. Cirillo, V. Petrone, S. Iandoli, "Graphene versus graphite based oil friction modifiers" Nanotech Italy 2013 - Venezia, Italy, November 27 – 29, 2013

- M. Sarno, C. Cirillo, P. Ciambelli, "Selective graphene covering of monodispersed magnetic nanoparticles", Chemical Engineering Journal Accepted (2013)

- M. Sarno, M. Polichetti, C. Cirillo, P. Ciambelli, "Superparamagnetic core-shell graphene coated Co/Fe synthesized nanoparticles", Submitted to Journal of Nanoscience and Nanotechnology (2014)

Contents

IV

List of Figures

List of Table

XII

Abstract

Graphene is the first two-dimensional (2D) atomic crystal available to us. Since its discovery in 2004, graphene has captured the attention and the imagination of worldwide researchers thank to its supreme properties.

Catalytic chemical vapour deposition (CCVD) is a widely employed method to synthesize large areas graphene on metal foil or to cover nanoparticles (NPs) with carbon coating. Exfoliation of graphite is largely used for the massive production of flakes of graphene.

In such light, this thesis work has been focused to develop industrial scalable processes starting from research at lab scale on graphene formation.

The first part of investigation has been addressed to fabrication of high-quality graphene films on Ni foil using CVD at ambient pressure. Critical parameters including Ni thickness, cooling rate, and polycrystalline crystallographic orientation have been explored to understand the graphene formation mechanism and to obtain controlled carbon growth. We have studied the effect of operating conditions such as the synthesis time and feed composition, as well as the key role played by H_2.

The placement of graphene on arbitrary substrates is key for applications. A study of graphene transfer from metal foil on specific support was also realized.

Subsequently, core-shell few layer-graphene-coated metal nanoparticles (GCMNP) were synthesized by CVD. Different synthesis operating conditions were investigated to achieve a good control over the coverage of GCMNPs and to understand the mechanism of GCMNP formation and carbon coverage. The reactor outlet gas was continuously monitored on-line during the catalyst activity. Several techniques were utilized to characterize the catalyst and the reaction products and to correlate their properties with the reactor operating conditions.

Magnetic properties of the core-shell few layer graphene-coated magnetic nanoparticles were also studied.

Parallel, few layer graphene oxide (GO) nanosheets were prepared by a very fast modified Hummers method and largely characterized. The tribological behaviour of GO in mineral oil was investigated under a wide spectrum of conditions.

Finally, the preparation of graphene and multilayer graphene sheets by liquid phase graphite exfoliation in N-methylpyrrolidone (NMP) was carried out. A one step massive very pure thin flakes production with an high monolayer yield was obtained.

XIV

Objectives

The goal of the research has been to develop industrial scalable processes starting from research at lab scale on graphene formation. To this purpose different techniques for graphene formation have been studied. In particular, the targets have been:

(i) Preparation of high quality graphene (ordered structure, omogeneity and controlled number of layers) on a low-cost commercial polycrystalline Ni foil using chemical vapor deposition (CVD) at ambient pressure.

(ii) Investigation of transfer techniques of graphene film on specific support.

(iii) Synthesis process analysis, with particular attention to the specific applications.

(iv) Preparation of high quality (controlled size, structure, selective covering, controlled number of carbon layer) graphene coated magnetic nanoparticles.

(v) Preparation of graphene flakes from graphite exfoliation for massive production using two different graphite exfoliation methods (Hummers method and liquid phase exfoliation).

Collaborations

Tribological tests have been conducted with the collaboration of Professor Adolfo Senatore at Laboratory I6 at Department of Industrial Engineering of University of Salerno.

Magnetic measurements have been conducted with the collaboration of Professor Massimiliano Polichetti, at Laboratory LAMBDA at Department of Physics of University of Salerno.

Introduction

Graphene is a two dimensional material consisting of a single layer of carbon atoms arranged in a honeycomb structure. It is the thinnest material known and yet is also one of the strongest. Graphene is almost completely transparent, so dense that even the smallest atom helium cannot pass through it. In 2004, the first graphene was extracted from graphite using a technique called micromechanical cleavage "Novoselov et al (2007)". This approach allowed easy production of high-quality graphene crystallites and further led to enormous experimental activities "Katsnelson (2007)".

Over the past few years research on graphene increased dramatically because of new methods to produce and study it. Since then researchers have proposed uses for graphene ranging from flexible touch screens to ultracapacitors to transistor. Many of these proposals rely on graphene grown via chemical vapor deposition (CVD), the most promising technique for producing large-area deposition. Once synthesized, CVD graphene can be transferred to suitable substrates, making the technique versatile for many applications.

Graphene can be achieved through other different methods, like mechanical exfoliation using "scotch tape method", chemical oxidation/exfoliation adding to graphite several chemicals, liquid-phase exfoliation of graphite exposing the materials to a solvent.

Depending on the specific application can be used single- or few-layer graphene. Therefore, alternative techniques for graphene formation have been studied.

Both the CVD technique that the exfoliation of graphite are used in industries. The first one for the production of large areas of graphene to be transferred onto substrates (microelectronics, solar cells, displays, etc....), the second one for the massive production of flakes of graphene to be added for example in polymers or oil lubricants for tribology applications.

Besides the applications of graphene, integration of nanoparticles (NPs) and graphene into nanocomposites has recently become a hot topic of research due to their new and/or enhanced functionalities that cannot be achieved by either component alone, and therefore holds great promise for a wide variety of applications in catalysis, optoeletronic materials, biomedical fields, and so on. Among them are nanocomposites of magnetic NPs (MNPs) for potential applications in enhanced optical limiting, MRI, drug delivery, energy storage

and removal of contaminants from wastewater. Different carbon coating strategies have been developed. CVD technique offers the advantage of being the easiest to scale up towards an economically viable production.

Chapter I
Background

I.1 Carbon Allotropes

Carbon is the element in the periodic table that provides the basis for life on Earth. It is also important for many technological applications, ranging from drugs to synthetic materials. This role is a consequence of carbon's ability to bind to itself and to nearly all elements in almost limitless variety. The resulting structural diversity of organic compounds and molecules is accompanied by a broad range of chemical and physical properties "Hirsch (2010)".
Carbon, one of the most common element on Earth, occurs naturally in many forms and as a component in countless substances.

Carbon has long been known to exist in three forms, namely, amorphous carbon, graphite, and diamond (Figure I.1) "Dai et al. (2012)".
Depending on how the carbon atoms are arranged, their properties vary. For example, graphite is soft and black and the stable, common form of carbon with strong covalent bonding in the carbon plane and the much weaker van der Waals interactions in the transverse direction between the layers (Figure I.1 a). Graphite's common usage is as the core of a pencil, where flakes of graphite slide off the bulk material and remain as a mark on paper.

Diamond is hard and transparent with each carbon atom bound to four other carbon atoms in a regular lattice (Figure I.1 b). It is constituted by a crystal lattice of carbon atoms arranged in a tetrahedral structure. Each carbon atom thus forms four covalent bonds with four neighboring atoms, completely filling its outer electron shell and resulting in one of the hardest and most valued substances in human history.
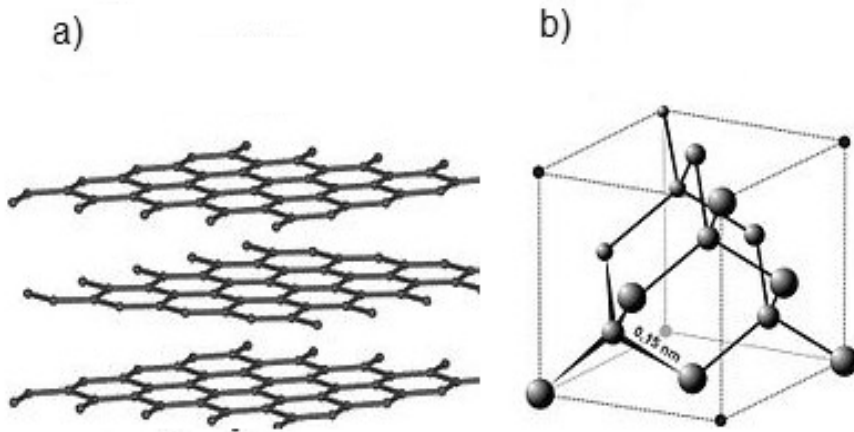
Figure I.1 *Images of crystal structure of: graphite (a) and diamond (b)*

But, in the last decade, three nanoscale forms of carbon have attracted widespread attention because of their novel properties: buckyballs, carbon nanotubes, and graphene.

A buckyball is created by collapsing yet another dimension. A buckyball is a small segment of a carbon nanotube that has been pinched together at both ends to form a hollow sphere of carbon atoms. The 60-carbon buckyball was the first carbon nanomaterial to gain widespread attention.

Carbon-60 (C60) is probably the most studied individual type of nanomaterial. The spherical shape of C60 is constructed from twelve pentagons and twenty hexagons and resembles a soccer ball. Buckyballs have many proposed uses, such as for example encapsulation of reactive compounds in chemistry.

Carbon nanotubes (CNTs) are another allotrope of carbon. They can be thought of as ribbons of graphene that have been rolled into a tube. Due to the strength of the bonds in a hexagonal carbon lattice, nanotubes are one of the strongest fibers ever discovered.

Actually the most recent carbon nanomaterial to be widely studied is graphene. Its basic structure is very simple: it is formed by a 6-carbon ring of

2

atoms, and then tessellate that hexagon to form a two dimensional (2D) hexagonal honeycomb lattice. Such a 2D sheet is known as graphene.

Graphene's properties are striking in a number of respects, but probably most notable is that a single graphene sheet is quite stable and mechanically resilient, as well as very electrically conductive.

Graphene is the building block for carbon nanotubes and buckyball "Geim and Novoselov (2007)".

Fullerene, or buckyball, is formed by wrapping up graphene into zero dimensional (0D) buckyball; carbon nanotube is formed by rolling up graphene into 1D cylinder and graphite is formed by stacking graphene into 3D structure (Figure I.2). For example, the crystalline form of graphite consists of many graphene sheets stacked together.
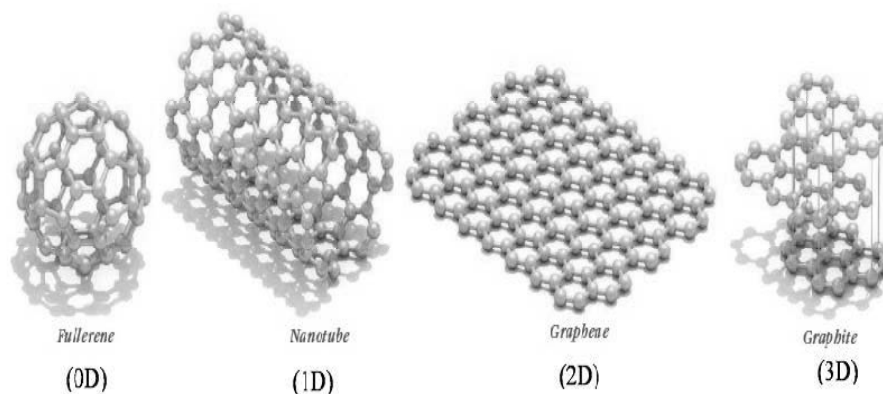
Figure I.2 *Carbon allotropes from 0D to 3D*

Graphene-like structures were already known of since the 1960's "Boehm et al. (1962), Van Bommel et al. (1975), Forbeaux et al. (1998), Oshima et al. (2000)" but there were experimental difficulties in isolating single layers in such a way that electrical measurements could be performed on them, and there were doubts that this was practically possible.

It is interesting to consider that everyone who has used an ordinary pencil has probably produced graphene-like structures without knowing it. A pencil contains graphite, and when it is moved on a piece of paper, the graphite is cleaved into thin layers that end up on the paper and make up the text or

drawing that we are trying to produce. A small fraction of these thin layers will contain only a few layers or even a single layer of graphite, *i.e.* graphene.

Thus, the difficulty was not to fabricate the graphene structures, but to isolate sufficiently large individual sheets in order to identify and characterize the graphene and to verify its unique two-dimensional (2D) properties. This is what Geim, Novoselov, and their collaborators succeeded in doing .

Chapter II
Graphene

II.1 Graphene

Graphene is the name given to a flat monolayer of carbon atoms tightly packed into a two-dimensional (2D) honeycomb lattice, and is a basic building block for graphitic materials of all other dimensionalities (Figure II.1) "Geim and Novoselov (2007)".

The term graphene was coined in 1962 as a combination of graphite and the suffix -ene by Hanns-Peter Boehm and described single-layer carbon foils. The crystalline or "flake" form of graphite consists of many graphene sheets stacked together.

In 2004 physicists at the University of Manchester and the Institute for Microelectronics Technology, Chernogolovka, Russia, first isolated individual graphene planes by using adhesive tape. They also measured electronic properties of the obtained flakes and showed their unique properties.

The Royal Swedish Academy of Sciences has awarded the Nobel Prize in Physics for 2010 to Andre Geim and Konstantin Novoselov, both of the University of Manchester, "*for groundbreaking experiments regarding the two-dimensional material graphene*".

A thin flake of ordinary carbon, just one atom thick, lies behind Nobel Prize in Physics. Geim and Novoselov have shown that carbon in such a flat form has exceptional properties that originate from the remarkable world of quantum physics.

Geim and Novoselov extracted the graphene from a piece of graphite such as is found in ordinary pencils. Using regular adhesive tape they managed to obtain a flake of carbon with a thickness of just one atom. This at a time when many believed it was impossible for such thin crystalline materials to be stable.
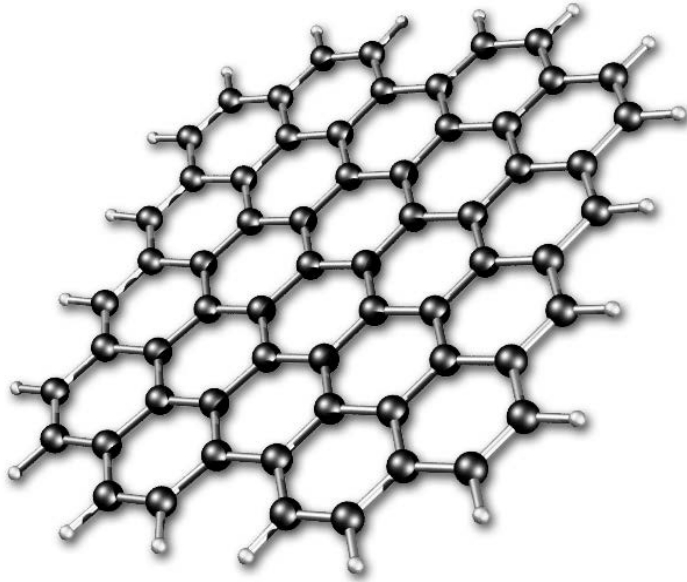
Figure II.1 *Structure of graphene: an atomic-scale honeycomb lattice made of carbon atoms*
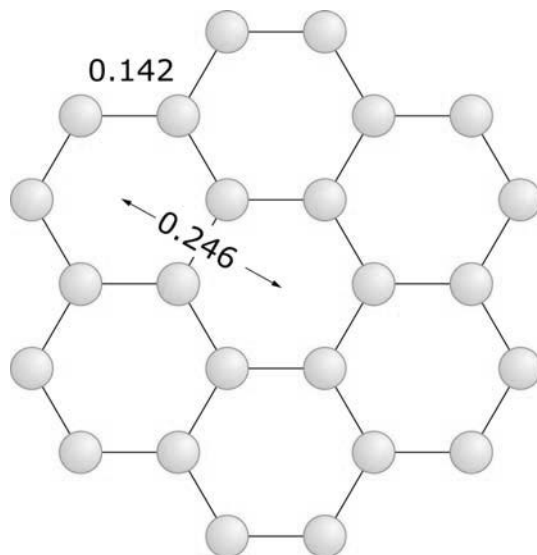
Figure II.2 *The honeycomb atomic lattice structure*

However, with graphene, it's possible to study a new class of two-dimensional materials with unique properties. Also a vast variety of practical applications now appear possible including the creation of new materials and the manufacture of innovative electronics.

Since it is practically transparent and a good conductor, graphene is suitable for producing transparent touch screens, light panels, and maybe even solar cells.

When mixed into plastics, graphene can turn them into conductors of electricity while making them more heat resistant and mechanically robust. This resilience can be utilized in new super strong materials, which are also thin, elastic and lightweight. In the future, satellites, airplanes, and cars could be manufactured out of the new composite materials.

II.2 Atomic Structure

In graphene, carbon atoms are arranged in a honeycomb lattice with angles of 120° as shown in Figure II.2. The carbon-carbon bond length in graphene is about 0.142 nanometers. We can see this atomic arrangement as a combination of benzene rings with a center-to-center distance of 0.246 nanometers.

Graphene sheets stack to form graphite with an interplanar spacing of 0.335 nm, which means that a stack of three million sheets would be only one millimeter thick.

II.3 Properties of graphene

Properties of graphene are determined mainly by its structural conformation, in particular by two unique features that affect its properties and material make it truly extraordinary. The first is the structural perfection: it is formed only by carbon atoms joined together by strong bonds and at the same time flexible, forming a crystalline structure practically, completely free of defects such as atoms out of place or missing. The second peculiarity is that the electrons behave as massless particles, such as photons, with an extremely high electron mobility (μ), equal to 15000 $cm^2 \cdot V^{-1} \cdot s^{-1}$ at room temperature. This makes this unique nanomaterial and suitable for many innovative applications "Geim and Novoselov et al. (2007)".

II.3.1 Density of graphene

The unit hexagonal cell of graphene contains two carbon atoms and has an area of 0.052 nm^2. Thus, its density is 0.77 mg/m^2 "Nobel Physics Laureates (2010)".

II.3.2 Electronics properties

One of the most useful properties of graphene is that it is a zero-overlap semimetal (with both holes and electrons as charge carriers) with very high electrical conductivity. Carbon atoms have a total of 6 electrons; 2 in the inner shell and 4 in the outer shell. The 4 outer shell electrons in an individual carbon atom are available for chemical bonding, but in graphene, each atom is connected to 3 other carbon atoms on the two dimensional plane, leaving 1 electron freely available in the third dimension for electronic conduction. These highly-mobile electrons are called pi (π) electrons and are located above and below the graphene sheet. These pi orbitals overlap and help to enhance the carbon to carbon bonds in graphene. Fundamentally, the electronic properties of graphene are dictated by the bonding and anti-bonding (the valance and conduction bands) of these pi orbitals.

Combined research over the last 50 years has proved that at the Dirac point in graphene, electrons and holes have zero effective mass. This occurs because the energy – movement relation (the spectrum for excitations) is linear for low energies near the 6 individual corners of the Brillouin zone. These electrons and holes are known as Dirac fermions, or Graphinos, and the 6 corners of the Brillouin zone are known as the Dirac points. Due to the zero density of states at the Dirac points, electronic conductivity is actually quite low. However, the Fermi level can be changed by doping (with electrons or holes) to create a material that is potentially better at conducting electricity than, for example, copper at room temperature "Geim and Novoselov (2007)".

II.3.3 Mechanical Properties

Another of graphene's stand-out properties is its inherent strength. Due to the strength of its 0.142 Nm-long carbon bonds, graphene is the strongest material ever discovered, with an ultimate tensile strength of 130,000,000,000 Pascals (or 130 gigapascals), compared to 400,000,000 for A36 structural steel, or 375,700,000 for Aramid (Kevlar). Not only is graphene extraordinarily strong, it is also very light at 0.77 milligrams per square metre (for comparison purposes, 1 square metre of paper is roughly 1000 times heavier). It is often said that a single sheet of graphene (being only 1 atom thick), sufficient in size enough to cover a whole football field, would weigh under 1 single gram.

What makes this particularly special is that graphene also contains elastic properties, being able to retain its initial size after strain. In 2007, atomic force microscopic (AFM) tests were carried out on graphene sheets that were suspended over silicone dioxide cavities. These tests showed that graphene sheets (with thicknesses of between 2 and 8 Nm) had spring constants in the region of 1-5 N/m and a Young's modulus (different to that of three-dimensional graphite) of 0.5 TPa. Again, these superlative figures are based on theoretical prospects using graphene that is unflawed containing no imperfections whatsoever and currently very expensive and difficult to artificially reproduce, though production techniques are steadily improving, ultimately reducing costs and complexity "Geim and Novoselov (2007)".

II.3.4 Optical Properties

Graphene's ability to absorb a rather large 2.3% (97.7% transmittance) of white light is also a unique and interesting property, especially considering that it is only 1 atom thick. This is due to its aforementioned electronic properties; the electrons acting like massless charge carriers with very high mobility. A few years ago, it was proved that the amount of white light absorbed is based on the Fine Structure Constant, rather than being dictated by material specifics. Adding another layer of graphene increases the amount of white light absorbed by approximately the same value (2.3%). Due to these impressive characteristics, it has been observed that once optical intensity reaches a certain threshold (known as the saturation fluence) saturable absorption takes place (very high intensity light causes a reduction in absorption). This is an important characteristic with regards to the mode-locking of fibre lasers. Due to graphene's properties of wavelength-insensitive ultrafast saturable absorption, full-band mode locking has been achieved using an erbium-doped dissipative soliton fibre laser capable of obtaining wavelength tuning as large as 30 nm.

In terms of how far along we are to understanding the true properties of graphene, this is just the tip of the iceberg. Before graphene is heavily integrated into the areas in which we believe it will excel at, we need to spend a lot more time understanding just what makes it such an amazing material. Unfortunately, while we have a lot of imagination in coming up with new ideas for potential applications and uses for graphene, it takes time to fully appreciate how and what graphene really is in order to develop these ideas into reality. This is not necessarily a bad thing, however, as it gives us opportunities to stumble over other previously under-researched or overlooked super-materials, such as the family of 2D crystalline structures that graphene has born "Bonaccorso et al. (2010)".

9

II.3.5 Thermal Properties

Graphene is a perfect thermal conductor. Its thermal conductivity was measured recently at room temperature and it is much higher than the value observed in all the other carbon structures as carbon nanotubes, graphite and diamond (> 5000 W/mK).

The ballistic thermal conductance of graphene is isotropic, i.e. same in all directions. Similarly to all the other physical properties of this material, its 2 dimensional structure make it particularly special. Graphite, the 3D version of graphene, shows a thermal conductivity about 5 times smaller (1000 W m^{-1} K^{-1}). The phenomenon is governed by the presence of elastic waves propagating in the graphene lattice, called phonons.

The study of thermal conductivity in graphene may have important implications in graphene-based electronic devices. As devices continue to shrink and circuit density increases, high thermal conductivity, which is essential for dissipating heat efficiently to keep electronics cool, plays an increasingly larger role in device reliability "Zhu et al. (2010b)"

II.3.6 Chemical properties

Similar to the surface of graphite, graphene can adsorb and desorb various atoms and molecules (for example, NO_2, NH_3, K, and OH).

Weakly attached adsorbates often act as donors or acceptors and lead to changes in the carrier concentration, so graphene remains highly conductive. This can be exploited for applications as sensors for chemicals.

Other than weakly attached adsorbates, graphene can be functionalized by several chemical groups (for instances OH^-, F^-) forming graphene oxide and fluorinated graphene. It has also been revealed that single-layer graphene is much more reactive than 2, 3 or higher numbers or layers.

Also, the edge of graphene has been shown to be more reactive than the surface. Unless exposed to reasonably harsh reaction conditions, graphene is a fairly inert material, and does not react readily despite every atom being exposed and vulnerable to its surrounding "Bonaccorso et al. (2010)"

II.4 Applications of graphene

The extraordinary properties of graphene, carbon sheets that are only one atom thick, have caused researchers to consider using this material in many technology areas. Some of these are:

(i) Graphene-based electronics and optoelectronics, partially replacing conventional siliconbased electronics, because graphene has ultrafast terahertz electron mobility that gives it a very bright future for building smaller, faster, cheaper electronic devices such as ballistic transistors "Liang et al. (2007)", spintronics "Yazyev et al. (2008)", field effect transistors "Meric et al. (2008)", and optoelectronics "Bonaccorso et al. (2010)".

(ii) Graphene filled polymer composites with high electrical and thermal conductivity, good mechanical strength, and low percolation threshold, which, in combination with low-cost and largescale production, allow a variety of performance-enhanced multifunctional use in electrically conductive composites, thermal interface materials, etc. "Dikin et al. (2007), Stankovich et al. (2006)".
 Large-area CVD-grown graphene that is suitable to replace indium tin oxide (ITO) as cheaper, transparent conducting electrodes in various display applications such as touch screens, which is considered to be one of the immediate applications in a few years "Kim et al. (2009), Bae et al. (2010)".

(iii) Another advantage over ITO is that ITO suffers from being brittle and is incapable of bending, which does not allow it to meet the requirements for flexible devices, while graphene is a more competitive solution for flexible, transparent and processable electrodes.

(iv) Graphene-based electrochemical storage energy devices such as high-performance Lithium Ion Batteries (LIBs) and ElettroCapacitors (ECs) because of their greatly improved electrochemical performance of capacity, cyclability and rate capability due to its unique 2D structure and excellent physiochemical properties "Chen et al. (2008)".

(v) Recent research indicates many other potential applications in bio-, electrochemical, and chemical sensors "Pumera (2009)", dye-sensitized solar cells "Wang et al. (2008)", organic solar cells "Wang et al. (2008)", field emission devices "Wu et al. (2009)", catalysts "Lightcap et al. (2010)" and photocatalysts "Williams et al. (2008)", nanogenerators "Choi et al. (2010)", hydrogen storage "Ma et al. (2009)", etc.
 Graphene may offer other advantageous properties that outperform those of CNT and graphite, resulting in the development of new and unexpected applications.

II.5 Outlook and future challenges

The successful introduction of graphene in products depends on the ability to make any of the materials in large quantities at a reasonable cost. The progress in developing new materials processes over the past few years has been impressive, especially given the broad materials requirements, from single crystal graphene to graphene flakes. The suitability of any given process depends on the application "Bonaccorso et al. (2012)".

Nanoelectronics more than likely has the most demanding requirements, i.e. low defect density single crystals. Other applications, such as biosensors, may require defective graphene, while printable electronics can tolerate lower quality, e.g. lower mobility, graphene. Chemical vapor deposition techniques is an ideal processes for large area graphene films, for example, for touch screen and other large display applications, while graphene derived from SiC single crystals maybe better suited for resistor standards, and high frequency device applications. However, it is desirable to grow graphene directly on dielectric surfaces for many device applications . But, a lot more effort is required to achieve large area uniform high quality graphene films on dielectrics. Liquid phase exfoliation is appealing for the preparation of inks, thin films and composites, and future research is needed to control on-demand the number of layers, flake thickness and lateral size, as well as rheological properties. The layered nature of graphite makes its integration with other layered materials a natural way to create heterostructures. Layered materials have been around for a long time and studied and developed mostly for their tribological properties. Now they are being considered as new interlayer dielectrics for heterostructures that have potential for new electronic devices with exotic properties. Because of their potential for new devices, there will be a host of new processes that will need to be developed in order to grow or deposit high quality large area monolayer films, integrated with graphene, with controlled thickness and transport properties "Bonaccorso et al. (2012)".

Chapter III
Synthesis and characterization of graphene

III.1 Graphene production

The methods of preparation for graphene can be divided into two categories, top-down and bottom-up ones. The top-down methods include (i) mechanical exfoliation and (ii) chemical oxidation/exfoliation. The bottom-up methods include (i) epitaxial growth on SiC and other substrates, (ii) Chemical vapor deposition.

Each of these methods has some advantages and limitations. Among them chemical synthesis of graphene using graphite, graphite oxide (GO) is a scalable process but it leads to more defect in the graphene layer.

Currently, there are probably a dozen methods being used and developed to prepare graphene of various dimensions, shapes and quality.

The main synthesis techniques are described in the following.

III.1.1 Micromechanical Cleavage

The reason for the popularity of graphene in the last few years lies in how simple it is to make. Anyone with a pencil, a roll of scotch tape and a silicon wafer can start doing original experiments. In the same way that a pencil can be used to draw on paper, very thin graphite flakes can be exfoliated onto a substrate.

This technique, shown in Figure III.1 (a,b,c), involves the repeated pealing of layers of graphite. An adhesive tape is used to peel off layers from the surface of HOPG and subsequent peeling eventually leads to a single layer of graphite on the surface of a substrate like silicon oxide. Single layers of sizes up to 10 μm in size and thicker multilayer films (two or more layers) of around 100μm have been reported "Novoselov (2004)".

The yield of single layers obtained by this technique is very low (a few graphene monolayers per mm^2 of substrate area). Research on improving the yield of exfoliated single layers have led to many variants of the exfoliation technique "Liang et al. (2007)", "Song et al. (2009)". However, the size and yield of single layer graphene still remains a bottleneck in this process.
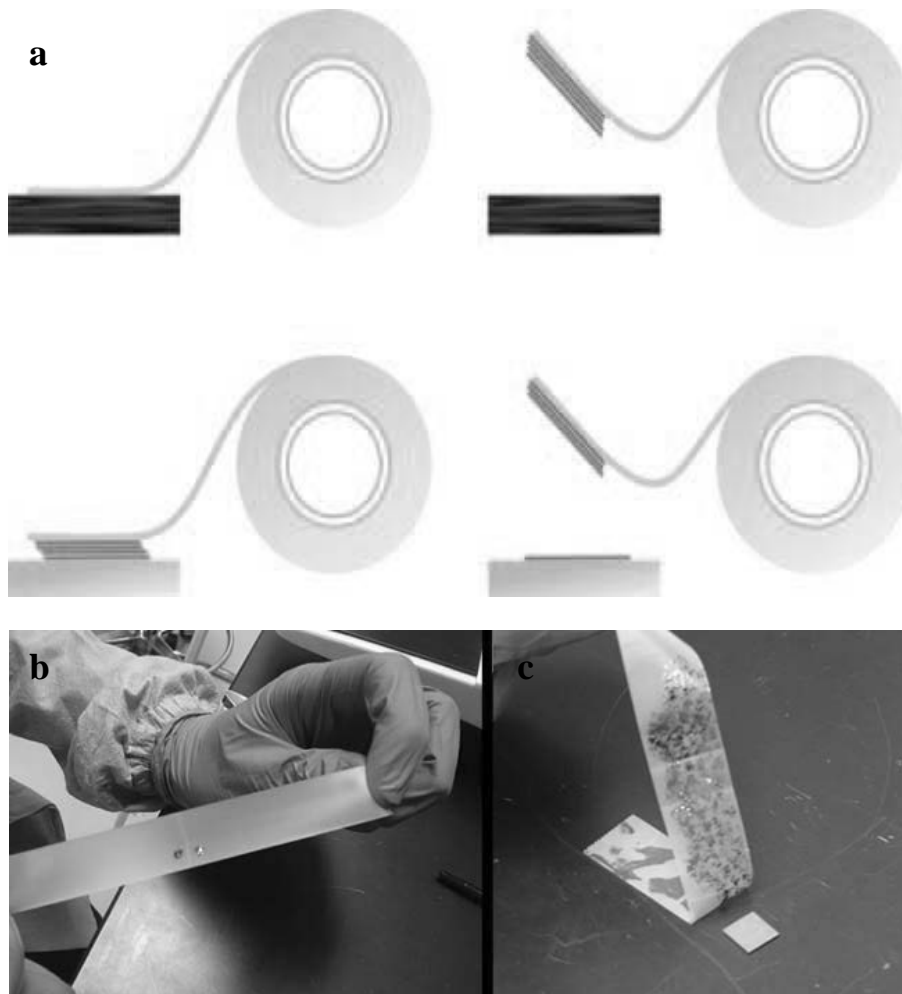
Figure III.1 *Scheme of the micromechanical cleavage technique ('Scotch tape' method) for producing graphene "Novoselov (2011)"(a), Images of: graphite flake cleaved by Scotch tape (b) tape covered with graphite pressed down on silicon wafer (c)*

III.1.2 Epitaxial Graphene from Silicon Carbide

Growth of graphitic thin films on silicon carbide is well known "Van Bommel et al. (1975), Mrtensson and Owman (1996)".

Specifically they grow on the 0001 (silicon-terminated) and 0001 (carbonterminated) faces of 4H- and 6H-SiC crystals upon heating to about 1300 °C in ultra-high vacuum (UHV). It is also possible to grow these films under less demanding vacuum conditions using ovens with controlled

background gas. This technique, however, does not produce atomically thin single graphene layers, rather it produces epitaxially ordered stacks of graphene.

Although the graphene obtained in the way is not structurally perfect, it shows electrical properties comparable to that of mechanically exfoliated graphene "Berger et al. (2006)".

In order to grow homogeneous mono- and few-layer graphene on SiC(0001), a suitable approach is to anneal the SiC samples at temperatures above 1600°C in an Ar atmosphere in a quartz glass reactor "Emtsev et al. (2009)". Furthermore, it has recently been demonstrated that it is also possible to grow graphene on both SiC faces with an additional carbon supply similar to molecular beam epitaxy using relatively low temperatures of around 950°C "Al-Temimy et al. (2009)".

III.1.3 Graphene oxide

The synthesis of graphene oxide, usually performed by Hummers and Offeman method "Hummers and Offeman (1958)", implies the use of one or more strong acids and an oxidizing agent. The method consists in oxidation of graphite powder, followed by exfoliation by sonication. The resulted graphene oxide is a sheet of graphene having covalently attached hydroxyl, epoxy and carbonyl groups on basal planes, and carboxyl and carbonyls – at margins, as presented in Figure III.2.

The oxidation of graphite in the presence of acids and oxidants, proposed in the nineteenth century "Brodie (1860)", disrupts the sp^2 network and introduces hydroxyl or epoxide groups "Mattevi et al. (2009), Cai et al. (2008)" with carboxylic or carbonyl groups attached to the edges. These make graphene oxide sheets readily dispersible in water and several other solvents. Although large flakes can be obtained, these are intrinsically defective and electrically insulating. Despite several attempts "Stankovich et al. (1958), Mattevi et al. (2009)" reduced graphene oxide does not fully regain the pristine graphene electrical conductivity "Mattevi et al. (2009), Eda et al. (2008)"

It is therefore important to distinguish between dispersion processed graphene flakes, which retain the electronic properties of graphene, and insulating graphene oxide layers.
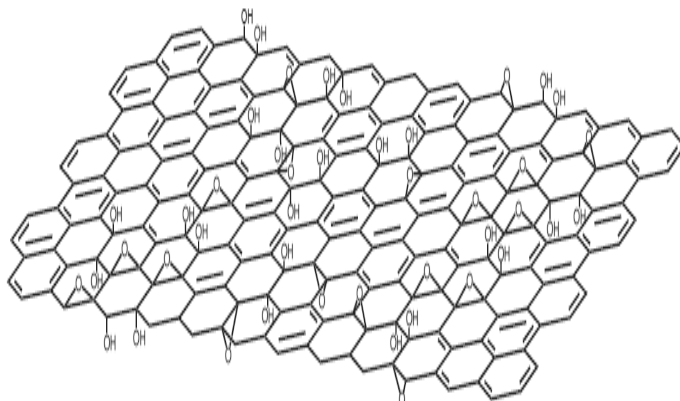
Figure III.2 *Chemical structure of graphite oxide*

III.1.4 Chemical Exfoliation

To achieve high quality results using a process that could be mass produced, chemical exfoliation of graphite to produce graphene monolayers have been explored "Hernandez et al. (2008)".

Liquid-phase exfoliation is based on exposing the materials to a solvent with a surface tension that favours an increase in the total area of graphite crystallites. Typically, the solvent is non-aqueous, but aqueous solutions with surfactant can also be used.

The role of the solvent is crucial, since n-Methyl-Pyrrolidone (NMP) has a strong interaction with the honeycomb lattice, thus easily infiltrating between the planes facilitating their exfoliation. Other similar solvents were tried by the group, but NMP resulted the one with the highest yield of single layer flakes. The method (Figure III.3) is really simple and clean, since it does not involve modification of the chemical composition of graphite, and residual solvent evaporates without remarkable traces. Produced solutions provide a ratio of mono-layers over multilayers of ~ 1 wt%, ending in relatively large flakes.

Previously, other methods such as intercalation (injecting atoms between graphite layers to peel them apart) "Viculis et al. (2003)", ultrasonic heating "Chen et al. (2004)" and acid treatment "Li et al. (2008)" have produced monolayer hexagonal carbon, generally produced nanoribbons (thin flat graphene wires), not full graphene sheets.
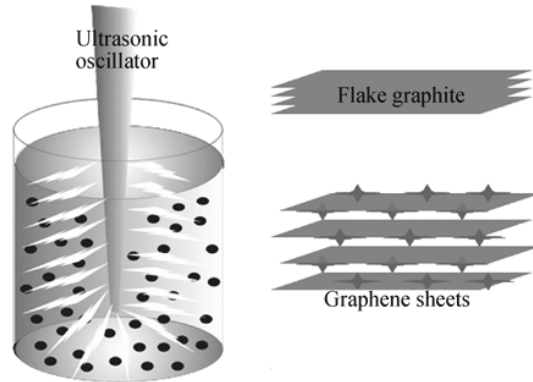
Figure III.3 *Liquid-phase exfoliation of graphite method*

III.1.5 Graphene grown on transition metal surfaces using Chemical Vapour Deposition (CVD)

Chemical vapor deposition (CVD) is an alternative method to mechanical exfoliation and it's used to obtain high quality graphene for large-scale production of mono or few layer graphene films on metal substrate. CVD is widely used in the microelectronics industry in processes involving the deposition of thin films of various materials. The deposition is made from precursors in the gas phase which adsorb on the target surface producing a condensed phase of a specific material. The attractiveness of the generation of graphene by CVD is based on the fact that this technique allows for scalability as well as low cost. A schematic experimental set-up is shown in Figure III.4. The process begins with an atomically flat surface of a transition metal substrate and an appropriate carbon precursor (like in methane or ethylene). The metal substrate plays the role of catalyst. This substrate is placed in a heated furnace and is attached to a gas delivery system. The precursor molecules will be brought into contact with the substrate surface from the gas phase or from liquid phase at elevated temperature. Upon contact with the surface, the precursor molecules are cracked to form carbon atoms and form gas-phase species, leaving the carbon atoms (which are free of functionalities) attached to the substrate surface. Graphene is formed when carbon atoms after diffusion on the metal surface, encounter other carbon atoms and form bonds.

Optimization of this process over the years has triggered interest in growth of graphene on relatively inexpensive polycrystalline Ni "Kim et al. (2009)", "Obraztsov et al. (2007)", "Reina et al. (2009)" and Cu "Li et al. (2009)". substrates.

17
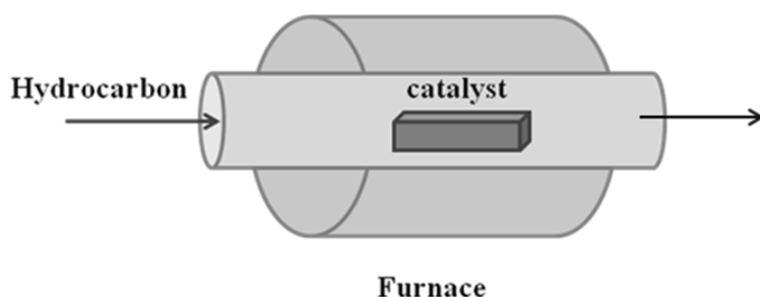
Figure III.4 *Scheme of the growth process for the synthesis of graphene using CVD*

III.2 Transfer of graphene grown on metals

Bae et al. "Bae et al. (2010)", in 2010, first reported the transfer of single layer graphene (SLG) and few layer graphene (FLG) grown on Ni, by depositing a PMMA sacrificial layer and subsequently etching the underlying Ni by aqueous HCl solution "Bae et al. (2010)". Li et al. transferred films grown by CVD on Cu, etched by iron nitrate "Li et al. (2009)". Kim et al. introduced etching by aqueous $FeCl_3$ in order to remove Ni without producing hydrogen bubbles, which may damage graphene when acid etching is used "Kim et al. (2009)".

They also reported a technique where PDMS stamps are attached directly to the graphene surface. Ni is then chemically etched by $FeCl_3$ leaving graphene attached to the Polydimethylsiloxane (PDMS). Graphene is then transferred to SiO_2 by pressing and peeling the PDMS stamp. Bae et al. "Bae et al. (2010)" also introduced roll-to-roll transfer of graphene grown by CVD on Cu foils as large as 30 x 30in^2, guided through a series of rolls: a thermal release tape was attached to the Cu+graphene foil, and then an etchant, an aqueous 0.1 M ammonium persulphate solution $(NH_4)_2S_2O_8$, removed Cu (Fugure III.5).

The tape+graphene film was then attached to a (flexible) target substrate and the supporting tape removed by heating, thus releasing graphene onto the target substrate "Bae et al. (2010)".

To avoid Fe contamination caused by $FeCl_3$ etching, ammonium persulfate $[(NH_4)_2S_2O_8]$ was used "Aleman et al. (2010)". To avoid mechanical defects caused by roll to roll transfer, a hot pressing process was developed "Kang et al. (2012)": similar to a roll-to-roll process, the Cu+graphene foil is first attached to thermal release tape and then Cu is chemically etched. The tape+graphene foil is then placed on the target substrate and both are subsequently inserted between two hot metal plates with controlled T and pressure. This results in the detachment of the adhesive tape with very low
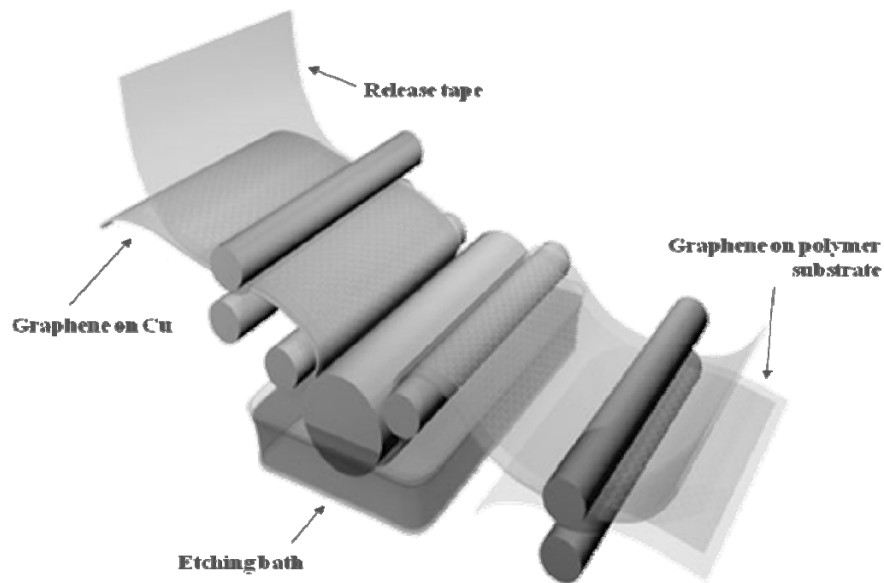
Figure III.5 *Scheme of the graphene transfer process to a substrate "Bae et al.(2010)"*
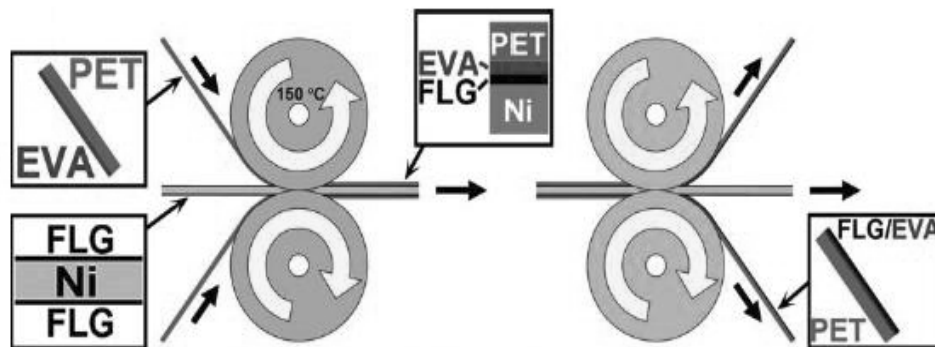
Figure III.6 *Scheme of roll-to-roll process for the transfer of FLG from Ni foil to EVA/PET substrates "Juang et al. (2010)"*

frictional stress, therefore less defects, than a roll-to-roll process "Kang et al. (2012)".

According to Juang et al. "Juang et al. (2010)" roll-to-roll process is an ideal production choice when a very low cost per unit area of deposition is required. In the process for the transfer of few layer graphene to various flexible substrates, shown in Figure III.6, commercial ethylene-vinyl acetate copolymer (EVA) coated transparent polyethylene terephthalate (PET) sheets were used as the target substrate.

At a temperature of 150°C, the EVA/PET and FLG/Ni sheets were pressed together with hot rollers to form a double-sided PET/EVA/FLG/Ni sheet. The EVA layer here plays a role of viscose between the PET and FLG. After the hot rolling step, the sheet was passed onto cold rollers at room temperature. The purpose of the cold rolling step is to separate the PET/EVA/FLG layers from the Ni surface in a uniform manner with a controlled, constant rolling speed.

III.3 Characterization of graphene

There are several techniques to determine the number of layers of graphene product and the size of the flakes. The techniques best suited for characterization of graphene sheets are reported in the following.

III.3.1 Raman spectroscopy

Raman spectroscopy is widely used to identify and characterize all the carbon materials. It is a nondestructive technique, fast, with high resolution and give the maximum structural and electronic information. It has now become a standard technique fundamental for the identification of graphene.

The Raman spectra of these carbon materials are very simple and characterized by few main bands in the region between 1000 and 3000 cm^{-1}, whose position, shape and intensity allow to discriminate between the various types of material (Figure III.7) "Ferrari (2007)". For graphene, the two fundamental peaks are at 1580 cm^{-1}, named G peak, and at 2700 cm^{-1}, named 2D peak and the Raman D peak, is at 1360 cm^{-1}. The G peak is due to the bond stretching of all pairs of sp^2 atoms in both rings and chains, D peak is due to the breathing mode of the carbon atoms of the benzene rings (Figure III.8), and 2D peak represents the second order of the peak D.

Compared to bulk graphite, graphene 2D peak is much more intense and shows a significant change in the shape.

The 2D peak in bulk graphite consists of two components "Ferrari et al. (2006)". Graphene has a single, sharp 2D peak, roughly four times more intense than the G peak "Ferrari et al. (2006)".

20

2D peak also allows to determine the number of graphene layers: layer going from single to double layer it decreases in intensity and becomes about ⅔ of the peak G; gradually increasing the layers changes the shape and the position of the peak: bi-layer graphene has a much broader and upshifted 2D band with respect to graphene, that is different from bulk graphite. Evolution of G peak as a function of number of layers is shown in Figure III.9.

Therefore, Raman spectroscopy is able to identify a single layer, from bi-layer from few layers.
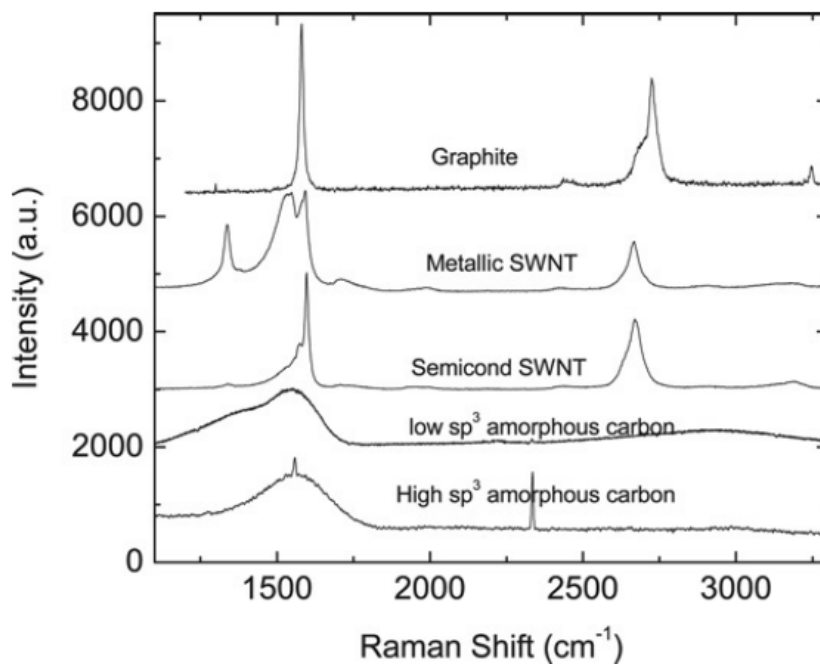
Figure III.7 *Raman spectra of different carbon materials, "Ferrari (2007)"*
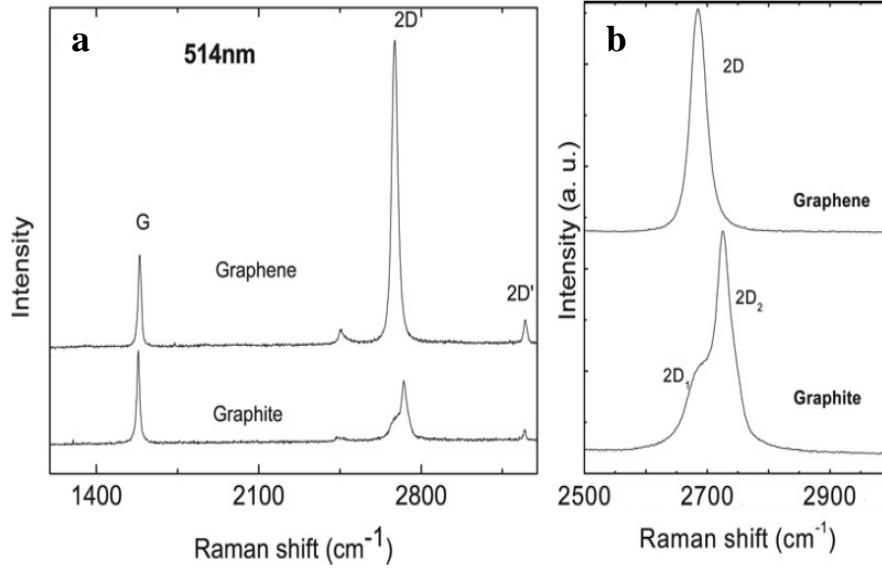
Figure III.8 *Comparison of the Raman spectra of graphene and graphite (a) Comparison of the 2D peaks in graphene and graphite (b),"Ferrari (2007)"*
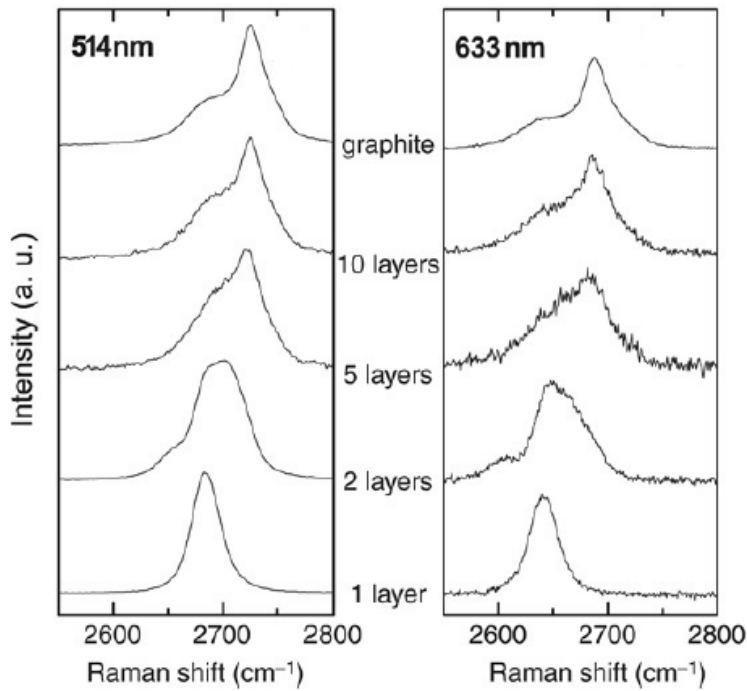
Figure III.9 *Evolution of G peak as a function of number of layers for 514 and 633 nm excitations, "Ferrari (2007)"*

III.3.2 Transmission Electron Microscopy (T.E.M)

Transmission Electron Microscopy is a technique able to evaluate the size of the graphene sheets and the number of layers. In order to study the graphitic structure and layer stacking, electron diffraction (ED) patterns are recorded. The Figure III.10 shows the typical T.E.M. image of a single layer graphene with an electron diffraction pattern.

III.3.3 Scanning electron microscopy (SEM)

Scanning Electron Microscopy technique can give qualitative insight into the three-dimensional structure of graphene sheets as illustrated in Figure III.11.
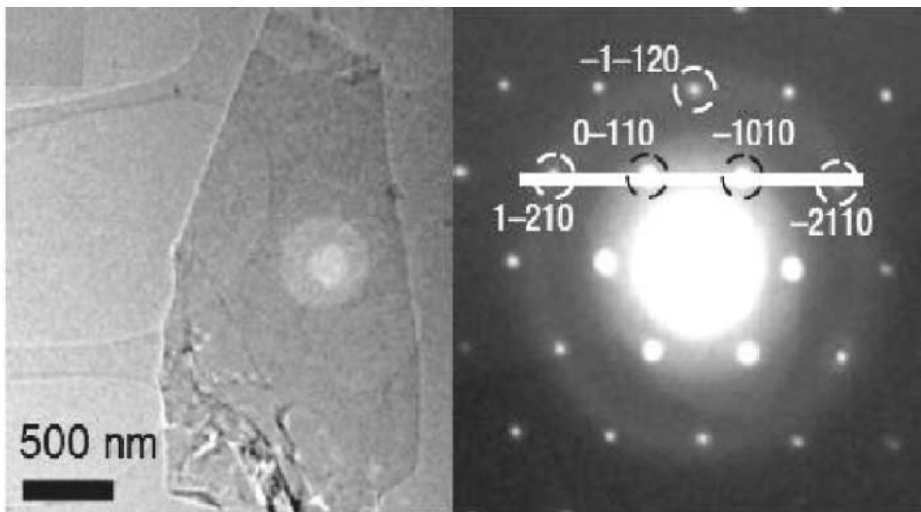
Figure III.10 *TEM image of a single layer graphene with an electron diffraction pattern with Miller-Bravais indices "Hernandez et al. (2008)"*
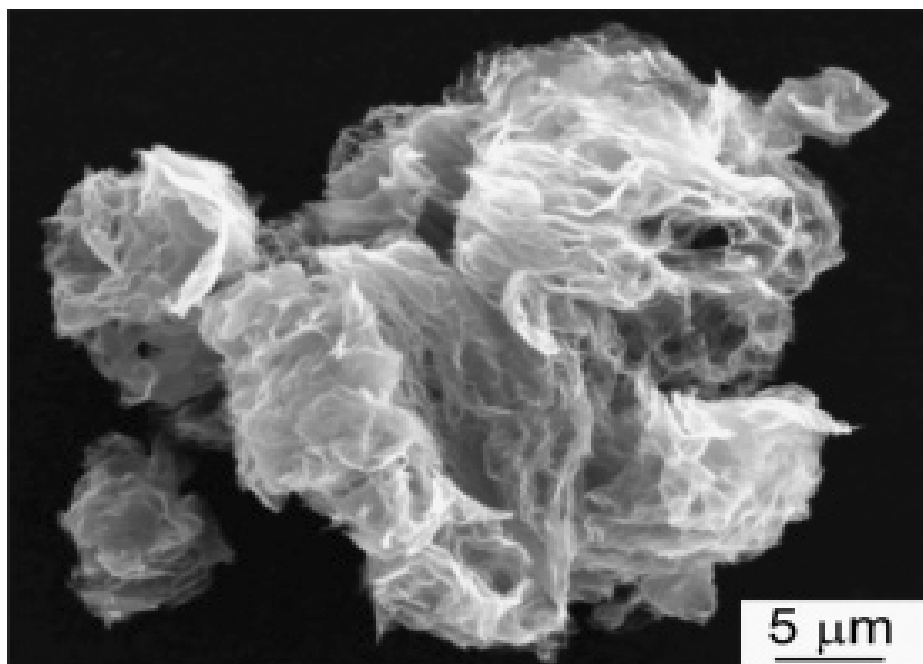
Figure III.11 *SEM image of thermally reduced graphene oxide sheets "McAllister et al. (2007)"*

III.3.4 Atomic Force Microscopy (AFM)

Atomic Force Microscopy (AFM) imaging provides more reliable measures of sheet dimensions. Contact or tapping mode AFM can be used to probe surface topology, defects, and bending properties "Schniepp et al. (2006)". Folded or wrinkled sheets as well as adsorbed solvents or moisture can complicate measurements "Kim et al. (2010)". An AFM analysis on the graphene flake is reported in Figure III.12.
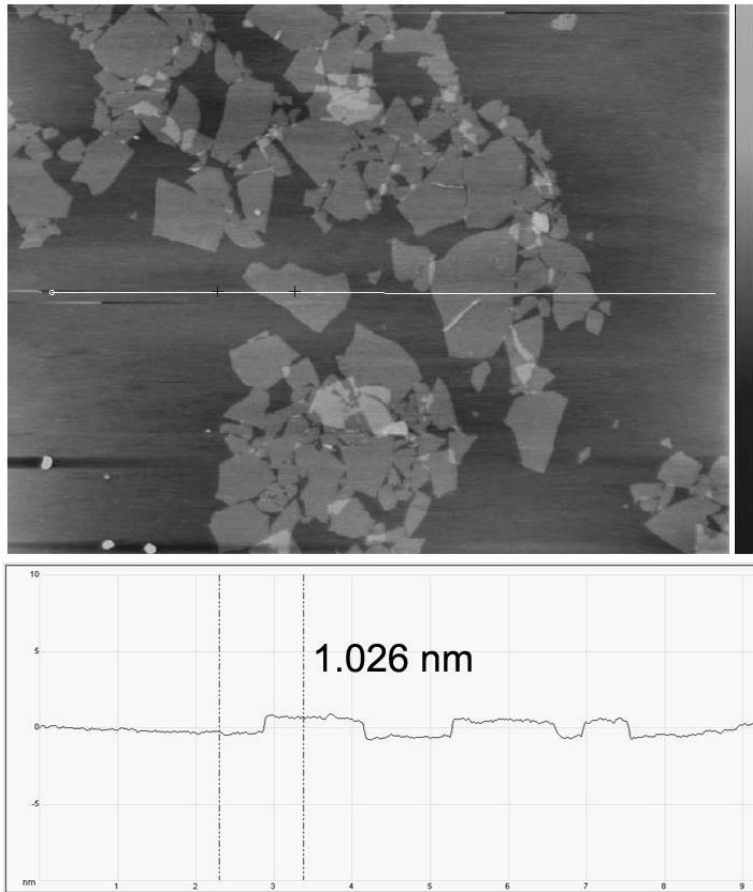
Figure III.12 *AFM analysis on the graphene flakes "Lu et al. (2012)"*

III.3.5 X-ray diffraction

X-ray diffraction is used to demonstrate that graphite has been intercalated. For example, the sharp reflection at $2\theta = 26.3°$ (Cu KR radiation, X-ray wavelength = 0.154 nm) in graphite shifts to 14.1°-14.9° in graphite oxide "Szabo et al. (2006)" (Figure III.13). However, X-ray diffraction disappears as the sheets of GO exfoliate into single sheets "McAllister et al. (2007)".
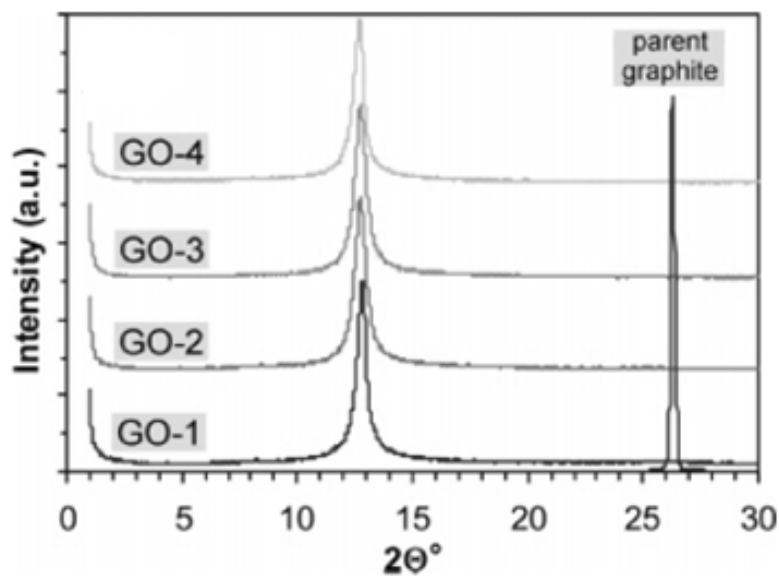
Figure III.13 *XRD pattern for graphite and different type of GO "Szabo et al. (2006)"*

III.3.6 Surface Area

Although indirect, surface area, measured using the Brunauer, Emmett, and Teller (BET) method, has been used as an indicator of exfoliation. Since theoretically the specific surface area is inversely proportional to thickness of disk-like particles, (~2/density/thickness), well-exfoliated sheets will have higher surface area "McAllister et al. (2007)".

Chapter IV
Experimental Plant

IV.1 Introduction

To study graphene growth, a semi-continuous experimental plant was implemented and set up to allow the continuous analysis of gaseous streams containing the carbon source. In the difference from literature, a vertical quartz micro-reactor where a catalyst is crossed by reaction feed was employed. Continuous analysis of gaseous streams, realised with NDIR continuous analysers, permitted to perform carbon mass balance, to evaluate hydrocarbons conversion, the presence of by-products, catalysts performances.

IV.2 Experimental Plant for graphene synthesis

A diagram of the experimental plant for graphene syntheses is shown in Figure IV.1. It consists of three sections:

- feed section
- reaction section
- analysis section

All the gas pipes (¼'' ed) are of Teflon, connections are made with Swagelok union and two, three and four way Nupro valves. All the connections are in stainless steel to avoid any corrosion due to the presence of water in the reaction products.

The feed section allows the feeding of the carbon source using N_2 as the carrier gas. For each gas a mass flow controller (MFC) was used, in order to

assure a constant flow rate. Each gas came from cylinders (SOL SPA) with a high purity degree.

Brooks measured flow controller (MFC) are used, able to operate with a maximum pressure drop of 3 atm. The working principle of the MFC is heat transport: the temperature difference in a capillary, where a part of the gas is split, it is measured. This temperature difference is proportional to the amount of heat adsorbed by the mass gas for the equation:

$$\Delta T = K \cdot C_p \cdot \Phi_m \qquad \text{(IV.1)}$$

where:

ΔT = temperature difference

K = dimensional constant

Cp = specific heat of the gas

Φm = mass flow

The instrument's temperature detector produces an electrical signal from 0 to 5 V (c.c.); this signal is sent to the control unit (MFC C.U.) which converts the signal in volumetric flow. This control unit allows the mass flow of the gases to be regulated.

The reaction section allows the preparation of graphene in a reactor, consisting of a quartz tube of 300 mm length and 16 mm internal diameter. A portion of the reactor, placed in a vertical furnace, was filled with a thin layer of catalyst. An external quartz tube, internal diameter 35 mm, permitted the preheating of the reactants stream. In order to measure the temperature inside the reactor, a thermocouple is placed on a 4 mm internal diameter quartz shield, coaxial to the reactor. The reactor is set in a vertical electrically heated oven. The oven temperature and the control parameters are adjusted by a temperature programmer-controller, connected to a type K thermocouple located inside the reactor. A temperature reader connected to a

second thermocouple measures the temperature of the catalyst inside the reactor.

In the reaction section a system of valves allows the reactants to go to the reactor, and the products to the analysis section, or, in the bypass position, the reactants to the analysis section to verify the reactant composition. In bypass mode an independent line is used to send air or nitrogen to the reactor for the thermal pre-treatment of the catalysts, or to wash the reactor.

In the analysis section continuous analysers (ABB), Figure IV.2, mean that C_2H_4, C_2H_2, CH_4 (URAS 14) and H_2 (Caldos 17) concentrations in the effluent stream on line during the reaction can be monitored.

The URAS 14 (Infrared analyser module) uses a NDIR absorption process, which is based on resonance absorption at the characteristic vibration rotation spectrum bands of non-elemental gases in the middle infrared range. Because of their bipolar moment, the gas molecules interact with infrared emissions. The photometer is characterized by high stability and selectivity.

The analyzer has gas-filled opto-pneumatic detectors which have been optimized for each application. This enables higher sensitivity, a wider range of sample components and reduced cross-sensitivity to interfering components. Detector filling corresponds to the gas being measured. This means that the detector provides optimal sensitivity and high selectivity for the component of interest. Calibration is possible via the internal calibration cells which do not require expensive bottled test gas mixtures. This greatly reduces operation and maintenance costs.

The Thermal conductivity analyzer module Caldos 17 (Figure IV.2) exploits the varying thermal conductivities of different gases. Measurement is carried out by means of a silicon sensor that allows especially rapid measurement and extremely small measuring ranges.
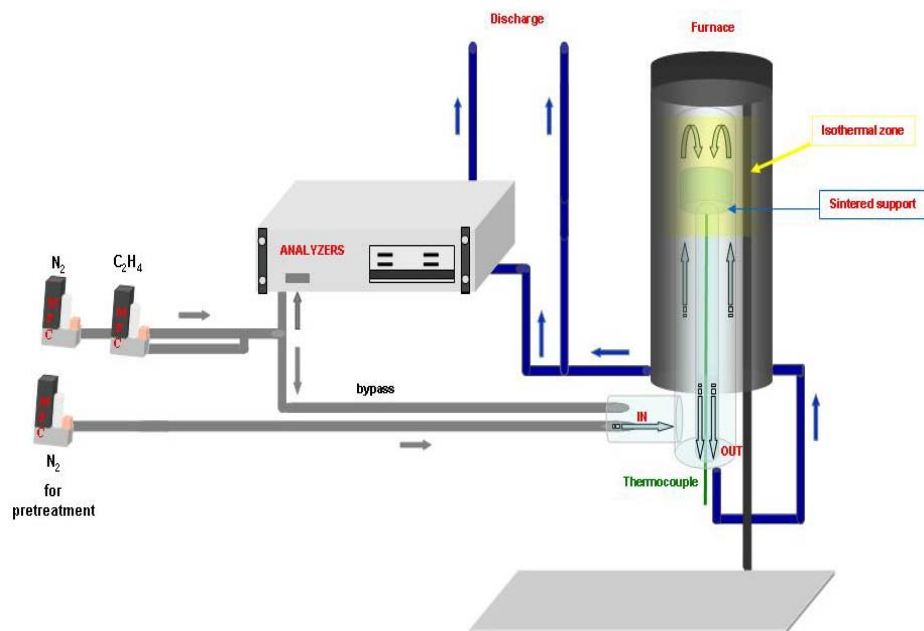
Figure IV.1 *Experimental plant for graphene synthesis*

Figure IV.2 *Uras 14 and Caldos 17 ABB analysers*

Chapter V
Experimental II
Uniform graphene growth on Ni foil

V.1 Introduction

Since the first successful fabrication of graphene by cleavage, three major methods for the fabrication of single-and multi-layer graphene have been investigated. These methods include micromechanical cleavage "Geim and Novoselov (2007)", chemical exfoliation of graphite "Stankovich et al. (2007), Hernandez et al. (2008)", and chemical vapor deposition (CVD) of hydrocarbons on a substrate surface "Kim et al. (2009), Vaari et al. (1997), Starr et al. (2006), Gall'et al. (2004), de Parga et al. (2008), Wintterlin et al. (2009), Johansson et al. (1994), Presland and Walker (1969), Kehrer Jr. et al. (1954), Presland, C. Roscoe, P.L. Walker Jr., in: J.G. Gregory (Ed.), Proc. Third Industrial Carbon and Graphite Conf., Society of Chemical Industry, London, 1971, p. 116, Bernardo et al. (1976), Karu et al. (1966), Derbyshire et al. (1975), Zhu et al. (1989), Reina et al. (2009a), Reina et al. (2009b), Kumar et al. (2010), Zhang et al. (2010), Thiele et al.(2010), Pollard et al. (2009), Park et al.(2010)".

Among them, the latter (CVD growth) is considered to be of the most promising due to its capability of producing large-area deposition, the lack of intense mechanical and/or chemical treatments and its
flexibility. The growth of graphene monolayers on single crystalline transition metals such as Co, Pt, Ir, Ru, Cu and Ni is well known "Vaari et al. (1997), Starr et al. (2006), Gall'et al. (2004), de Parga et al. (2008), Wintterlin et al. (2009)". In CVD the nucleation and growth of graphene usually occurs by exposure of the transition metal surface to a hydrocarbon gas under low pressure or UHV conditions. Growing graphite by using CVD at ambient pressure has long been tried "Johansson et al. (1994), Presland and Walker (1969), Kehrer Jr et al. (1954), Presland, A.E.B. Roscoe, C. Walker P.L. Jr., in: J.G. Gregory (Ed.), Proc. Third Industrial Carbon and Graphite Conf., Society of Chemical Industry, London, 1971, p.116, Bernardo et al. (1976), Karu et al. (1966), Derbyshire et al. (1975), Zhu et al. (1989)", but single-layer graphene has been synthesized by this way only recently on Ni substrates by Reina et al. "Reina et al. (2009a)" and Kim et al. "Kim et al. (2009)" independently.

The literature on this theme can essentially be divided between (i) those in which graphene films were prepared on nickel films "Kim et al. (2009), Reina et al. (2009a), Reina et al. (2009b), Kumar et al. (2010), Zhang et al. (2010), Thiele et al. (2010), Pollard et al. (2009), Park et al. (2010), Obraztsov et al. (2007)" (sputtered or evaporated on substrate), mostly for microelectronic applications, and (ii) those using nickel foils "Yu et al. (2008), Chae et al. (2009), Li et al. (2009)" to obtain very large areas of graphene with which to make transparent electrodes; these could be used as a in substitute for ITO in flat panel displays, liquid crystal displays, touch panels, solar cells and EMI shielding. Each of the papers written supplies a contribution to the interpretation of the reaction mechanism. In particular, specific points in the process are individuated as critical in the formation of the carbon layers: the thickness of the film, the cooling rate, the roughness and crystalline orientation. In a few cases, the synthesis operating conditions were studied too.

In particular, Reina et al. "Reina et al et al. (2009a)", demonstrated for the first time that continuous films of single- to few-layer graphene (1 to ~10 layers) can be grown by ambient pressure CVD on polycrystalline Ni film and transferred to a large variety of substrates. The Ni films, e-beam evaporated onto SiO_2/Si substrate and thermally annealed before the CVD synthesis, were exposed to a highly diluted hydrocarbon/H2 flow at 900–1000 ∘C under ambient pressure. Graphene films were prepared by Kim et al. "Kim et al. (2009)" at 1000 °C, under a (CH_4/H_2/Ar = 50/65/200) flowing gas mixture. They found that a fast cooling rate is critical for suppressing the formation of multiple layers and for separating graphene layers efficiently from the substrate in the later process steps. To avoid the formation of thick graphite crystals rather than graphene films, they deposited thin layers of nickel less than 300 nm thick on SiO_2/Si substrates using an electron-beam evaporator.

Reina et al. "Reina et al. (2009b)" showed the possibility of growing graphene film at high concentration on Ni substrate by controlling the carbon concentration and the substrate cooling rate during the CVD process.

Kumar et al. "Kumar et al. (2010)" gives an interpretation of the catalytic role of the support (a thin Ni film), identifying the two phases of hetero-epitaxial and homo-epitaxial carbon layer deposition. They demonstrated the absence of catalyst segregation in the formation of graphene layers, based on the consideration that the solubility of carbon in Ni is less than 1% at 950°C.

By comparing the behavior of single and poly-Ni crystal (mostly (1 1 1), Zhang et al. concluded that the formation of mono- bi-layer graphene is due to the substrate smoothness "Zhang et al. (2010)".

The same conclusion is reported in Thiele et al. "Thiele et al. (2010)", thermal annealing process to increase the nickel grain size that has limited 1–2-layer graphene areas was investigated. After thermal annealing, only the

(1 1 1) diffraction peak, showing a smaller mismatch in the epitaxial growth of graphene, was detected "Wintterlin et al. (2009), Obraztsov et al. (2007)". In the paper by Yu et al. "Yu et al. (2008) graphene synthesis was performed on a Ni foil with a thickness of 0.5 mm under CH_4:H_2:Ar = 0.15:1:2 at 1000 °C. They studied the effect of the cooling rate on the thickness of the graphene layers grown by a surface segregation process.

Chae et al. "Chae et al. (2009)" reported on the growth of large-area graphene at optimized CVD conditions on poly-Ni foils. Under these conditions (1 1 0) is the most abundant crystal direction in addition to the (1 0 0) and (1 1 1) directions, showing a transformation from the most abundant (1 0 0) direction after graphene synthesis. They found that high temperature, short reaction time (on the order of minutes) and high H_2/C_2H_2 ratio are required to grow highly crystalline few-layer graphene. Based on experimental observation, they propose that the wrinkles observed on the graphene surface were a consequence of the nucleation of defect lines on the step edges between Ni terraces and the thermal stress-induced formation around step edges and defect lines. The paper by Li et al. "Li et al. (2009)" clarify an important point regarding the mechanism of graphene growth on Ni, analyzed together with that on Cu that provides a good graphene uniformity. Starting with the consideration that the solubility of C in Cu is limited, the authors conclude that graphene formation on Ni is due to a combined deposition and precipitation mechanism: the latter requires suppression if one aims to achieve monolayer graphene growth, either by using a Ni thin film with controlled thickness and/or a high cooling rate. On the other hand, Juang et al. "Juang et al. (2010)", starting from their experiments, claim that the results of the growth method proposed for Cu systems "Li et al. (2009)", specifically the deposition mechanism, may be applicable to the Ni system in some cases. Experimental results suggest that controlling the cooling rate of the CVD process may not be a critical condition for controlling the thickness of graphene films because the deposition and precipitation mechanisms may occur simultaneously during graphene growth. They also demonstrate no direct correlation between grain boundaries and graphene flakes.

In general, graphene can be grown on metal surfaces by surface segregation and precipitation, or by surface adsorption "Li et al. (2009)". The best results for producing few-layer graphene films on Ni in which the first phenomenon occurs, have been obtained by controlling the cooling rate of the metal substrate and/or using thin Ni films from which the amount of precipitated C can be also controlled.

However, because the solubility of C in Ni is relatively high, it is difficult to suppress C precipitation completely "Zhu et al. (2010)" or carbon diffusion toward dedicated nucleation sites "Baraton et al. (2011)".

This results in forming graphene films produced varying from a monolayer to tens of layers on the same surface, instead of the quite uniform monolayer

graphene growth on Cu foils that can be obtained thanks to its low carbon solubility and slower hydrocarbon processability. Success in the preparation of controlled uniform graphene layers on Ni foils could permit to take advantage of their higher activity (e.g. shorter synthesis times), leading to economical implications and improving commercial viability.

In this chapter, a method to fabricate uniform few-layer graphene films on a polycrystalline, low cost, commercial Ni foil was reported. First, the use of a Ni foil results in less restrictions in sample area, in contrast to the thin film system. Second, flexible metal foils allow for the use of a simpler transfer process, opening possibilities to several industrial implications "Chae et al. (2009), Juang et al. (2010)". It was chosen to use ambient pressure conditions, as they are technologically more attractive, and to feed methane, to not complicate the interpretation of the results. In fact, for the understanding of the graphene formation mechanism it is a necessity to give attention to the number of gas phase transformations of the precursor molecules "Lebedeva et al. (2011)" before they reach the catalyst surface: this parameter can lead to a very different gas composition with respect to the reactor inlet gas. A reaction temperature of 950 °C has been chosen as the best compromise between economic implications and the need to decompose the "stable" methane molecules, also resulting in high quality materials. H_2 is always present in the feed flow to the CVD chambers "Kim et al. (2009), Vaari et al. (1997), Starr et al. (2006), Gall'et al. (2004), de Parga et al. (2008), Wintterlin et al. (2009), Johansson et al. (1994), Presland et al. (1969), Kehrer Jr. et al. (1954), Presland, C. Roscoe, P.L. Walker Jr., in: J.G. Gregory (Ed.), Proc. Third Industrial Carbon and Graphite Conf., Society of Chemical Industry, London, 1971, p. 116, Bernardo et al. (1976), Karu et al. (1966), Derbyshire et al. (1975), Zhu et al. (1989), Reina et al. (2009a), Reina et al. (2009b), Kumar et al. (2010), Zhang et al. (2010), Thiele et al.(2010), Pollard et al. (2009), Park et al. (2010)", but to the best of our knowledge for this system, a clarification of its role, its mechanism of action, and its optimal concentration is lacking. With the aim to understand the graphene formation mechanism and to obtain controlled carbon growth (in terms of quality, uniformity, and number of layers), on commercial Ni foils, the critical parameters that have emerged in literature such as Ni thickness, cooling rate, and polycrystalline crystallographic orientation have been explored. To perform the growth experiments, a vertical arrangement has been chosen for the reactor, since it does not suffers from the longitudinal diffusive limitations along the reactor axes that horizontal furnaces do. During the synthesis, the reactor effluent stream was continuously monitored with specific gas analyzers (Uras26) to follow the evolution of the methane decomposition and hydrogen formation.

In comparison with similar literature reports, greater attention to the effect of changing the operating conditions, such as the synthesis time and feed composition was given. The effect of hydrogen, changing its concentration

from 0 to 98.5% (v/v), was explored. For the first time, a study of the effect of the foil position in the reactor with respect to the feed flow was reported. The synthesis products were carefully characterized by the combined use of scanning electron microscopy (SEM), transmission electron microscopy (TEM), scanning probe microscopy (SPM), micro-Raman spectroscopy, micro X-ray diffraction and Xray diffraction, to explore the properties of few-layer graphene.

V.2 Experimental

V.2.1 Graphene preparation

The graphene layers were obtained by the chemical vapor deposition (CVD) "Sarno et al. (2012), Ciambelli et al. (2007), Altavilla et al. (2009)" of methane. Hydrocarbon pyrolysis was carried out in a laboratory apparatus consisting of a continuous flow microreactor fed by methane in nitrogen and/or hydrogen. Each gas stream flow rate was easured/controlled by mass flow controller (MFC). The experimental plant for the synthesis was equipped with on-line ABB analyzers that permit the monitoring of the concentrations of CH4 and hydrogen in the reactor outlet gas.

Graphene films were grown on 25 and 50 μm thick Ni foils (Nickel foil, 0.025 mm (0.001 in) thick, annealed, 99.5% (metals basis) and 0.05 mm (0.002 in) thick, annealed, 99.5% (metals basis, Alfa Aesar) at temperature of 950°C. The roughness the substrate is 200 nm, or about 20 nm if measured on a single Ni grain, when treated with N2 flow from room temperature to 950 °C + 1 min at 950 °C. Ni foils were chosen because of their availability in large size and their low cost. For each synthesis, a disk of Ni foil 1 cm in diameter was put on a sintered support onto our vertically arranged reactor (see Figure V.1).
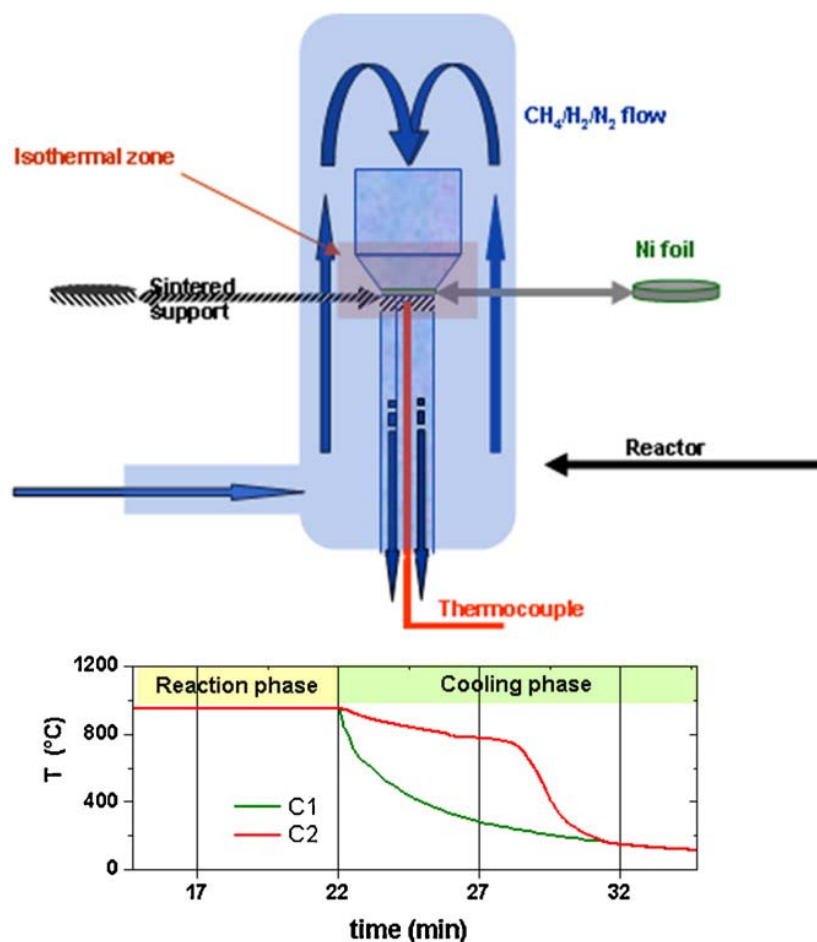
Figure V.1 *Scheme of the CVD reactor, evidencing the isothermal zone, in which Ni foil was loaded. C1 and C2 (temperature–time) cooling rate profiles.*

Sets of experiments have been performed on foils by varying the methane and hydrogen concentrations in the feed and the reaction time, and relating these parameters to the quality of the produced materials (number of layers, carbon order, homogeneity of the deposition). The most significant experiments, among more than 100 are reported in Table V.1. The syntheses have been performed in isothermal conditions, under a total flow of 100 stp/min, after pre-treatment of the foil under nitrogen flow from room temperature to the synthesis temperature for 40 min. Two different cooling conditions were explored, as demonstrated in the green (C1) and red (C2) temperatures profiles in Figure V.1 "Yu et al. (2008)".

V.2.2 Characterization methods

All the graphene samples obtained as previously described were characterized in order to define their quality (number of layers, structural order of carbon, homogeneity of deposition). Transmission electron microscopy (TEM) micrographs were obtained with a JEOL JEM 2010 electron microscope operating at 200 keV. High resolution images have been obtained with a TEM Tecnai F30 operating at 200 kV. Scanning electron microscopy (SEM) images were obtained with a LEO 1525 microscope. Raman spectra were obtained at room temperature with a micro-Raman spectrometer Renishaw inVia with a 514 nm excitation wavelength (laser power 30 mW) in the range 100–3000 cm^{-1}. Optical images were collected with a Leica DMLM optical microscope connected on-line with the Raman instrument. For all the sample about 40 measurements have been carried out on both top and bottom surface. A number of typical Raman spectra are reported in the figures (evidencing the presence from monolayer to graphite "Ferrari et al. (2006)". The laser spot diameter was 10 μm, a value higher than the size of small spots of different colors visible in the optical images. XRD measurements were performed with a Bruker D8 X-ray diffractometer using CuKα radiation and μX-ray diffractometer (Rint Rapid, Rigaku Corporation). For the characterization of the roughness of the SPM images were obtained in tapping mode, with Digital Instruments, Version 3.0.

V.3 Results and discussion

V.3.1 Analysis of the effect of Ni foil position in the reactor and Ni foil thickness

Different Ni thicknesses have been explored starting from the consideration that the mechanism of graphene formation on Ni, due to the solubility of C in the metal itself, is the result of catalytic hydrocarbon decomposition in combination with carbon diffusion in the metal and segregation and precipitation phenomena during the cooling phase.

To evaluate the effect of Ni foil thickness and Ni foil disk position on the sintered support in the reactor more than 40 measurements have been carried out on both top and bottom surface. A number of typical Raman spectra for both surfaces and Ni1 and Ni1T optical images are reported in Figure V.2 and Figure V.3. The specific collection areas are indicated in the pictures. The spectra are normalized to the intensity of the G band that are pretty much superimposable showing differences in the 2D band intensity and

profile. On the top surface of Ni1, exposed to the feed flow, few areas (shown in white) with a monolayer can be observed. In the spectrum of a graphene monolayer, the most prominent features "Malard et al. (2009)", the so-called G band appearing at 1582 cm^{-1} and the G' or 2D band at approximately 2700 cm^{-1} "Ferrari (2007)", using 514 nm excitation wavelength, are collected (see Figure V.2). The G' band at room temperature exhibits a single Lorentzian feature with a full width at half maximum (FWHM) of 24 cm^{-1} as for 1-LG "Malard et al. (2009)". The calculated intensity ratio I(2D)/I(G) is 3.7 as reported for 1 L "Ferrari et al. (2006)", decreasing with the addition of subsequent layers. A very broad D-band due to disorder or the edge "Pimenta et al. (2007)" of a graphene sample, can also be seen at about half of the frequency of the G' band (approximately 1350 cm^{-1} using laser excitation at 2.41 eV). Additionally, the so-called G* band "Malard et al. (2009)", can be seen at 2450 cm^{-1}. In Figure V.2a, two TEM images of Ni1 top surface and the electron diffraction pattern revealing the defined hexagonal patter of graphene sheet are reported. For the TEM image the carbon on the top surface of Ni1 was transferred on a TEM grid after a partial etching of the Ni film. In the spectra collected in the no white areas the 2D bands are broader, have an intensity lower than that of the G band and can be deconvoluted in more than one peak. In no case the typical Raman spectrum of graphite consisting of the two components 2D1 and 2D2, the second roughly double of the first "Ferrari et al. (2006)" are visible. However, the 2D bands collected on the bottom surface of Ni1 have the same intensity, differences in the profiles, with quite the spectrum of graphite (with the characteristic step toward higher wavelengths) on the area E and F. In particular, the Ni1 bottom surface (lying on the sintered support) does not exhibit monolayer areas. This behavior in our opinion could be due to a carbon diffusion from top to bottom during the synthesis, which results during the cooling to a greater availability of carbon in the zones adjacent the bottom surface: see also Section V.3.4.

At the same operating conditions but a larger Ni foil thickness, a higher carbon deposit was observed (e.g. when compared the top surface of Ni1 and Ni1T on which no area of graphene monolayer can be detected). Two typical spectra are reported for both surfaces (A and B containing grain edges, from the top; C and D containing grain edges, from the bottom). This indicates the occurrence of segregation and precipitation phenomena "Li et al. (2009)" that leads, in the case of Ni1T to a thicker carbon deposition under these operating conditions.

Table V.1 *List of prepared samples and relevant operating conditions*

Sample Name	Ni foil thickness mm	time min	CH$_4$ %v/v	H$_2$ %v/v	Cooling conditions
Ni1	0.025	10	25	7.5	C2
Ni1T	0.050	10	25	7.5	C2
Ni2	0.025	10	25	7.5	C1
Ni2T	0.050	10	25	7.5	C1
Ni3	0.025	1	25	2.5	C1
Ni4	0.025	0.25	25	2.5	C1
Ni5	0.025	0.33	25	2.5	C1
Ni6	0.025	0.50	25	2.5	C1
Ni7	0.025	0.42	25	2.5	C1
Ni8	0.025	10	25	0	C2
Ni9	0.025	10	25	75	C2
Ni10	0.025	1	25	75	C2
Ni11	0.025	10	5	95	C2
Ni12	0.025	9.50	5	95	C2
Ni13	0.025	9.50[a]	5	95	C2
Ni14	0.025	9.50[a]	5	95	C1

a The Ni foil was annealed before synthesis for 2 h at 950 °C under H$_2$ flow.
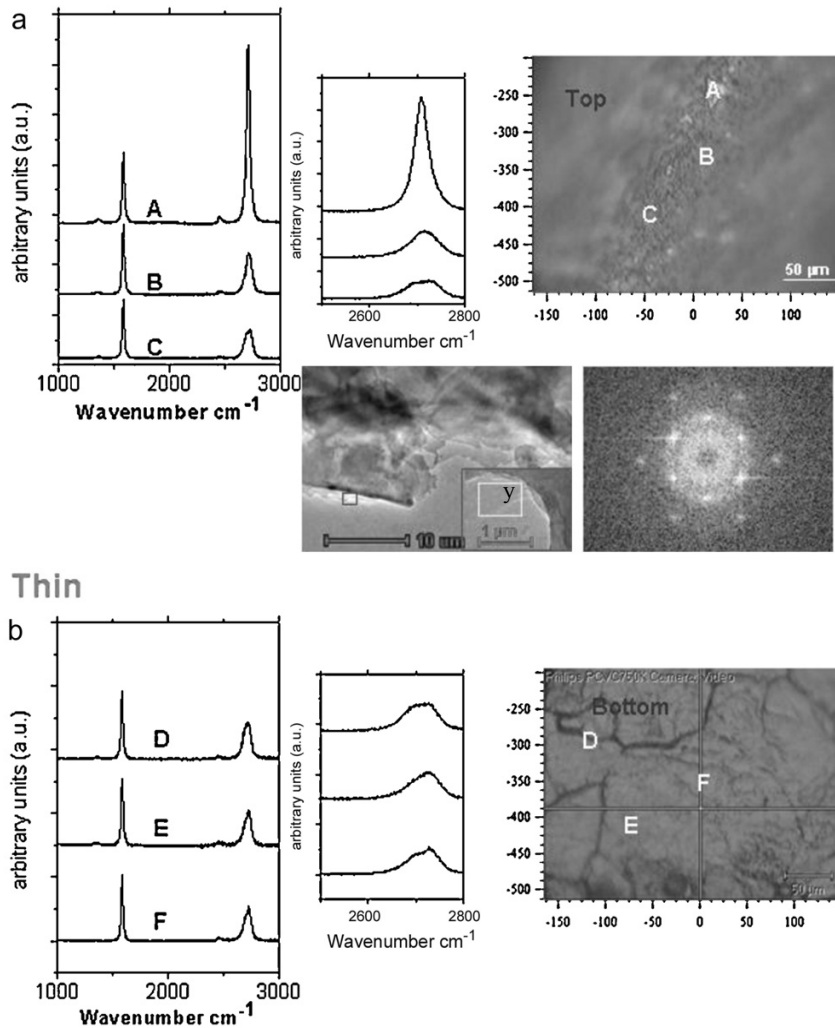
Figure V.2 *Optical image of the top surface of Ni1, related Raman spectra, TEM images at two different magnification of the carbon film form the top surface and the electron diffraction pattern collected in the y area (a). Ni1 optical images, and Raman spectra collected in the area indicated in the figure from the bottom surface (b). In particular, three Raman spectra were collected for both surfaces (a) white area A and two dark areas B and C on the top, and D containing grain edges and E and F from the bottom*
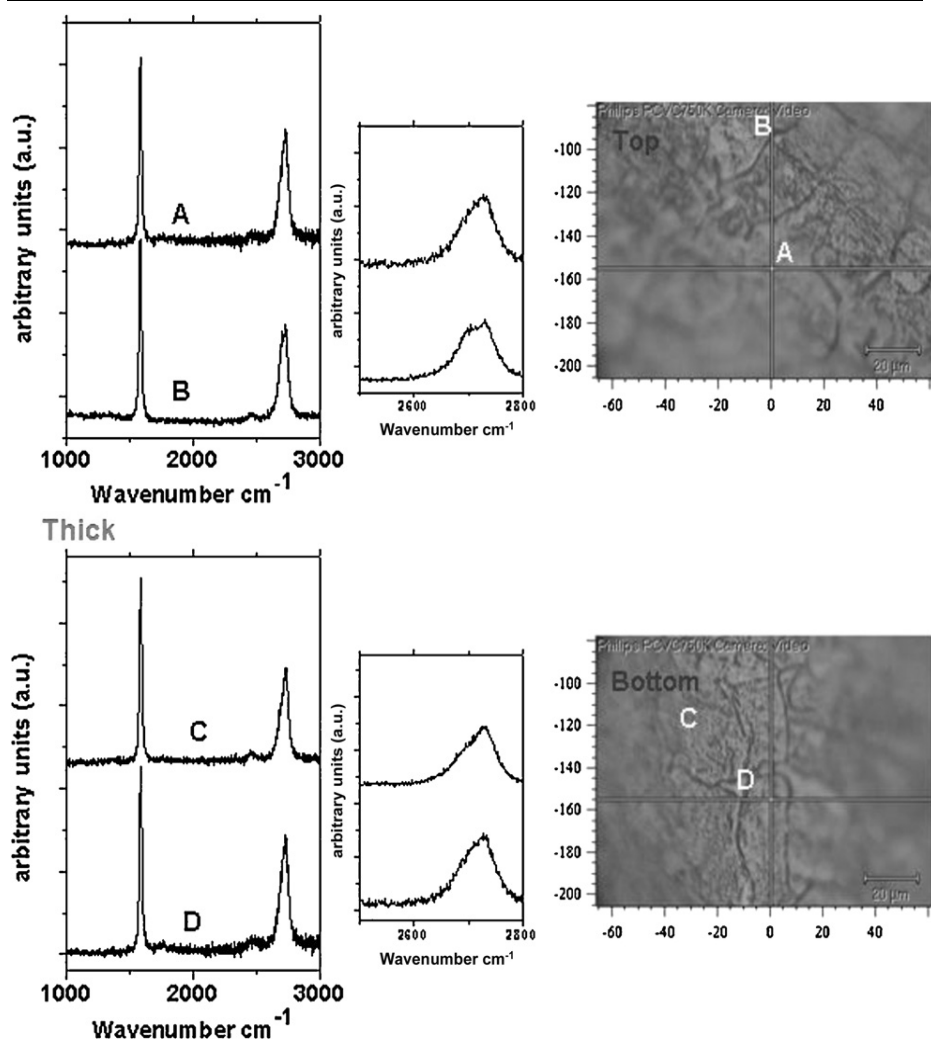
Figure V.3 *Ni1 T optical images, and Raman spectra collected in the area indicated in the figures, to evaluate the effect of Ni foil thickness and Ni foil disk position on the sintered support in the reactor. Two spectra, were collected for both surfaces (A and B containing grain edges from the top; C and D containing grain edges from the bottom)*

V.3.2 Evaluation of the effects of cooling rate

Ni2 and Ni2T have been prepared to compare the two cooling conditions C1 and C2, as shown in Figure V.1. When cooling was performed in the C2 condition (with a permanence of the sample at high temperature in the first minutes after the synthesis) a lower carbon deposition was observed on both Ni surfaces. A number of typical Raman spectra for both surfaces, and Ni2 and Ni2T optical images are reported in Figure V.4 and Figure V.5. The specific collection areas are indicated in the pictures.

White areas are visible on the both surface of Ni2 and Ni2T, but not covered by carbon in this case. In particular Ni2T exhibit an increased carbon deposition on both surfaces if compared with Ni2 (lower presence of white areas and the appearance in some cases of 2D bands with shape similar to that of the graphite) "Ferrari et al. (2006)". This indicates a phenomenon of carbon rearrangment in the metal bulk at this slower cooling rate in the high-temperature region "(Yu et al. (2008)", resulting in reduced segregation and precipitation phenomena. This result is also in agreement with that reported by Li et al. "Li et al. (2009)", showing a reduced carbon atom precipitation when passing from 3 to 0.3 °C/s.

V.3.3 Evaluation of effects of time and Ni polycrystalline orientation

The successive step was to investigate the effect of the reaction time, the C2 condition was chosen for cooling (Figure V.1). The characteristics of graphene were determined by Raman spectra associated with optical images of the surface of the samples. No graphene monolayer areas were detected after a 1 min synthesis time (Ni3): on the other hand, no carbon was detected on the Ni surface after 15 s synthesis time (Ni4). A time of 20 s (Ni5) permits the formation of few-layer graphene in some areas of the Ni surfaces, but the surfaces were not completely covered by carbon. For Ni6, few-layer graphene sheets are detected on the Ni surface but SLG or BLG.

Finally, 25 s of synthesis were tested, leading to areas covered by a graphene monolayer (Figure V.6). Nickel grains with a random size distribution (greater than 100 μm and less than 10–20 μm) can be observed.
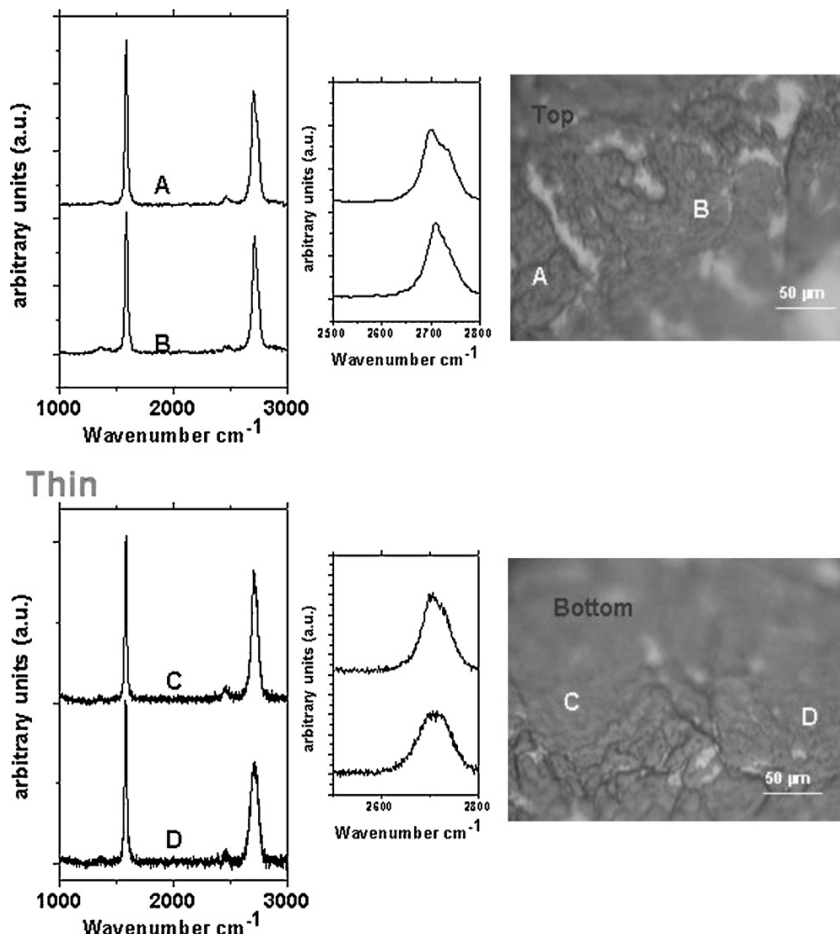
Figure V.4 *Ni2 optical images, and Raman spectra collected in the area indicated in the figures*

On these grain areas, different colors are visible (light gray, brown, dark gray and black on the grain boundary), while not directly correlated with grain boundaries "Juang et al. (2010)", these zones can be associated with different Raman spectra and are due to fewlayer graphene (FLG) "Ferrari et al. (2006)". The typical spectrum of the bulk graphite "Malard et al. (2009), Ferrari et al. (2006)" has never been found. Not only different Raman spectra are detected in the different colored areas of the Ni7 top surface, but different X-ray microdiffraction patterns as well (Figure V.6). In particular, an increased Ni(1 1 1) X-ray diffraction peak intensity is observed in the area containing type A covered by a 1 L graphene, as previously reported "Johansson et al. (1994)". For the X-ray micro-diffraction measurement, an area of 30 $\mu \times 30$ μ was scanned. The (0 0 2) reflection peak, due to graphite

interlayer spacing at 26.7°, results absent in the areas of type A, covered by a monolayer, and it is very narrow (full with at half maximum (FWHM) = 0.1°), as typical of well oriented graphite "Johansson et al. (1994), Ferrari et al. (2006)", when collected on the whole Ni7 surface.

In Figure V.7, TEM images of Ni7 are reported, as observed at the end of the acidic treatment to remove the Ni. In the carbon recovered the sheets originally grown on different nickel grains become overlapped and partially curved due to the Ni support removal. At increasing magnification, few to 12 layers are visible (Figure V.7c). Finally, in Figure V.8, SEM images of the Ni foil top surface, treated at the same operating conditions as Ni7 but in the absence of methane, and the Ni7 top surface on which areas of different colors are evident, are reported.
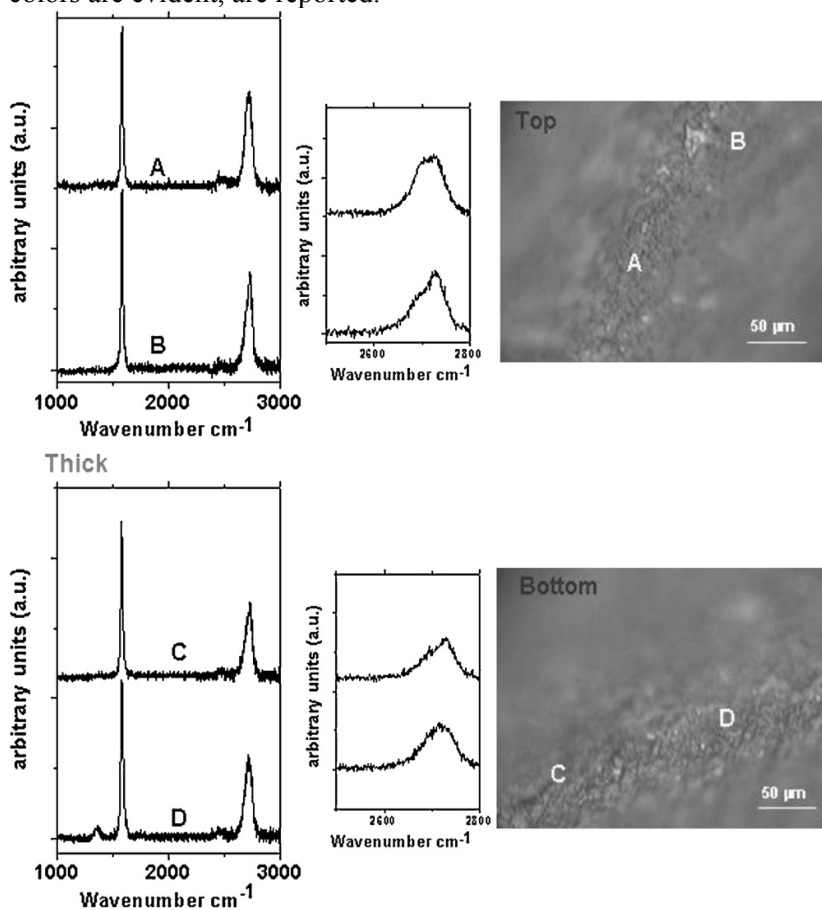
Figure V.5 *Ni2T optical images, and Raman spectra collected in the area indicated in the figures*
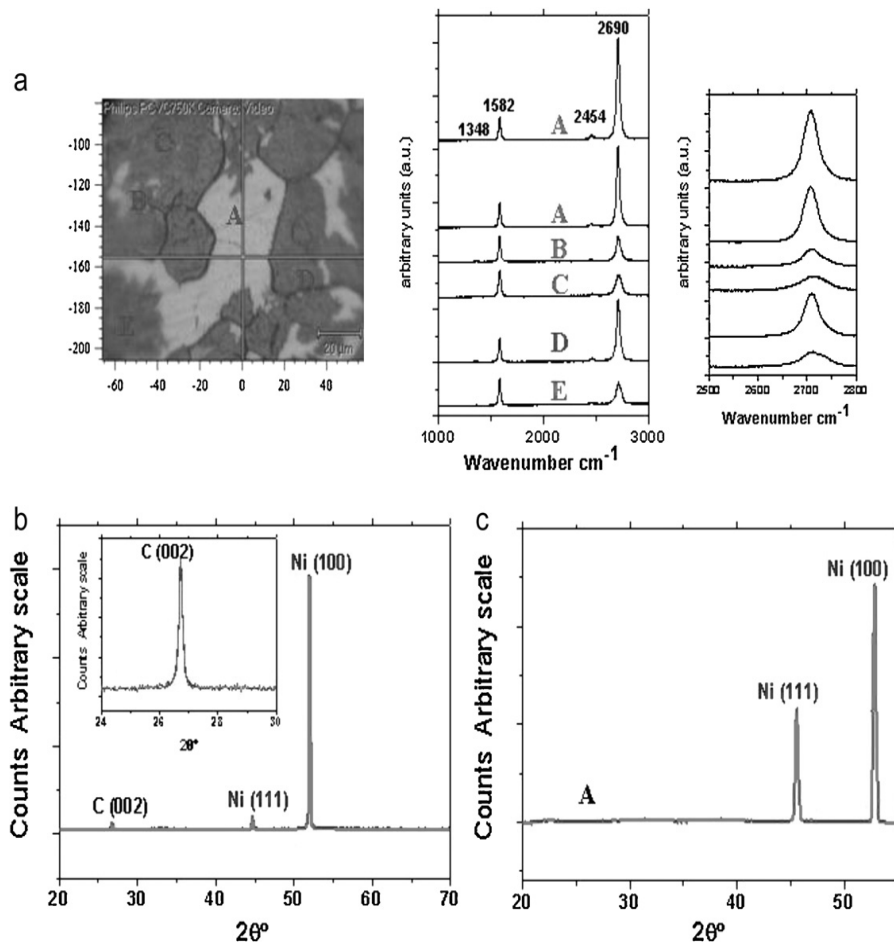
Figure V.6 *Ni7 optical images of an area from the top surface, and the typical Raman spectra collected in the area indicated in the figures (a). X-ray diffraction pattern of the whole Ni7 top surface, evidencing the presence of the (1 1 1) and (1 0 0) diffraction peaks from Ni and of the (0 0 2) reflection peak due to graphite interlayer spacing at 26.7°, that is very narrow (full width at half maximum (FWHM) = 0.1°) as typical of well oriented graphite (b). Micro X-ray diffraction pattern collected in the area A, evidencing the increased (1 1 1) X-ray diffraction peak intensity collected in a containing type A area (c).*
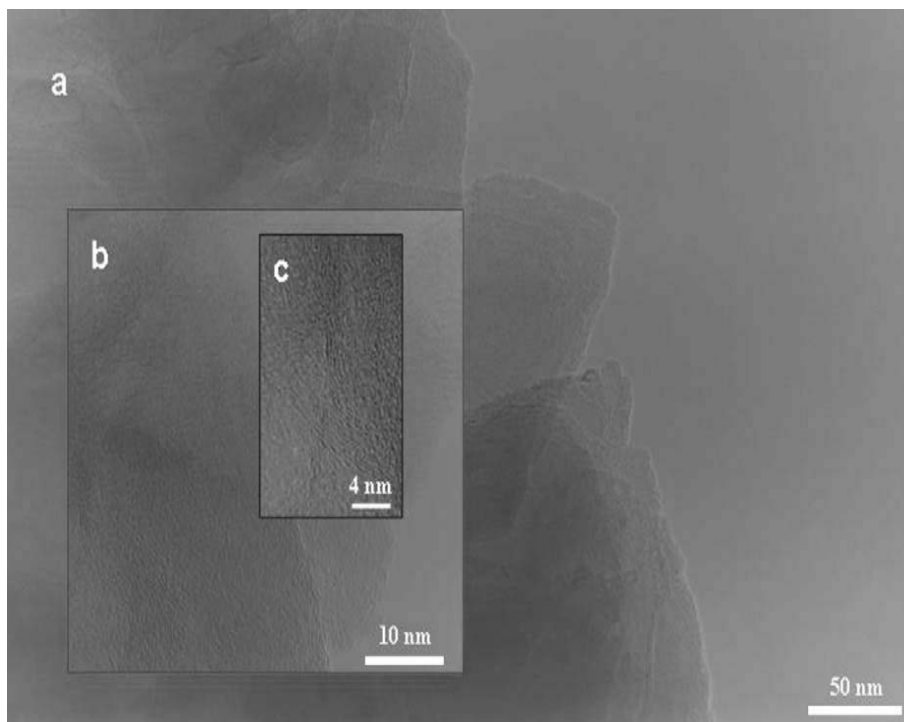
Figure V.7 *TEM images of few layer graphene, from 1 to 12, of Ni7 after Ni acidic removal, at different magnification. Images (b) in the bigger box and (c) in the smaller box are higher magnification images of areas in the image (a) and (b), respectively. The sample, at the end of the acidic treatment, consists of sheets with a size close on that of the grains, partially overlapping.*

V.3.4 Analysis of hydrogen concentration effect

Starting from the previous considerations, and aiming at achieving a controlled and uniform deposition on the Ni surface, a new set of samples from Ni8 to Ni14 have been prepared.

An optical image of Ni8, prepared in the absence of H_2 (a flux of CH_4 25% (v/v) in N_2 was fed to the reactor), shows the top surface covered with spots of different colors with a dimension on the order of 1–2 μm (lower than the laser spot size). Raman spectra collected in the areas indicated in the image are reported in the same figure. The typical (0 0 2) graphite stacking diffraction peak is also evident in the insert of Figure V.9. The surface of Ni9, obtained under the same synthesis conditions but while feeding a CH_4/H_2 flow (see Table V.1) shows remarkable carbon uniformity on the surface and an even more narrow (0 0 2) carbon diffraction peak. By increasing the H_2 concentration in the feed (Ni11), uniform few-layer graphene has been found (Figure V.10).

At the same operating conditions of N11 except for time, Ni12 exhibits a non-satisfactory uniformity of the formed carbon layers (part of the surface is not covered by carbon). Finally, Ni13 was obtained after 2 h of annealing Ni foil at 950 °C to clean and homogenize the surface "Yu et al. (2008)". It results in coverage on the bottom surface of a few-layers of uniform carbon (2–3) "Malard et al. (2009)", and exhibits a clean top surface (no carbon was detected). It is worth noting the absence of the (0 0 2) diffraction peak due to the stacking of AB graphite in the X-ray diffraction spectrum collected on the whole bottom surface of the sample. The spectrum of type A = B = C is representative of a large part of the sample surface, while fewer zones (especially those containing grain edges) were of type D. The Raman D band, due to disorder and edge, is almost indistinguishable in this case. In Figure V.11, a TEM image of a few layers of folded graphene and a higher resolution TEM image showing 3 layers are reported. This last result is clearly due to a high flow of hydrogen, but how does the H_2 act, and what is the graphene formation mechanism? Before answering these questions Ni14 was prepared. Ni14 synthesized with the same conditions as Ni13, but for the cooling rate shows a total absence of carbon on both surfaces, as expected for a sample prepared in C2 cooling conditions, giving a confirmation that carbon on the Ni13 bottom surface is formed during the cooling phase "Baraton et al. (2011)". Since the top Ni13 surface was carbon-free and uniform (2–3) layers cover the Ni13 bottom surface, we think that this is most likely due to a carbon migration from top to bottom during the synthesis, resulting in an higher carbon availability near the bottom surface during the cooling phase. These results are confirmed by the evolution of the concentration profiles of H_2 and CH_4 during the synthesis. A typical example of the concentration profiles of H_2 and CH_4 during the test for Ni13 is shown in Figure V.12 (lines). We can distinguish three temporal phases:

Pre-reaction phase (I): H_2 is fed to the analyzer, the concentration values of hydrogen is 98% (v/v).

Reaction phase (II): H_2 is fed to the reactor, reaching the analyzer after passing over Ni. After the time necessary to cross the reactor, and accounting for the delay time of the analyzers, the steady state hydrogen concentration reaches a maximum at 98.2 vol.%.

Post-reaction phase (III): the reaction has ended, and the gas is sent directly back to the analyzer (bypassing the reactor). The concentration is the same as that in the pre-reaction phase.
A blank test (line with cross in Figure V. 12) was performed by recording the evolution of the hydrogen and methane composition to determine the

behavior of the system in the absence of Ni. The concentration of hydrogen and methane in the absence of Ni stay constant as during phase I.

Starting from the hydrogen produced during the test that comes from the catalytic decomposition of methane the moles of C deposited have been quantified (moles deposited carbon = 1.4×10^{-6}).
This value is lower than the saturation threshold limit (2.2×10^{-3} gC/gNi = 1.07 at.% 950 °C), indicating that the carbon on the Ni bottom surface is formed during the cooling phase "Baraton et al. (2011)".
Considering the very high level of hydrogen and the with a very low conversion of methane during the synthesis time, the best solution for the reagent system working in these operating conditions must provide for a readjustment and a recycling.
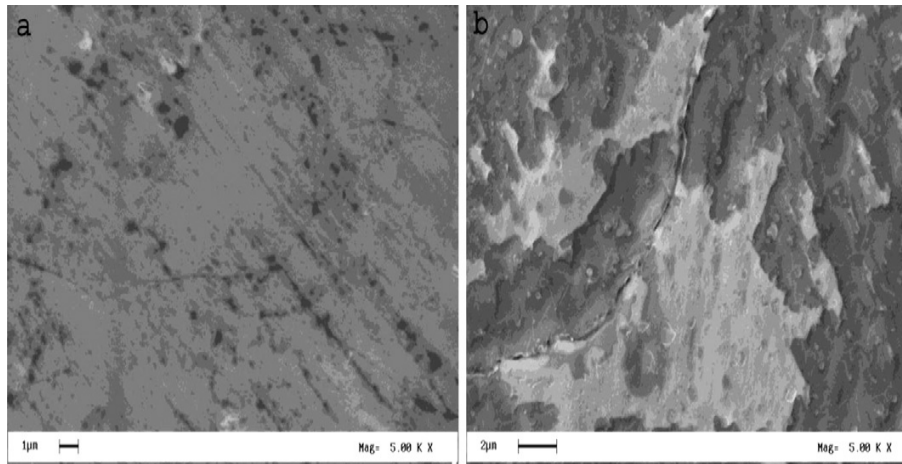
Figure V.8 *SEM images of: Ni foil surface treated in the same conditions of Ni7 but in the absence of methane (a); Ni7 surface evidencing the presence of different color areas*

V.3.4.1 Formation mechanism of few-layer graphene on Ni, in the presence of a high H_2 concentration

Graphene formation on Ni happens: (i) during the cooling phase, due to the high solubility of carbon in nickel, by a segregation and precipitation mechanism, and (ii) by deposition during the synthesis phase "Kumar et al. (2010)", when the solid solution has been saturated. In a 1979 study "Eizenberg and Blakely (1979)", Eizenberg and co-author performed extensive studies on the formation of carbon films by cooling Ni foils

saturated with C at high temperatures. They found that a monolayer of graphite formed under a temperature decrease due to C segregation; this was followed by graphite precipitation. They report that the partition of carbon atoms in Ni between the surface and bulk would also be observed if the carbon chemical potential were controlled by adjusting the composition of the CH_4–H_2 mixture in contact with the surface instead of controlling the carbon doping level in the bulk crystal.

In Figure V.13, a scheme describing the steps involved in graphene formation on Ni foil under steady state conditions is shown. In the high-temperature phase "synthesis phase" the steps are: (i) the gas phase diffusion of the precursor molecules; (ii) hydrocarbon adsorption/desorption and decomposition on the metal surface and carbon diffusion into the catalyst, followed, after a metal saturation, by incorporation in the growing structure.
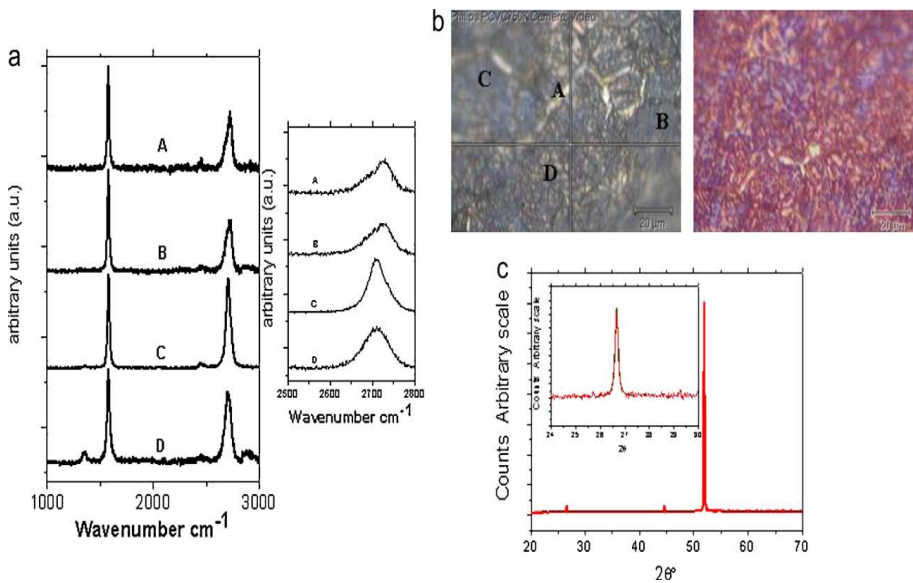
Figure V.9 *Ni8 typical Raman spectra (a), collected in the area indicated in the optical image of the top surface (b on the left), and the optical image of the transferred carbon film on SiO₂/Si (b on the right). X-ray diffraction pattern of the whole Ni8 top surface, evidencing the presence of the (1 1 1) and (1 0 0) diffraction peaks from Ni and of the (0 0 2) reflection peak due to graphite interlayer spacing (c)*

V.3.5 What happens at high hydrogen concentrations?

During CVD graphene synthesis under ambient pressure, at a typical synthesis temperature that exceeded 950 °C, the rate limiting step is usually the diffusion through the boundary layer "Lebedeva et al. (2011), Bhaviripudi et al. (2010)".
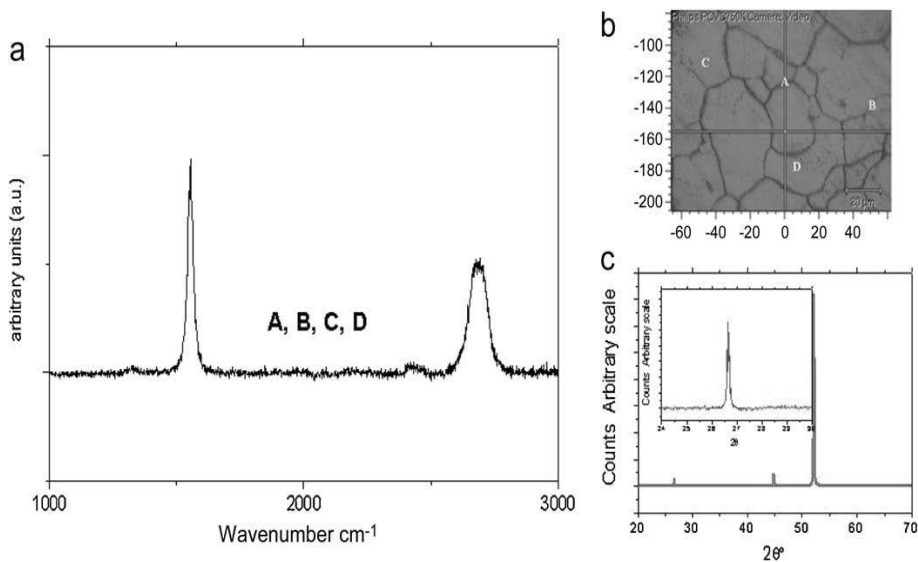
Figure V.10 *Ni11 typical Raman Spectrum of the surface (a) and optical image (b). X-ray diffraction pattern of the whole Ni11 surface, evidencing the presence of the (1 1 1) and (1 0 0) diffraction peaks from Ni and of the (0 0 2) reflection peak due to graphite interlayer spacing (c)*

In these conditions, the mass transfer, which depends on the diffusion coefficient, which is itself inversely proportional to the pressure, becomes disadvantaged, while the reaction kinetics, depending exponentially on the temperature, is favored. This results in the fact that reactor geometry affects the result of the synthesis.

To partially solve this problem, we have chosen to work with a vertically arranged reactor to avoid the boundary layer variation along the surface of the foil, as would be typical in an horizontal CVD chamber. However, in the diffusive limitation step, the boundary layer thickness, and thus the hydrocarbon supply rate, can change locally also as a result of defects or dust. It is clear that working in the reaction regime, where the processes are primarily dependent on the temperature of the substrate, is possible to avoid the deleterious boundary layer and the geometric effects on graphene synthesis. This can be obtained, for example, by working at a low pressure "Kumar et al. (2010)". However, as previously reported "Lebedeva et al.

(2011)" for the same catalyst in similar experimental conditions (for the synthesis of carbon nanotubes, with Ni in form of powder), dilution of the hydrogen containing feed flow usually shifts the regime to a diffusion-controlled regime.
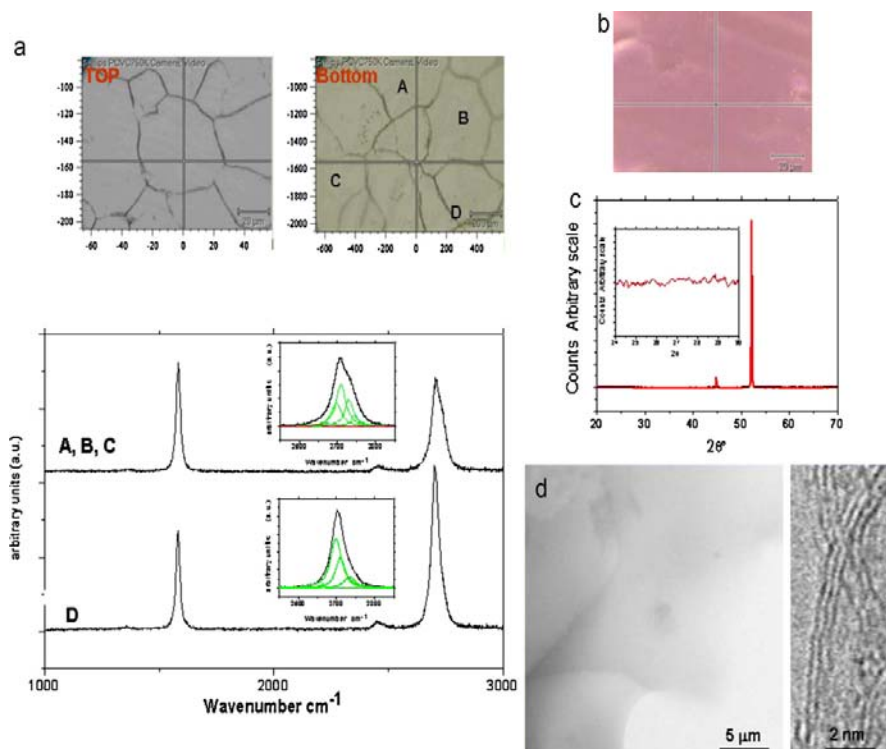
Figure V.11 *Ni13 optical images and Raman spectra from the bottom surface (a). Optical image of the transferred few layers graphene on SiO$_2$/Si (b). X-ray diffraction pattern of the whole Ni13 bottom surface, evidencing the presence of the (1 1 1) and (1 0 0) diffraction peaks from Ni and the absence of the (0 0 2) reflection peak due to graphite interlayer spacing (c). TEM image of a few layers of folded graphene and a higher resolution TEM image showing 3 layers are reported (d)*

On the other hand, in addition to the influence on the diffusion of the precursor, hydrogen affects the kinetics of hydrocarbons and leads to an increase of the rate of desorption of hydrocarbons from the catalyst surface. At high partial pressures of hydrogen the rate of hydrocarbons desorption exceeds the rate of carbon formation.
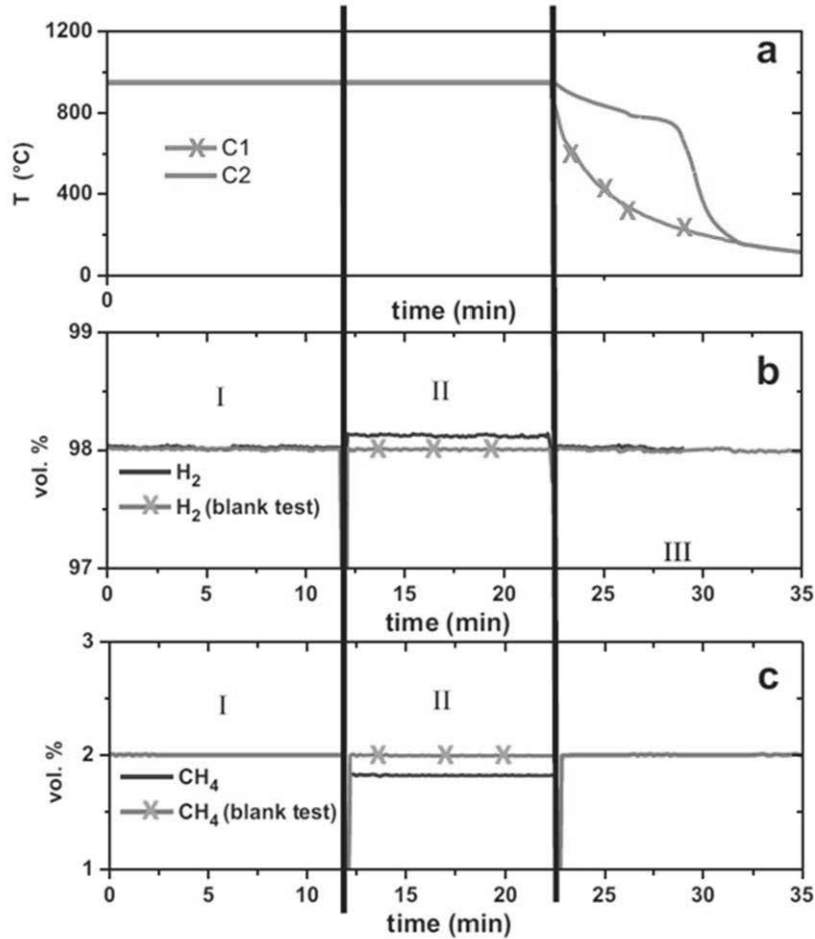
Figure V.12 *Temperature profiles during the pretreatment, the syntheses and under cooling (medium cooling green, slow cooling red) (a). Concentration profiles of H_2 during Ni13 test (line) and a blank measurement (line with cross) (b). Concentration profiles of CH_4 during Ni13 test (line) and a blank measurement (line with cross) (c)*

In this desorption-controlled regime the carbon supply rate is determined by the surface concentration of carbon atoms, which is established by the balance of adsorption and desorption processes. This results in an arrangement of carbon atoms during the cooling within the Ni film, leading to the formation of an ordered carbon layer. The carbon formation on the nickel surface is controlled despite the thickness and roughness of the film,

the crystallographic orientation of the different zones, the high solubility of carbon in nickel, and the cooling rate.
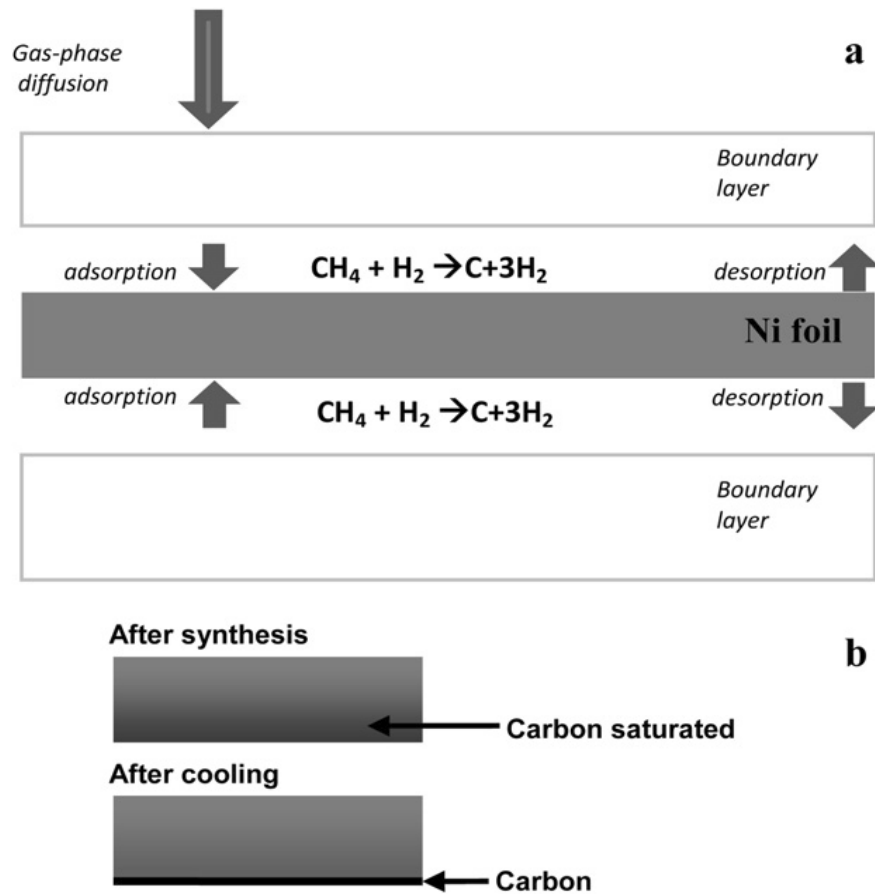
Figure V.13 *Reaction synthesis scheme (a). Nickel saturated by carbon after synthesis, and the carbon layer covering the bottom Ni surface at the end of cooling (b)*

V.4 Conclusions

The reactor geometry and the position of the catalyst in the reactor are very important parameters by which to control graphene formation. In any case, the bottom Ni surface (lying on the sintered support) shows an increased carbon deposition with respect to the top surface. This behaviour could be due to carbon diffusion from top to bottom during the synthesis, which results in a greater availability of carbon in the zones adjacent the bottom surface during cooling. An increase of the segregation and precipitation phenomena under Ni thickness increase was observed. In the same operating conditions but cooling rate a lower carbon deposition was observed on both Ni surfaces when the sample remains at high temperature in the first minutes after the synthesis. This indicates a phenomenon of carbon rearrangment in the metal bulk, at this slower cooling rate in the high-temperature region, resulting in reduced the segregation and precipitation phenomena. By decreasing the synthesis time, it is possible to obtain few-layer graphene on the nickel surface, which also contains 1 L on areas showing an increased Ni(1 1 1) diffraction peak intensity, but without homogeneity. By increasing the hydrogen concentration it is possible to control the final graphene formation on the nickel surface, despite the thickness and roughness of the film, the crystallographic orientation of the different zones, the high solubility of carbon in nickel, and the cooling rate. In particular quite uniform 2–3-layer graphene has been obtained on the bottom Ni surface during cooling, leaving no excess carbon.

Chapter VI
Experimental III
Graphene transfer

VI.1 Introduction

Different synthesis methods have been developed to isolate single to few layer graphene, such as epitaxial growth on SiC, oxidative/thermal intercalation and ultrasonication of graphite and recently by CVD on metal foils (Ni, Cu). In particular, graphene on Cu foil has collected considerable interest due to its ability to produce macroscopic areas of mostly monolayer graphene. In order for growth on Cu to be a viable route to large-scale graphene applications, there must be a reliable method for transferring the graphene from metallic Cu substrates to more useful substrates "Regan et al. (2010)".

VI.2 Graphene transfer process

The placement of graphene on arbitrary substrates is key for applications and characterization.

The ideal approach would be to directly grow graphene where required. However we are still far from this goal, especially in the case of non-metallic substrates. Alternatively, a transfer procedure is necessary.

The graphene samples were grown on nickel and copper foil with a CVD process. The quality and number of layers of the as-grown graphene were evaluated by Raman spectroscopy.

Once synthesized, CVD graphene was transferred on a suitable substrate, making the technique versatile for many applications.

First of all, any carbon layers were gently removed from on one side of the copper foil with nitric acid (65%). Subsequently, a polymer support, such thermal release tape (Nitto Denko Co.), was glued on the graphene layer by applying soft pressure (about 0.2 MPa).

When transferring graphene using a thermal release tape, first peel off the protective layer from the thermal release tape, then put the adhesive layer of the tape on top of the layer of graphene.

An aqueous solution of ferric chloride (0,1 g/ml) for approximately 12 hours was used as etchant to remove the metal foil. This solution works well for nickel as well as for copper.

The tape with graphene should be pressed firmly to the substrate, avoiding to damage the substrate.

In this way, graphene is attached only to the polymer, which can be positioned onto any other substrate. After etching, graphene transferred on thermal release tape was rinsed with deionized (DI) water to wash off remaining Ni/Cu etchant.

After the metal was completely removed and then after cleaned, graphene film was transferred on substrate like glass, silicon wafer, polymer, through forced convection heat applying uniform pressure at 80°C, so that the tape lose its adhesion and the graphene film detach from the tape and transfer to the substrate.
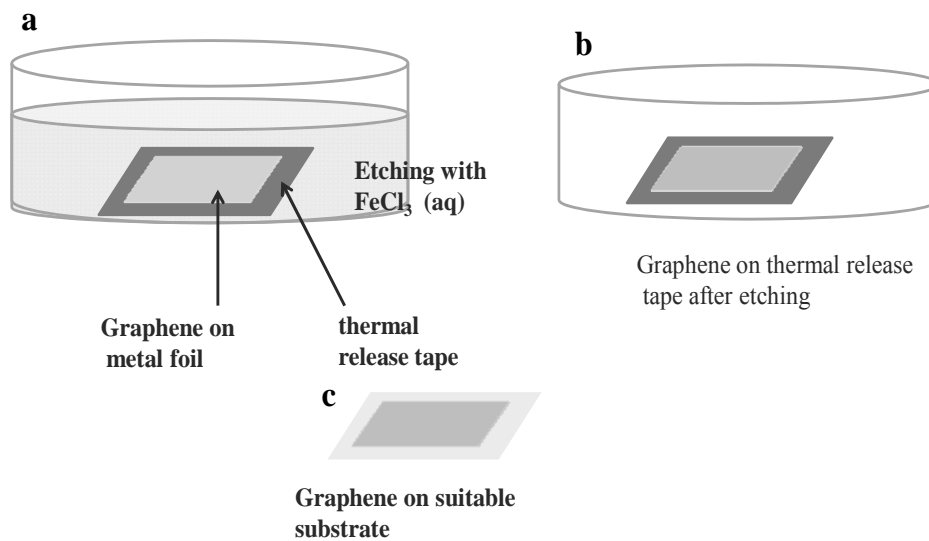
Figure VI.1 *A scheme of the transfer process: metal foil/graphene/thermal release tape in FeCl₃ solution (a) After the removal on the metal foil, graphene is attached to a thermal release tape and it can be transferred on a suitable substrate.*

a
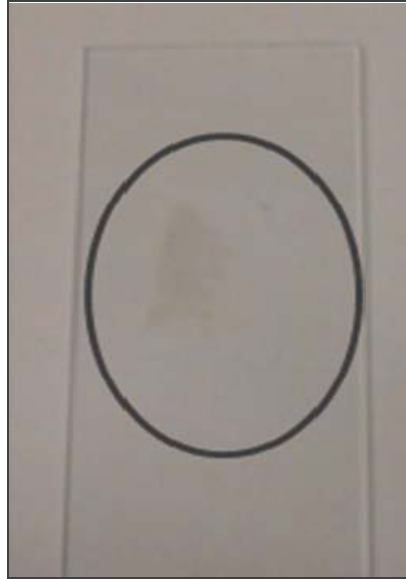
b
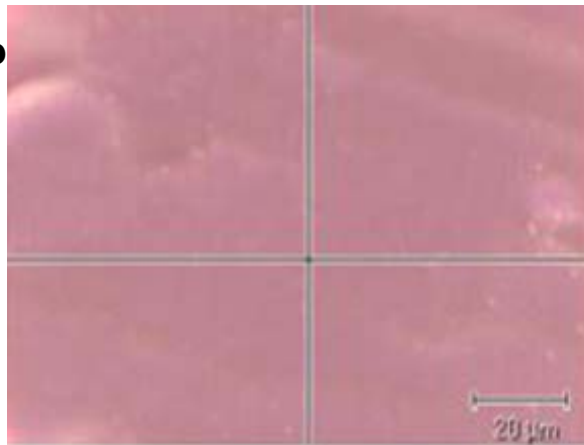
Figure VI.2 *Photograph of graphene transferred on a glass slip (a) optical image of the transferred few layer graphene on SiO$_2$/Si (b)*

In Figure VI.2a, a photograph of a by-layer graphene transferred on a glass slip (2.5 x 7.5 cm) and an optical image of the transferred carbon film on SiO_2/Si in Figure VI.2b is shown.

VI.3 Conclusions

In conclusion, a very simple graphene transfer method using a thermal release tape is shown. In this way, graphene can be transferred on different substrate like glass, polymer, silicon wafer.

Chapter VII
Experimental IV

Effect of the operating conditions on the catalytic synthesis of graphene-coated nanoparticles

VII.1 Introduction

The attention to the process parameters of the stable magnetic nanoparticles (MNPs) synthesis to obtain a controlled product, is of particular importance in view of the exploitation of their properties "Niemeyer (2001), Altavilla et al. (2009), Lu et al. (2007)" in the different fields in which they can be used, including catalytic, environmental, biological, biomedical and electronic.

Many attention has been focused on the synthesis of MNPs "Niemeyer (2001), Altavilla et al. (2009), Lu et al. (2007)" and different strategies have been developed to preserve MNPs stability against agglomeration or precipitation and oxidation phenomena, involving polymers "Gaster et al. (2009), Kim et al. (2001), Nikolic et al. (2006)", silica "Yi et al. (2005), Santra et al. (2009), precious metals "Rivas et al. (1994), Shon et al. (2002)" and carbon-coated NPs (CMNPs) "Scott et al. (1995), Ang et al. (2004), Teunissen et al. (2001), Hayashi et al. (1996), Nesper et al. (2006), Nikitenko et al. (2001), Geng et al. (2004), Bystrzejewski and Rümmeli (2007), Seo et al. (2006)".The carbon covering have many advantages over the other coatings, such as much higher chemical and thermal stability, having also the possibility to be easily functionalized. It has been reported

"Lu et al. (2007), Seo et al. (2006), Bai et al.(2005)" that CMNPs are biocompatible materials, on the other hand the mechanism of such hybrid magnetic nanostructures cytotoxicity is still not fully explored. More recently it has been concluded "Grudzinski et al. (2013a), Grudzinski et al. (2013b), that a great caution should be devoted to physicochemical features of the CMNPs and further preclinical studies are needed before their use. Different carbon coating strategies have been developed. Carbon-encapsulated metal or metal carbide nanocrystallites have been generated by the Kratschmer arc-discharge process already in 1995 "Scott et al. (1995)". Since then, many studies have shown that in the presence of metal nanoparticles (Co, Fe, Ni, Cr, Au, etc), graphitized carbon structures, such as carbon nanotubes and carbon onions, are formed under arc-discharge, laser ablation, and electron irradiation "Ang et al. (2004), Teunissen et al. (2001), Hayashi et al. (1996), Nesper et al. (2006)". Gedanken and co-workers reported a sonochemical procedure that leads to air-stable cobalt nanoparticles "Nikitenko et al. (2001)". Johnson et al. describe a simple method to prepare carbon-coated magnetic Fe and Fe3C nanoparticles by direct pyrolysis of iron stearate at 900°C under an argon atmosphere "Geng et al. (2004)". Moreover, carbon-coated nanoparticles are usually in the metallic state, and thus have a higher magnetic moment than the corresponding oxides "Niemeyer (2001)". Chemical Vapour Deposition (CVD) technique offers the advantage of being the easiest to scale up towards an economically viable production "Seo et al. (2006), Bai et al. (2005), Grudzinski et al. (2013a), Grudzinski et al. (2013), He et al. (2006), Dumitrache et al. (2004)". In particular, He et al. "He et al. (2006)" demonstrated for the first time the feasibility of synthesizing carbon-encapsulated nanoparticles free of byproducts, such as carbon nanotubes/nanofibers, carbon nanoparticles and amorphous carbon, and agglomeration, which would limit the potential applications of the NPs. He et al. "He et al. (2006)" prepared NPs with a mean diameter of 15 nm, with a standard deviation of 3 nm, via CVD over a Ni/Al catalyst. Seo et al. "Seo et al. (2006)" obtained stable magnetic nanoparticles by impregnating high-surface-area silica powder in methanol with iron and cobalt species. Carbon coating of the metal-loaded silica was obtained by flowing a 100% methane stream in a CVD chamber. They found, for their body-centered-cubic-NPs of 7 nm diameter the highest saturation magnetization obtained for nanocrystal, and despite the smaller size a lower value for the 4 nm NPs, likely due to the presence of a mixed body-centered-cubic-FeCo and face-centered-cubic-Co phases. The nanoparticles were tested as advanced magnetic resonance and near–infrared imaging agents and, more recently, for few-cells enrichment and detection "Chen et al. (2012)".

However, little or no attention has been focused on the synthetic process in which the products, having identified the catalyst and carbon source, strongly depend by operating conditions chosen. The selective coating of nanoparticles, is still, an aspect to analyze and optimize. In fact, the presence of carbon in the samples, other than the nanoparticles coating, (e.g., coming from an homogeneous decomposition) would decrease the magnetic performances and constitutes an impurity in view of the successive applications. For example, feeding a pure hydrocarbon flow makes it very difficult to obtain a satisfactory reaction yield and/or controlled nanoparticle coverage and carbon selectivity. Little attention has been devoted to investigating the influence of the support on the characteristics of the prepared materials. In addition, insight into the formation mechanism is key to controlling the synthesis process.

However, identification of the parameters that determine the size of the nanoparticles and their distribution for Co/Fe on Al_2O_3 has not been explored.

Herein, in this chapter the preparation of stable core-shell graphene-coated magnetic nanoparticles (GCMNPs) via catalytic chemical vapor deposition (CCVD) of methane at atmospheric pressure was reported. Alumina, which is a very good support catalyst due to its narrow and small size porosity and the coupling effect with the metal active phase, was used as the support for the Co and Fe "Sarno et al. (2012)". The prepared nanoparticles (~4.1 nm in diameter) possess a very narrow size distribution and are by-product free.

Particular attention has been devoted to studying the effects of the reactor operating conditions on the reaction yield and quality of the produced materials. Therefore, feed gas composition, total flow rate, catalyst mass, metal catalyst weight, and catalyst pretreatment were varied in the CCVD runs. In addition, the inlet and outlet reactor concentrations of the reactants and products, respectively, were monitored continuously with specific gas analyzers to obtain a quantitative description of the synthesis process.

To perform the growth experiments, a vertical arrangement has been chosen for the reactor because it does not suffer from the longitudinal diffusive limitations along the reactor axes in typical CVD horizontal furnaces "Sarno et al. (2012), Sarno et al. (2013)". During CVD synthesis at atmospheric pressure and a typical temperature (700-900°C), the rate-limiting step is typically the diffusion through the boundary layer. Under these conditions, the mass transfer rate, which depends on the diffusion coefficient that is inversely proportional to the pressure, is disfavored, and the reaction kinetics, which depend exponentially on the temperature, are favored. Therefore, the reactor geometry can affect the results of the synthesis. To partially solve this problem, we have chosen to work with a vertically

arranged reactor to avoid the boundary layer variation along the surface of the catalyst bed, as would be typical in a horizontal CVD chamber.

To characterize the catalyst and the reaction products and to correlate their properties with the operating conditions, various techniques were employed as follows: transmission electron microscopy (TEM), scanning electron microscopy (SEM), Raman spectroscopy, thermogravimetric analysis (TG-DTG) coupled with a quadrupole mass detector, X-ray diffraction analysis, inductively coupled plasma mass spectrometry (ICP-MS), dynamic light scattering (DLS), and N_2 adsorption–desorption at 77 K.

VII.2 Materials and methods

The Co, Fe catalyst (50 wt.% of each metal) was prepared by wet impregnation of gibbsite (γ-Al(OH)$_3$) powder "Sarno et al. (2012), Giubileo et al. (2012)" with cobalt acetate and iron acetate solutions followed by drying at 80°C for 3 h.

CCVD was performed in a continuous flow microreactor fed by a methane–hydrogen gas mixture. The microreactor was a quartz tube (16 mm internal diameter, 300 mm in length), and the catalyst (particle sizes in the range 38-53 μm, sieved prior to synthesis) was loaded onto a sintered support "Sarno et al. (2012), Giubileo et al. (2012)". An external coaxial quartz tube (35 mm internal diameter) allowed the reactant stream to be preheated. The temperature of catalyst bed was measured with a K thermocouple located inside a third internal coaxial quartz tube (4 mm internal diameter). The reactor was heated by an electrical oven whose temperature was controlled by a temperature programmer–controller (Eurotherm 2408). Cylinder gases (99.998 pure methane and 99.9990 pure hydrogen) were mixed to obtain the methane/hydrogen stream that was fed into the reactor. A constant flow rate of each gas was provided by mass flow controllers. The experimental plant for the synthesis was equipped with on-line analyzers (Uras 26, ABB) that permit the alternating monitoring of the inlet and outlet reactor concentrations of the reactants (methane (CH_4) and hydrogen (H_2)) and products (acetylene (C_2H_2), ethylene (C_2H_4), and hydrogen (H_2)) continuously during the reaction via a bypass valve.

The typical procedure for preparing GCMNP particles includes (1a) feeding the reacting gas to the analyzers to verify the steady state inlet concentration. (1b) N_2 is fed to the reactor by another feed line to pre-treat the catalyst. (2) The pre-treatment nitrogen flow was stopped using the bypass valve, and the reacting gas stream was started to feed the reactor. (3a) After 5 min, the

reacting gas stream was stopped, and nitrogen was fed to the reactor. Next, (3b) the reacting gas is fed to the analyzers. (4) The reactor was extracted from the furnace and allowed to cool under ambient temperature conditions. (5) chemical attack with a diluted HF solution (15 vol. %) for 3 h, followed by centrifugation and washing, in distilled water, under filtration.

The catalyst was preheated prior to starting the CCVD process at 70°C/min up to the synthesis temperature, and the run time was 5 min. The total feed flow, catalyst mass and gas composition were varied, as reported in Table VII.1.

Table VII.1 *Prepared samples*

Samples	Total flow rate (cc/min)	% CH_4	Catalyst Weight (mg)
GCMNP1	400	10	125
GCMNP2	100	100	125
GCMNP3	50	100	125
GCMNP4	100	100	250
GCMNP5	400	10	1350

To better understand the experimental results, five samples were prepared, as shown in Table VII.2.

TG-DTG analysis in flowing air with a 10 K/min heating rate was performed with an online SDTQ 600 Analyzer (TA Instruments) connected to a quadrupole mass detector (Quadstar 422, Pfeiffer Vacuum).

SEM images were captured with a LEO 1525 microscope. TEM images were acquired using a FEI Tecnai electron microscope operating at 200 kV with a LaB6 filament as the source of electrons. The samples for the TEM observation were prepared via sonication in ethanol for 2-5 minutes followed deposition of the sample on a carbon grid.

Raman spectra were obtained at room temperature with a microRaman spectrometer (Renishaw inVia; 514 nm excitation wavelength).

The ICP-MS analysis was performed using an Agilent 7500ce ICP-MS instrument.

XRD measurements were performed in the 2ϑ range of 20-30° with a Bruker D8 X-ray diffractometer using $CuK\alpha$ radiation.

The particle size distribution was determined using a dynamic light scattering (DLS) instrument (HPPS ET_ Malvern Instruments).

The surface area and porosity characterization were obtained via N2 adsorption–desorption at 77 K with a Kelvin 1042 V3.12, COSTECH Instruments. The powder samples were outgassed in a He flow at 250°C for 3 h prior to the measurement.

VII.3 Results

VII.3.1 Catalyst metal loading

The Co and Fe contents in the catalyst obtained by ICP-MS (model Agilent 7500ce ICP-MS instrument) were similar (49.7 and 49.8 wt% for Co and Fe, respectively) to the values expected from the catalyst preparation.

An air flow TG-DTG (SDTQ 600 Analyzer) analysis of the gibbsite supports "Sarno et al. (2012)" and the catalyst has been performed for comparison. The total mass loss observed on the TG curve for gibbsite (see Figure VII.1a) from 220 to 820°C was 34.2%, which is in agreement with the theoretical value of 34.6% for the following reaction:

$$Al(OH)_3 \rightarrow \frac{1}{2}Al_2O_3 + \frac{3}{2}H_2O$$
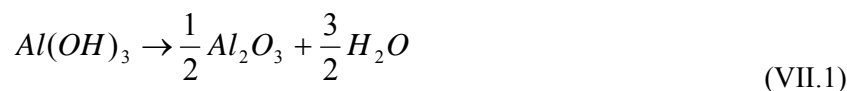
(VII.1)

The TG-DTG-DSC-MS analysis of the catalyst is shown in Figure VII.1b. The original catalyst mass (125 mg) is the sum of the gibbsite weight (41.7 mg) plus the organic metal precursors (56.05 mg organic component, 27.25 mg metal component).

During the thermogravimetric test performed on the catalyst, the weight loss at 75- 300°C was due to the simultaneous decomposition and oxidation of the organic portion of the metal precursor (which was confirmed by the corresponding total ion current (TIC), with mass fragments at m/z = 30, 46, 58, 59 and 44 due to CO_2 release) followed by the endothermic transformation of gibbsite into boehmite.

Table VII 2 *Additional samples*

Samples	Starting material	Treatment	Flow (cc/min)	% CH$_4$ in the isotherm step	Weight (mg)
Al1	non impregnated gibbsite	25-800°C 70 K/min under N$_2$ + 5 min at 800°C	400	10	41.7
Al2	non impregnated gibbsite	25-800°C 70 K/min under N$_2$ + 5 min at 800°C	100	100	41.7
Al3	non impregnated gibbsite	25-800°C 70 K/min under N$_2$ + 5 min at 800°C	100	0	41.7
Al4	non impregnated gibbsite	calcination at 400°C for 2h + 25°C-800°C 70K/min under N$_2$ + 5 min at 800°C	100	0	41.7
Al5	impregnated gibbsite	25-800°C 70 K/min under N$_2$ + 5 min at 800°C	100	0	41.7

At temperatures higher than 300°C, further dehydration of boehmite and the formation of a second type of anhydrous aluminum oxide were observed. The first step in the weight loss below 75°C can be attributed to residual methanol (see mass fragments 30 and 31). Alumina and metal oxides constitute the thermogravimetric residue, which is equal to 44.2 wt.% (19.4 wt. % alumina, 24.8 wt.% metal oxides). Subtracting the total weight loss in the 75-625°C range from the contribution due to the gibbsite transformation, the weight loss due to the organic portion of the metal precursors is

consistent with a metal loading in the final catalyst of 50 wt.% iron and 50 wt.% cobalt (27.3 mg).

VII.3.2 GCMNP1 characterization and analysis

Figure VII.2 shows a typical TEM image of purified GCMNP1. The nanoparticles have an average diameter of 4.12 nm with a 0.86 nm standard deviation, as measured for ~400 nanocrystals) and are covered by 1-2 layers of graphene (see the HRTEM insert in the Figure VII.2). A selected-area electron-diffraction pattern is also shown in the Figure VII.2.
The SEM characterization indicated that GCMNP1 is composed of GCMNP aggregates, which are less than 1 μm in size, on the alumina surface (Figure VII.3a). At increasing magnifications (Figures VII.3b, VII.4a-b), the aggregated nanoparticles of the purified GCMNP1 after alumina removal were observed.
In Figure VII.5a, the X-ray diffraction pattern of GCMNP1 is shown. The peaks at 44.87, 65.32 and 82.75 2θ are typical of a crystalline body-centered-cubic Co/Fe alloy. It is important to note the absence of the (002) diffraction peak due to the stacking of AB graphite.

By applying the Scherrer equation to the 110 diffraction peak:

$$L_a = 0.9\lambda / B \cdot \cos\Theta \qquad\qquad (VII.2)$$

where La is the metal core diameter, λ is the X-ray wavelength, B is the peak half-maximum width and Θ is the Bragg angle, the La value was determined to be 4.22 nm, which is very similar to that measured in the HRTEM images.

In Figure VII.5b, the Raman spectrum of GCMNP1 is shown. In particular, the most prominent features "Sarno et al. (2013)" of the sp^2 carbon materials, which are known as the G band and the G' or 2D band, were observed at 1582 cm^{-1} and approximately 2700 cm^{-1}, respectively, using 514 nm excitation wavelength. A broad 2D band (FWHM= 75 cm^{-1}) and a pronounced D band, which are characteristic for curved graphene layers "Tan et al. (2004)", were observed.
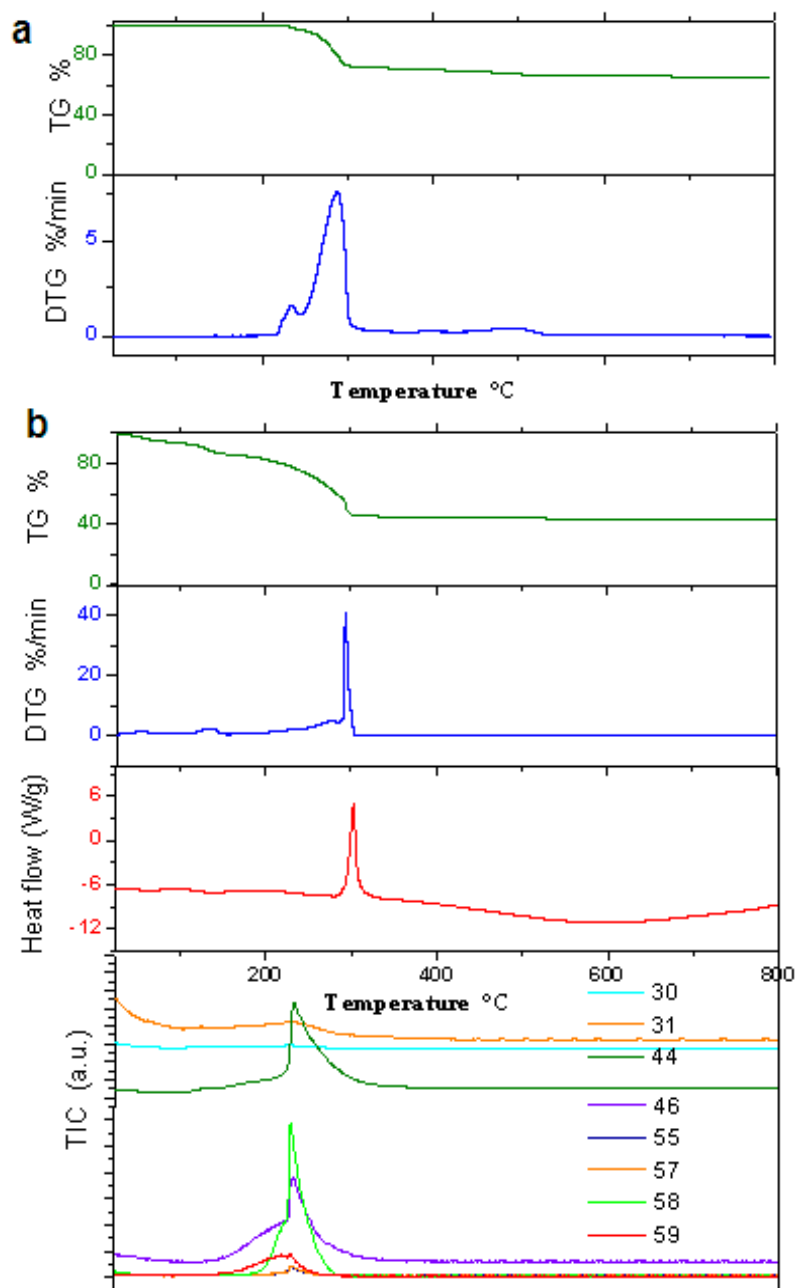
Figure VII.1 *TG-DTG of non impregnated gibbsite (a); TG-DTG-DSC-MS of impregnated gibbsite (b)*
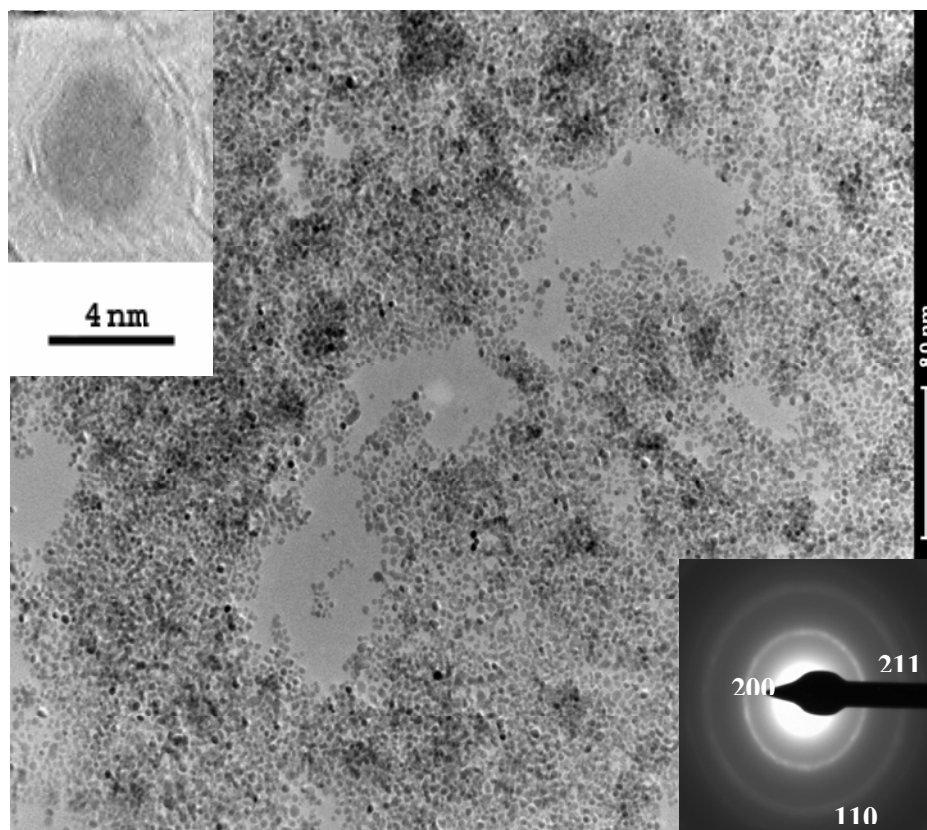
Figure VII.2 *TEM image of GCMNP1. The inserts in the figure show a nanoparticle covered by 1-2 layers graphene, and a selected-area electron-diffraction pattern*

a

2µm   Mag= 5.00 K X

b

a

EHT=15.00 kV   WD= 31 mm   Mag= 500 X
30µm   Photo No.=527   Detector= SE1
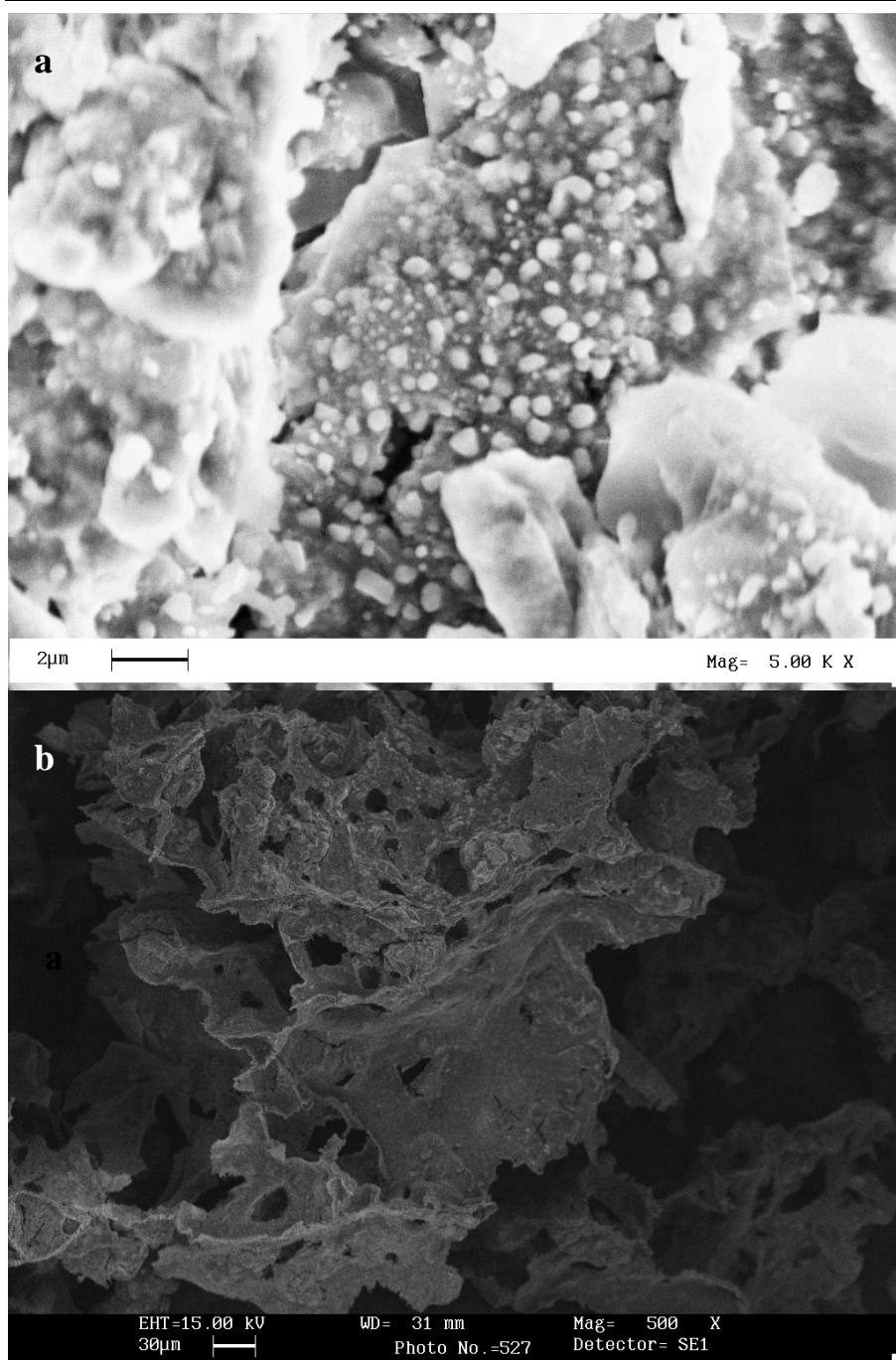
Figure VII.3 (a,b) *GCMNP1 SEM image (a), purified GCMNP1 SEM images at higher magnification (b)*
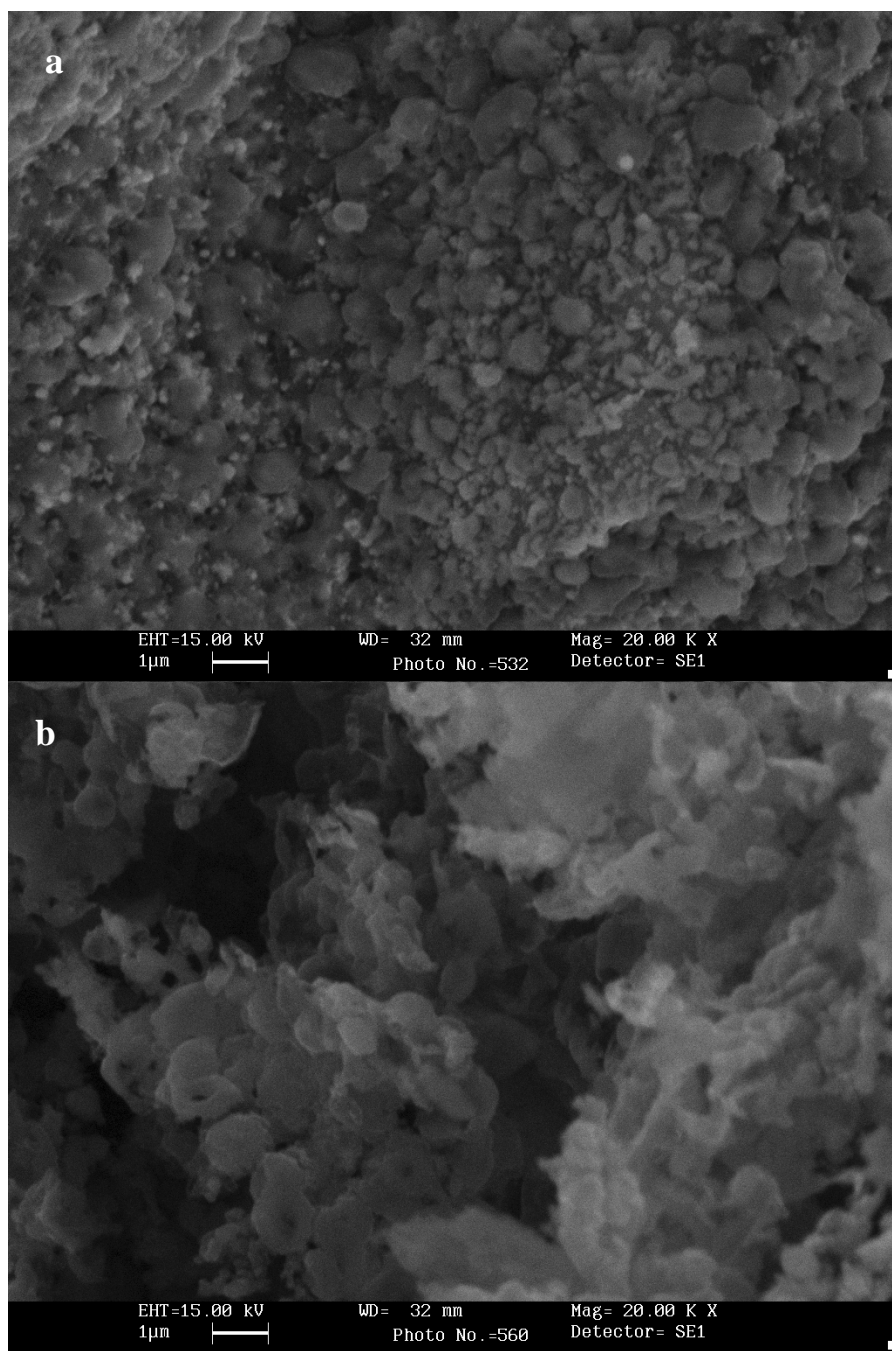
Figure VII.4 (a,b) *purified GCMNP1 SEM images at increasing magnification (a, b)*

a

b

c

d

Lorentz fit
Chi^2/DoF 2,6445E6
R^2   0,99552

Peak	Area	Center	Width	Height
1	9,5088E5	2647,9	58,920	10274
2	1,7304E6	2671,5	39,323	28014
3	2,7297E6	2690,3	41,844	41530
4	1,9124E6	2712,2	46,081	26421
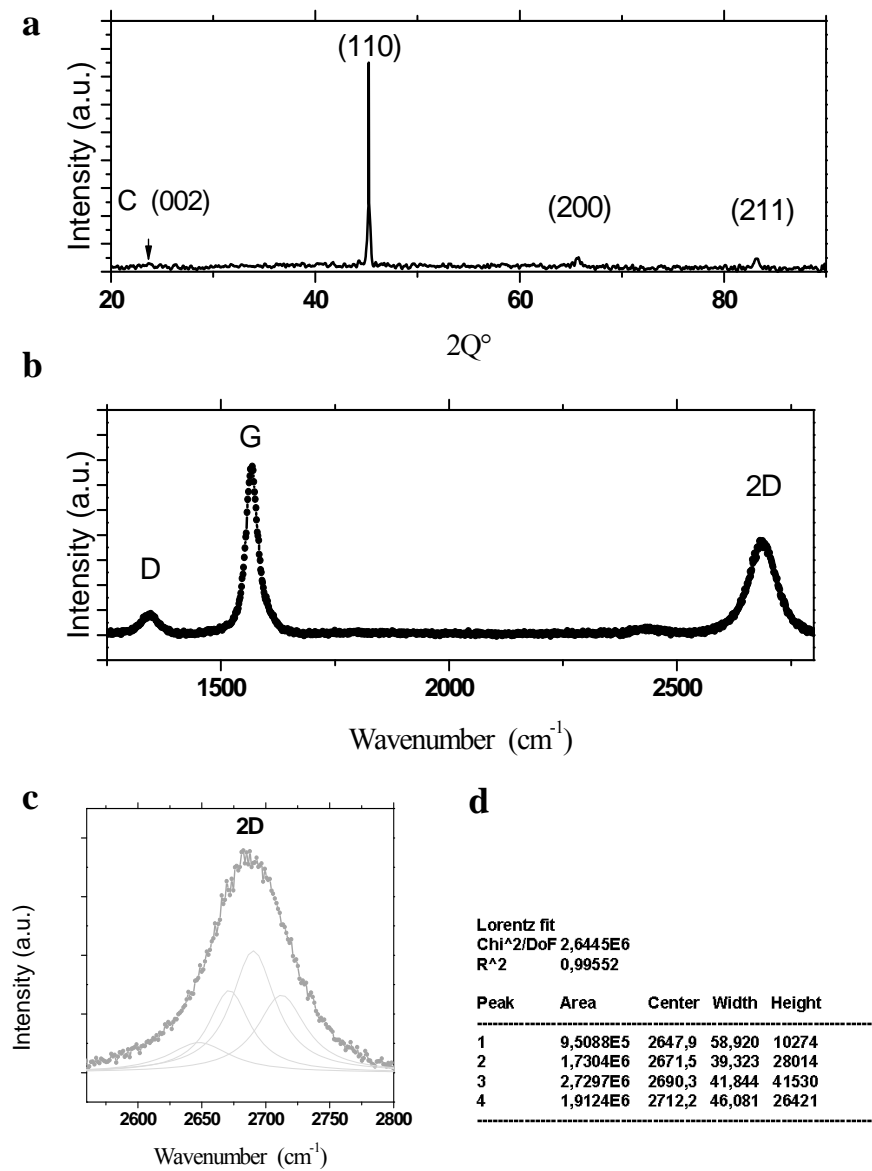
Figure VII.5 *X-ray diffraction pattern (a) and Raman spectrum (b) of GCMNP1. Lorentzian fitting of the 2D band (c) of the Raman spectrum GCMNP1 and details about the fitting (d).*

In Figure 5 (c, d), the Lorenzian fitting with four curves, as typical of 2 layer graphene "Malard et al. (2009)" is shown. The relevant details support the hypothesis of the good fit obtained.   The thermal stability of GCMNP1, after alumina removal, was investigated by thermogravimetric analysis in flowing air (Figure 6). The TG curve shows that after a slight weight loss of 1.35 wt. % at the initial stage due to the evaporation of the physisorbed water, the sample weight increases of 18.53 wt. % in the temperature range 350-750°C due the combined oxidation of C (see the mass fragments m/z=44) and metals "Wanga et al. (2012)". The total mass gain of the sample during the oxidation process suggests that the weight content of the graphene shells in the nanoparticles should be about 7.3 mg. The XRD pattern (not shown here) of GCMNP2 after alumina removal "Bystrzejewski (2011)"and after three weeks was found to be identical to that shown in Figure 5a, confirming the sample stability.

To understand the mechanism of the carbon coverage, the concentrations of CH_4, C_2H_2, C_2H_4 and H_2 in the effluent stream during the GCMNP1 reaction have been monitored via on-line analyzers. The relevant profiles are shown in Figures VII.7-8. We can distinguish three temporal phases: (I) Pre-reaction phase: the reaction gas is fed to the analyzers. The concentration of C_2H_4 and C_2H_2 are close to zero, while the initial methane and hydrogen concentrations are 10% v/v and 90% v/v, respectively. (II) Reaction phase: the gases are fed to the reactor and reach the analyzers after passing through the catalyst bed. After the time necessary to traverse the reactor and accounting for the delay time of the analyzers, the methane and hydrogen concentrations were 8.85% v/v and 93.98% v/v, respectively. No significant C_2H_4 and C_2H_2 concentrations are detected during the entire run time at the chosen temperature. (III) Post-reaction phase: the gases are sent directly back to the analyzers (bypassing the reactor). The concentrations of the four gases are the same as those in the pre-reaction phase.

The methane conversion and hydrogen yield were calculated by assuming that the methane conversion to carbon and hydrogen was the primary reaction:

$CH_4 \rightarrow C + 2\ H_2$.
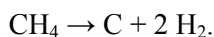
Based on this reaction the methane conversion and hydrogen yield can be expressed as:

$$X_{CH4} = \frac{1 - \dfrac{C_{CH4}}{C^0_{CH4}}}{1 + \dfrac{\varepsilon_{CH4} \times C_{CH4}}{C^0_{CH4}}}$$

(VII.3)

$$R_{H2} = \frac{(1 + \varepsilon_{CH4} X_{CH4}) \times C_{H2}}{2C^0_{CH4}}$$

(VII.4)

where C is the current concentration, C^0 is the initial concentration of a single component and εCH_4 expansion volume factor.

After the transient phase, the observed agreement between the CH_4 conversion (x_CH_4) and the H_2 yield (R_H_2) curves (see Figure VII.7 for the profiles of CH_4 conversion and H_2 yield) confirms the previously mentioned hypothesis that the catalyst resulted in the selective formation of carbon and hydrogen.

To better understand the catalytic activity, a blank test was performed by recording the evolution of the reactor's exhaust gas composition in the absence of the metal catalysts (sample Al1 in Table VII.2). The evolution of the concentration profiles of the exhaust gases in the presence of non-impregnated gibbsite (Figure VII.8) indicates a lack of methane decomposition in the absence of the catalysts in these operating conditions, and the C_2H_4 and C_2H_2 concentrations were close to zero. Starting with the hydrogen produced from the catalytic decomposition of methane during the GCMNP1 test, the total deposited carbon was calculated to be 7.5 mg, which corresponds to a mean deposited carbon mass of 0.025 mg/sec. It is important to note that this value is very close to the saturation threshold limit for the Co/Fe alloy, gC/gFeCo = 0.45 at.% at 800°C corresponding to 0.026 mg of carbon. Therefore, after the formation of GCMNPs during the pretreatment step, carbon saturation was achieved in approximately 1 sec. After 1 sec, carbon begins to cover the nanoparticle via carbon supersaturation and continuous precipitation from the cluster to form the graphitic structure. When the reaction was terminated, the catalyst remains active, and the carbon coverage phenomenon terminates when complete coverage of the GCMNP is achieved resulting in inactivation of the metal. The residual carbon mass inside the GCMNPs, which precipitated during the cooling phase, will contribute to the complete coverage of the metal "Seo et al. (2006)".
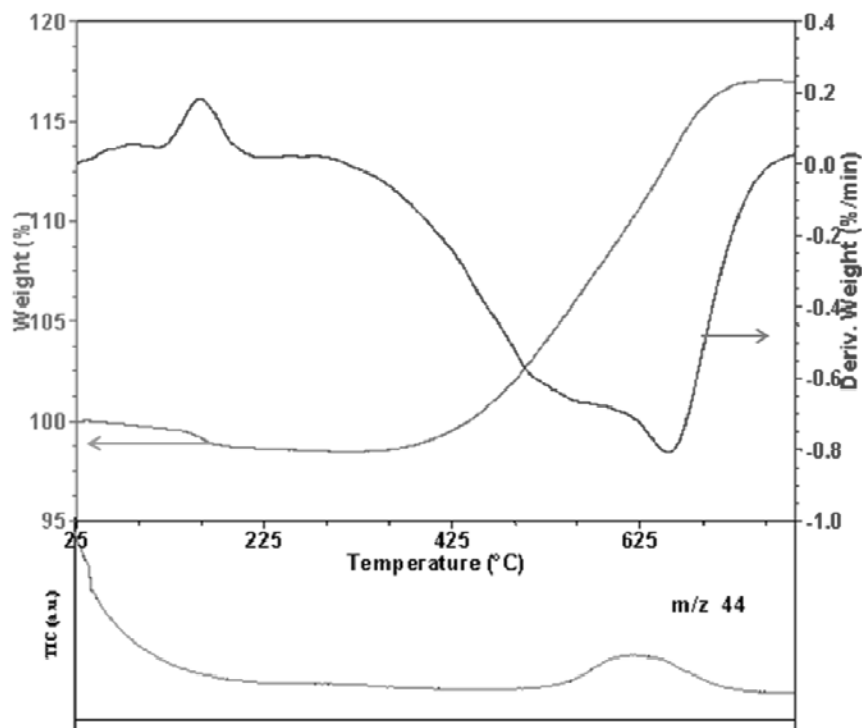
Figure VII.6 *TG-DTG_MS analysis of GCMNP1 after alumina removal*

The characterization of GCMNP1 indicates good homogeneity of the product along the reactor bed.

Very small body-centered-cubic-Co/Fe nanoparticles (4.1 nm mean diameter) with a very narrow distribution selectively covered by 1-2 graphene layers have been prepared. The hydrocarbon conversion is approximately 15%. It is important to note that there is no methane conversion in the absence of the metal catalyst on the support.

This result was determined by analyzing a series of critical parameters, such as feed composition, total feed flow, catalyst mass, hydrocarbon concentration, and pretreatment conditions, as described below.
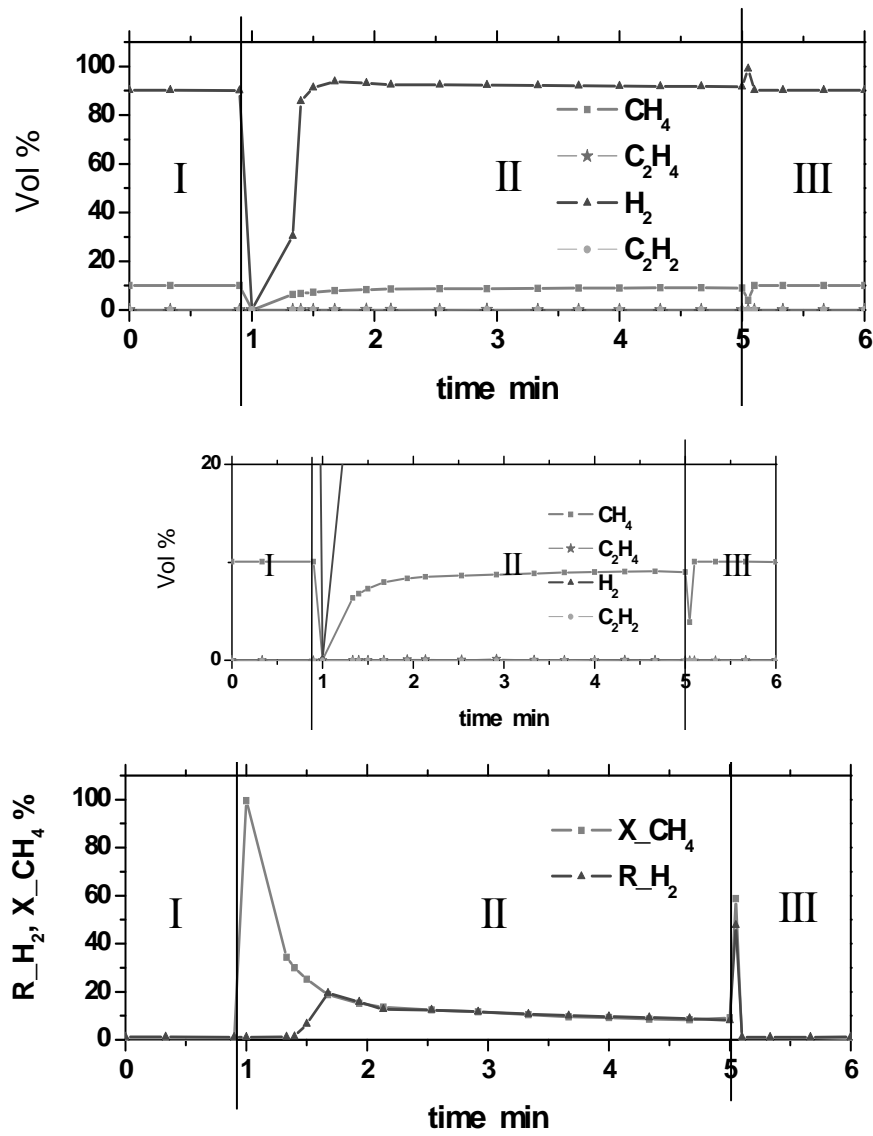
Figure VII.7 *On line analysis and CH₄ conversion and H₂ yield during the test: for GCMNP1 synthesis*
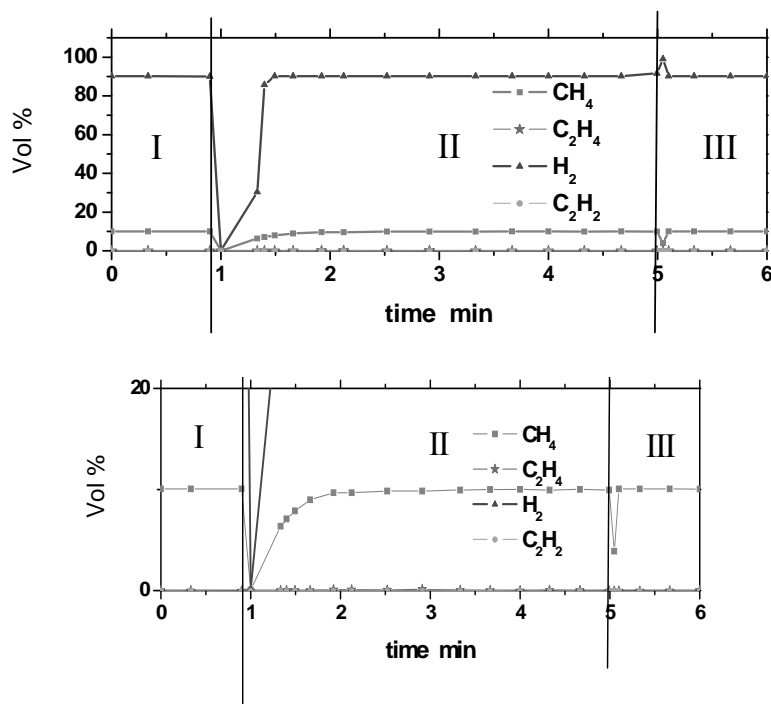
Figure VII.8 *On line analysis and CH$_4$ conversion and H$_2$ yield during the test in presence of non impregnated gibbsite treated as GCMNP1 (sample Al1 in Table 2)*

VII.3.3 The effect of the absence of the carrier gas

In the following discussion, the results related to GCMNP2, which was prepared under a pure CH$_4$ flow, are reported.

The concentration profiles of CH$_4$, C$_2$H$_2$, C$_2$H$_4$ and H$_2$ during a synthesis test for the GCMNP2 synthesized at 800°C under 100% v/v of methane is shown in Figures VII.9-10.

After the transient, the agreement between the CH$_4$ conversion (x_CH$_4$) and the H$_2$ yield (R_H$_2$) curves (see Figure VII.9 for the profiles of CH$_4$ conversion and H$_2$ yield) indicates that the catalyst was also selective for the formation of carbon and hydrogen.

In particular, a step after the first 0.7 minutes of the synthesis is observed, indicating a change in the catalytic behavior. To explore this phenomenon

and to better understand the catalytic activity, blank tests were performed by recording the evolution of the reactor's exhaust gas composition to determine the behavior of the system in the absence of a catalyst. The conditions employed involved the use of an empty reactor and the presence of non-impregnated gibbsite. The results are shown in Figures 10a and 10b, respectively.

For the empty reactor, the evolution of the concentration profiles of the exhaust gases indicates weak homogeneous methane decomposition, and C_2H_4 and H_2 "Guéret et al. (1997)" were observed. In addition, the reactor walls in the higher temperature zone are visibly gray after the synthesis. In the test with the non-impregnated gibbsite, the patterns in the concentrations of methane and hydrogen recorded at 800°C (Figure VII.10b) differed compared to those recorded during the empty reactor test. Methane conversion and a more significant hydrogen formation, which indicated carbon deposition, can be observed in the first few minutes of the synthesis. After a certain time, the evolution of the concentration profiles nearly overlaps that shown during the GCMNP2 synthesis. Therefore, in these experimental conditions, the activity of the catalyst metal nanoparticles starts to decrease after approximately 0.7 minutes of synthesis, and the other phenomena continue due to the catalytic surface of the alumina and the temperature. Therefore, under these experimental conditions, the carbon coating of the catalyst nanoparticles is most likely completed during the first synthesis phase (partially during the transient phase) along with simultaneously hydrocarbon decomposition that is partially catalyzed by alumina. Based on the methane conversion and hydrogen yield (Figure VII.10b) for non-impregnated gibbsite treated as GCMNP2 (Sample Al2 in Table VII.2), the amount of carbon deposited was determined to be 12.8 mg of carbon.

Further information was acquired from the TG-DTG analysis of GCMNP2, as shown in Figure VII.11.

First, the oxidation of carbon occurs as two main step losses centered at 330°C and 567°C, which indicate that the decomposition of methane led to the formation of nearly two different carbon phases (as indicated by the corresponding total ion current (TIC) of mass fragments $m/z = 44$ due to CO_2). Above 100°C, the first weight loss is due to the release of water.

The amount of deposited carbon was evaluated by determining the weight loss of the sample in the temperature range at which carbon burns in air (i.e., the two weight loss steps due to carbon oxidation) and considering the thermogravimetric residue, which is the weight of the catalyst (alumina+metal oxides) remaining after burning at 800°C. The carbon amount based on the 125 mg of impregnated gibbsite loaded into the reactor, was calculated to be 23.6 mg. Finally, based on the ratio between the two

carbon weight losses, a loss of 13.4 mg of carbon was calculated for the temperature range of 230-430°C, which is a carbon mass that is consistent with that determined by the evolution of the exhaust gases for the test with the non-impregnated gibbsite under the same operating conditions.
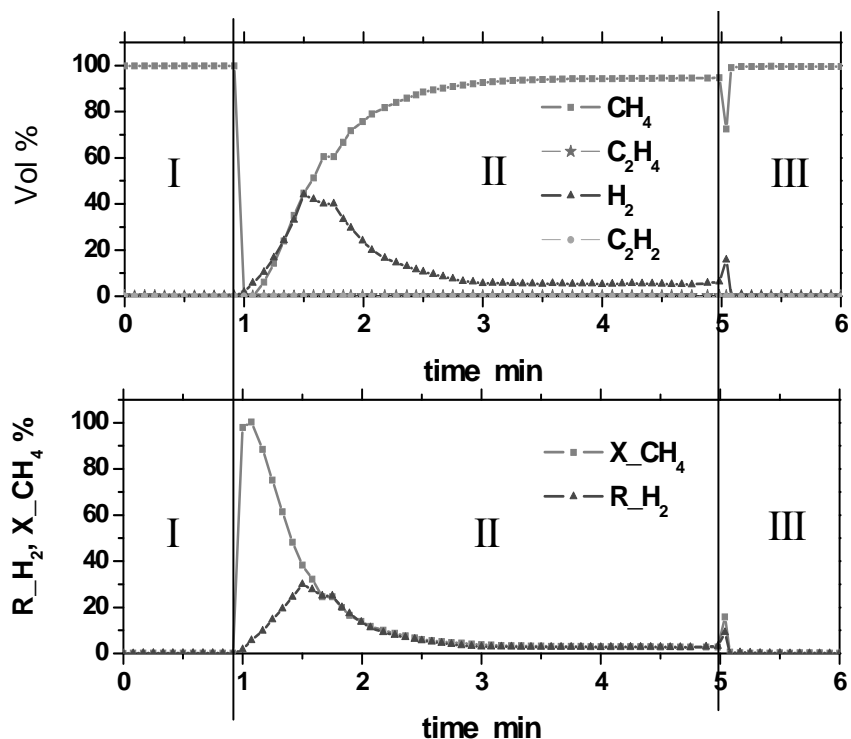
Figure VII.9 *On line analysis and CH$_4$ conversion and H$_2$ yield during the test for GCMNP2 synthesis*
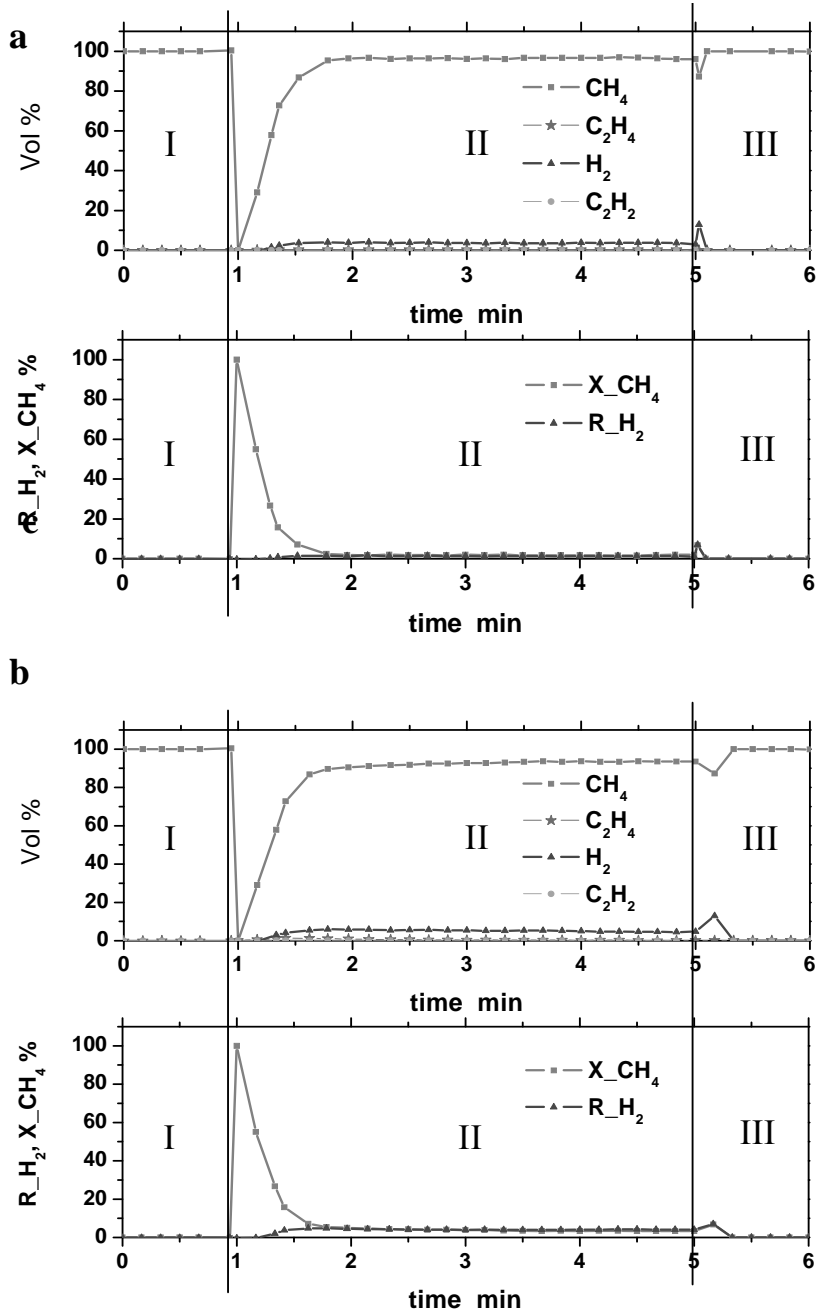
Figure VII.10 *On line analysis and CH$_4$ conversion and H$_2$ yield during the test: for an empty reactor (a); and in presence of non impregnated gibbsite, treated as GCMNP2 (Al2 in Table VII.2)(b)*
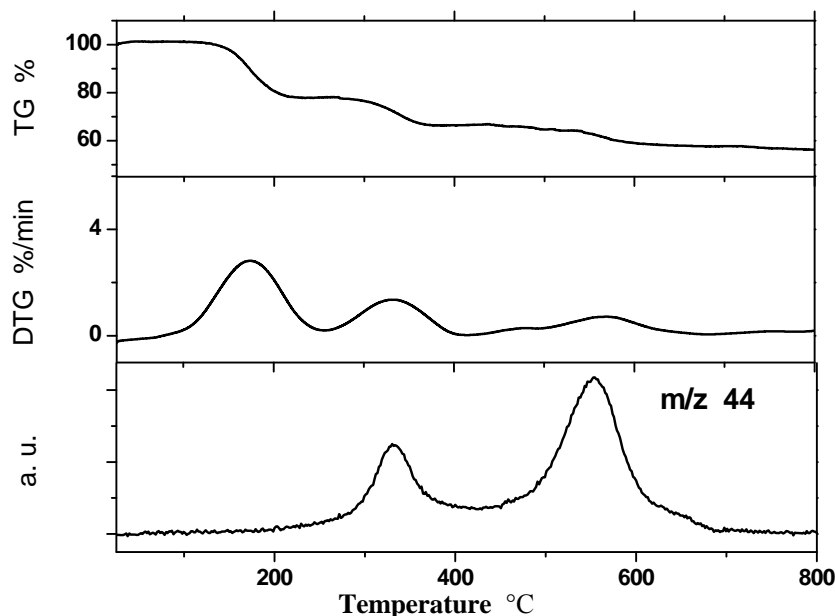
Figure VII.11 *TG-DTG_MS analysis of GCMNP2*

After chemical etching to remove the alumina support, the SEM image of the GCMNP2 is shown in Figure VII.12a. The sample is composed of quasi-spherical aggregates with a size that ranges from a few nanometers to 500 nm. Some objects with faceted faces are also visible (indicated by the arrow in Figure VII.12a). Figure VII.12c shows the GCMNP2 image after an additional thermogravimetric test up to 425°C (Figure VII.12b) to remove the carbon that oxidized under the first weight loss at 330°C. It is important to note the facetted objects were not observed in the sample after the thermal oxidation, which indicates that they are due to the carbon coating of the alumina crystals.

Figure VII.13 shows typical TEM images of the synthesis end product. The low magnification image shows the aggregates observed by SEM, which are composed of nanoparticles and carbon (see the insert at higher magnification, where the nanoparticles are the black points and the carbon that does not cover the nanoparticles is visible as dark halos).
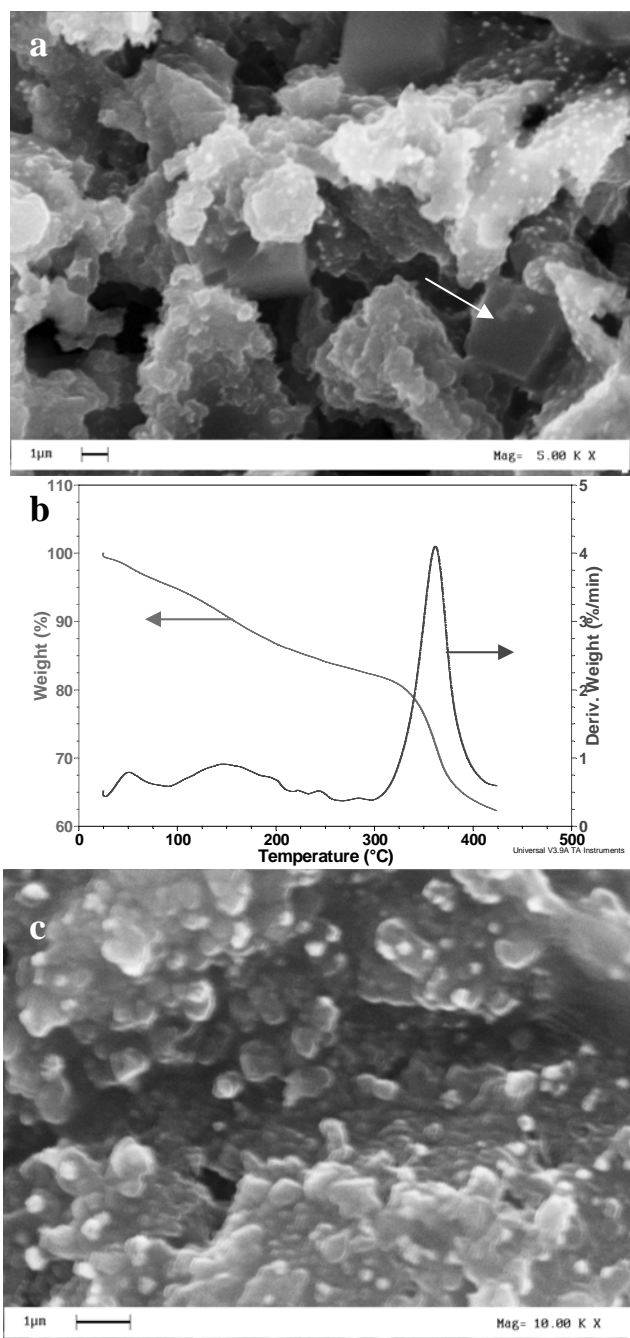
Figure VII.12 *SEM image of purified GCMNP2 (a); TG-DTG of purified GCMNP2 until 425°C (b); SEM image of purified GCMNP2 after the thermogravimetric treatment reported in b (c).*

At the highest magnification, it is possible to observe a core-shell nanoparticles that is approximately 5.5 nm in diameter. In addition, the image in the left-hand side box shows a magnification of the carbon layers that covered the alumina crystals during the GCMNP2 test, and remained in the sample after acid treatment of the alumina. However, the carbon that did not cover the nanoparticles appears to be present in the TEM images of the samples of ref. "Seo et al.(2006)", where homogeneous decomposition could not be excluded based on the residence time, temperature and feed composition.

To further confirm the nature of these carbon layers and to correlate it with the thermogravimetric results, a careful study of the material obtained from the test with the non-impregnated gibbsite treated the same as the GCMNP2 sample except in absence of methane (sample Al3 in Table VII.2) has been performed. In particular, in Figure VII.14a, the image of Al3 shows aggregates that are approximately a tens of microns in size. A low resolution TEM image (Figure VII.14b) of this sample (for the measurement a drop of the supernatant solution of the powder in ethanol was cast on a TEM grid) shows particles of approximately 1 μm and smaller. Finally, in Figure VII.14c, the hydrodynamic diameters of Al3 were determined by DLS. For the measurements Al_2O_3 dry powder was weighed and suspended in distilled water at a concentration of 0.5 mg/mL. This suspension was vibrated by vortex for 2 min and sonicated for 3 min to obtain a homogeneous suspension.

The DLS technique measures the Brownian motion (i.e., the random movement of particles due to bombardment by the solvent molecules that surround them) and relates this motion to the size of the particles. The size of the particle is calculated from the translational diffusion coefficient using the Stokes-Einstein equation:

$$d(H) = \frac{kT}{3\pi\eta D}$$

(VII.5)

where d(H) is the hydrodynamic diameter, D is the translational diffusion coefficient, k is Boltzmann's constant, T is the absolute temperature, and η is the viscosity.
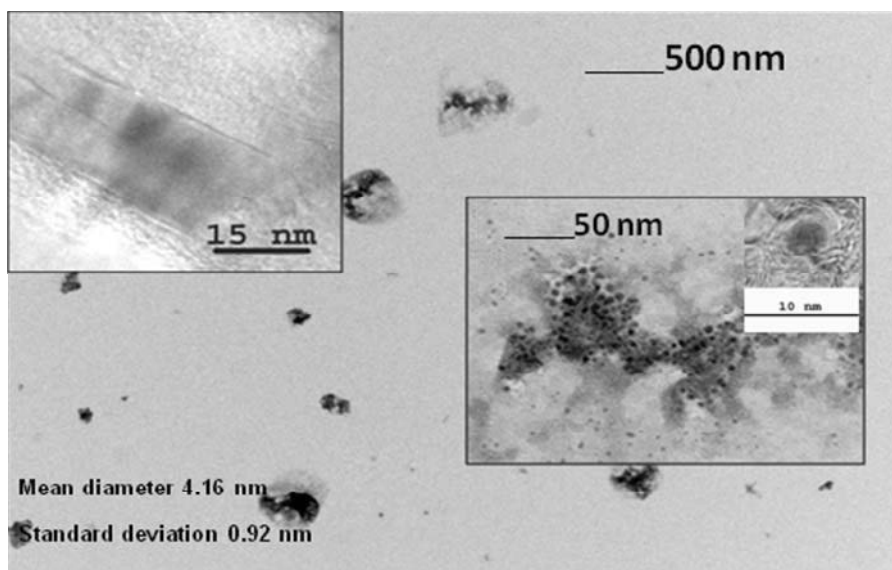
Figure VII.13 *TEM image of GCMNP2. The inserts in the figure show: the carbon layers generated by the alumina surface; nanoparticles at higher magnification; a nanoparticles covered by 5 graphene layers*

The diameter measured by DLS refers to how a particle diffuses within a fluid. Therefore, this value is referred to as the hydrodynamic diameter (i.e., the diameter of a sphere that has the same translational diffusion coefficient as the particle). The hydrodynamic diameters of the powder determined by DLS are 10.5 nm, 831 nm and 6.6 μm.

Based on the thickness of the carbon layer, the graphite density and the PSD distribution of Al3, a carbon deposition on the alumina surface was determined to be approximately 13 mg, which is in good agreement with the thermogravimetric results.
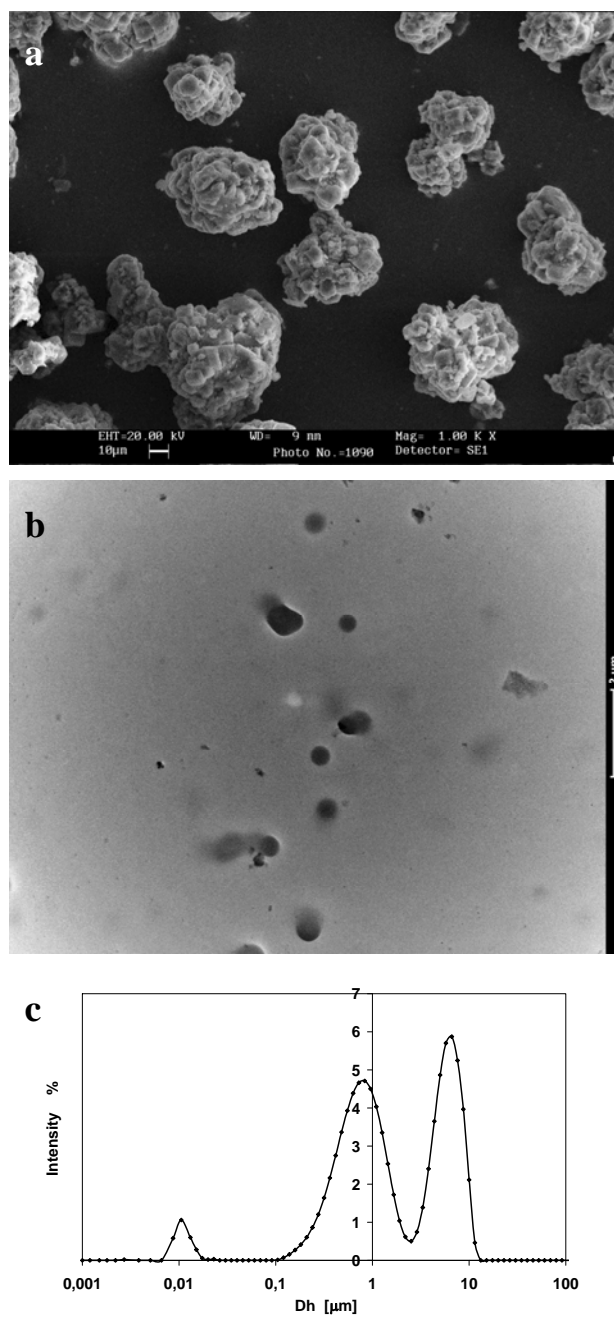
Figure VII.14 *Al3: SEM image (a), low resolution TEM image (for the measurement a drop of the supernatant solution of the powder in ethanol was casted on a TEM grid) (b), PSD as determined by DLS technique (c)*
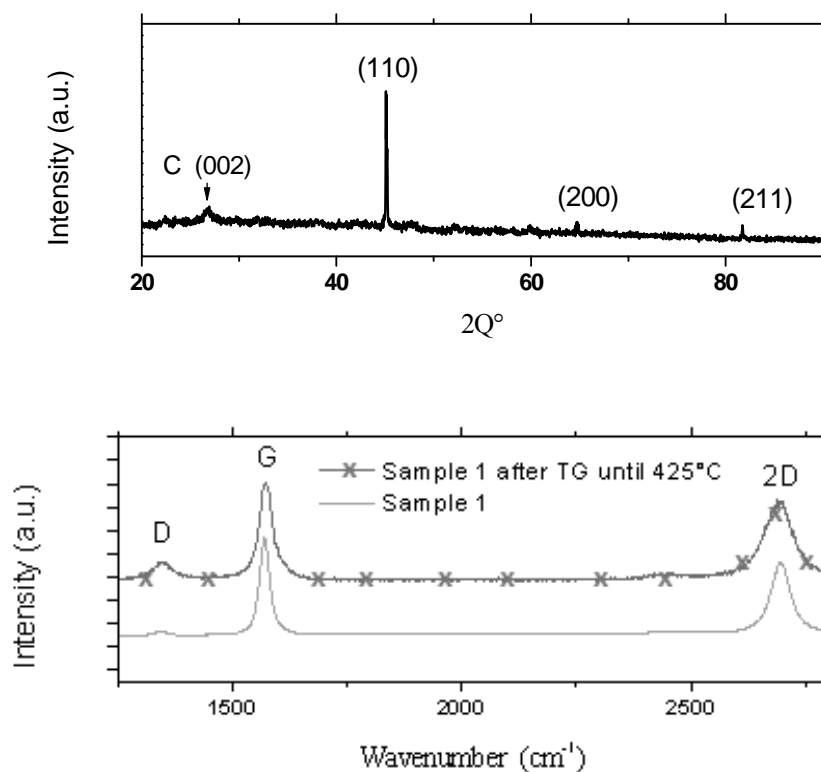
Figure VII.15 *X-ray diffraction pattern (a) and Raman spectra (b) of GCMNP2*

In Figure VII.15a, the X-ray diffraction pattern of the GCMNP2 is shown. The typical (002) reflection from the carbon along with the typical peaks for a crystalline body-centered-cubic FeCo alloy were observed.

Starting from the metal content in GCMNP2 (27.3 mg), the GCMNP mean diameter of 4.16 nm, and the metal GCMNP density of 8.2 g/cm^3, $9.2*10^{16}$ GCMNPs has been calculated. By multiplying the volume of the carbon spherical cap around the GCMNPs ($7.1*10^{-20}$ cm^3) for the GCMNP number and the carbon density, a deposited carbon mass of 10.5 mg has been obtained, which is in very good agreement with the carbon weight losses under the step centered at 567°C (see Figure VII.11).

85
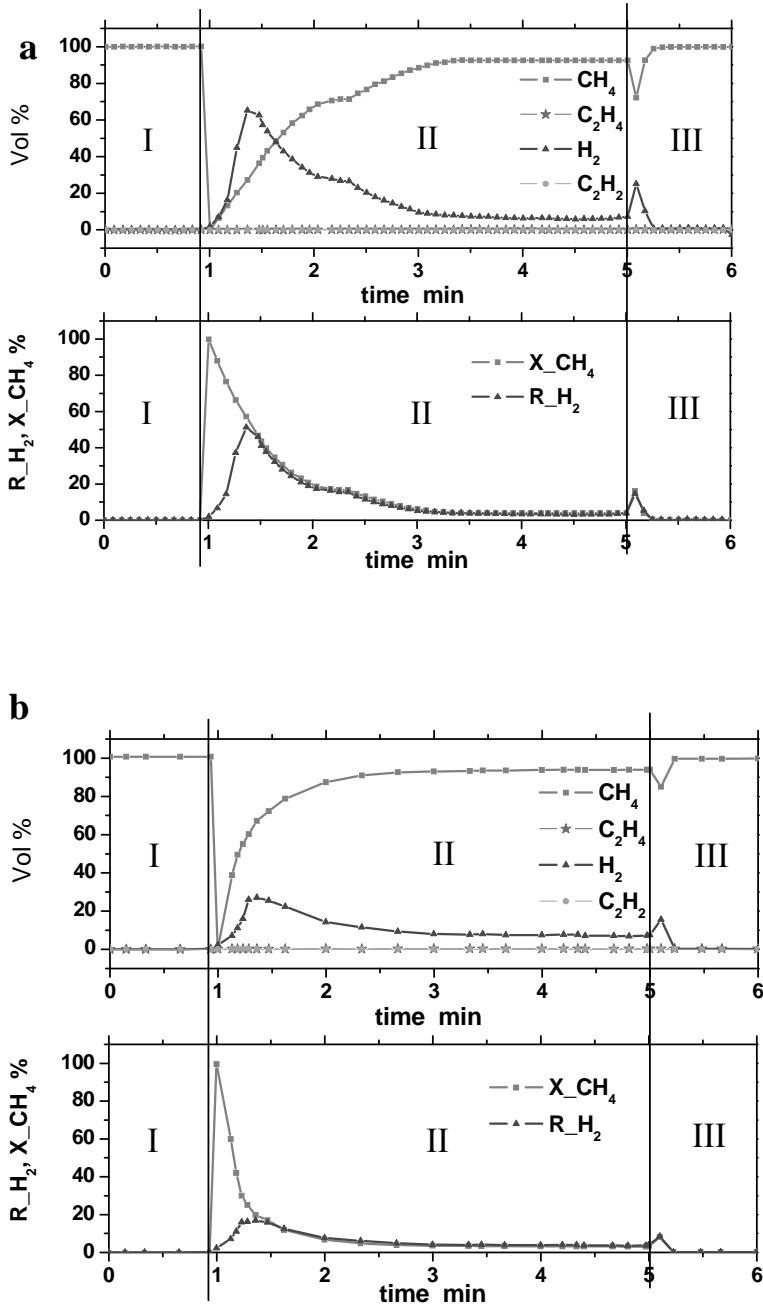
Figure VII.16. *On line analysis and CH₄ conversion and H₂ yield during the test: for GCMNP3 synthesis (a); for GCMNP4 synthesis (b)*

In Figure VII.15b, the Raman spectra of GCMNP2 are shown. In particular, the G band and the 2D band at approximately 2700 cm^{-1} were observed using an excitation wavelength of 514 nm. At room temperature, the 2D band exhibits a single Lorentzian feature with a full width at half maximum (FWHM) of 45 cm^{-1}. A broad D band due to disorder or the edge of a graphite sample was also observed at approximately half of the frequency of the 2D band (approximately 1350 cm^{-1} using 514 nm laser excitation). The Raman spectrum of GCMNP2 is also reported in Figure VII.15b after thermal treatment under thermogravimetric conditions up to 425°C for comparison. A broad 2D band and a more pronounced D band, as expected for more curved graphene layers "Tan et al. (2004)", was observed. The spectrum near overlaps that of GCMNP1 shown in Figure VII.5b.

VII.3.4 The effect of total feed flow, catalyst mass, feed composition

To evaluate the effect of the total feed flow, the GCMNP3 sample was prepared, as shown in Table VII.1, in which five samples have been chosen that are representative of the effects of the different experimental parameters. Under the same operating conditions but total feed flow (Figure VII.16a), a step is detected as observed during the GCMNP2 synthesis but after a longer time. This result indicated longer metal catalyst activity. In addition, the methane conversion is higher compared to that of GCMNP2. The TEM image of GCMNP3 in Figure VII.17 shows nanoparticles on a carbon carpet.

When the catalyst mass (GCMNP4) was increased, no step is observed during the entire run time. However, by feeding pure methane at 800°C (see Figure VII.10b for the behavior of Al2), homogeneous decomposition added up to the metal catalyst activity in the first few minutes of the synthesis. In addition, the differences in the results obtained for GCMNP3 and GCMNP4 indicate that the system does not work in a chemical regime and most likely the concentration gradient along the catalyst bed results in a lower hydrocarbon availability to the metal active phases. The catalyst is more slowly deactivated and a nonuniform product distribution along the catalyst bed was obtained. The TEM images of GCMNP4, which are not shown here, confirm this result as well as the presence of a carbon carpet under the nanoparticles.

The next step was to synthesize GCMNP5 with an increased catalyst mass and total flow. After the synthesis, the sample exhibited great disomogeneity along the catalyst bed thickness. In addition, the product color changed from

black to light grey depending on the proximity of the sintered reactor support due to diffusive limitations.

VII.3.5 The effect of the pretreatment

In Figure VII.18a, the isotherm of a sample obtained by treating non-impregnated gibbsite as follows (Al4 in Table 2): (i) drying at 80°C for 3 h; (ii) followed by a calcination at 400°C for 2 h; (iii) thermal treatment under nitrogen from 25°C to 800°C with a heating rate of 70°C/min; and finally in isotherm for 5 min at 800°C under nitrogen. The nitrogen adsorption–desorption isotherm of this sample is a type IV under BET classification, and the BJH pore size distribution is multimodal, as shown in Figure VII.18c.

For comparison, Figure VII.18b, the nitrogen adsorption–desorption isotherm of a sample obtained by treating non-impregnated gibbsite as follows, (to simulate typical process conditions, Al3 in Table 2): (i) drying at 80°C for 3 h; (ii) followed thermal treatment under nitrogen from 25°C to 800°C with a heating rate of 70°C/min; and finally in isotherm for 5 min at 800°C under nitrogen, is also reported. The pore distribution evaluated with the BJH method is monomodal with a relative maximum at 4.1 nm (Figure VII.4b), indicating that the pretreatment phase is fundamental to controlling the final Al_2O_3 pore size distribution and crucial for the final size of the GCMNPs .

To further confirm this conclusion, a TEM image of carbon nanotubes obtained from the same catalyst under the same operating conditions used for GCMNP1, but with 5 wt% Co/Fe on alumina is shown in Figure VII.19.

Due to the lower metal loading, nanoparticles that are 4 nm in diameter catalyzed the growth of carbon nanotubes.

The key factor that determines the formation of carbon nanotubes is the lack of the catalyst deactivation, which is the case when this is covered with carbon. To coat the nanoparticles with a protective coating, it is necessary to create conditions in which the catalyst goes towards the deactivation.

The formation of graphene at higher catalyst content indicates that the rate of carbon extraction from the hydrocarbon for each nanoparticle is lower.

This is probably due to a confinement effect generated by the larger number of nanoparticles, even if a lower availability of hydrocarbon for each nanoparticle, can not be excluded.
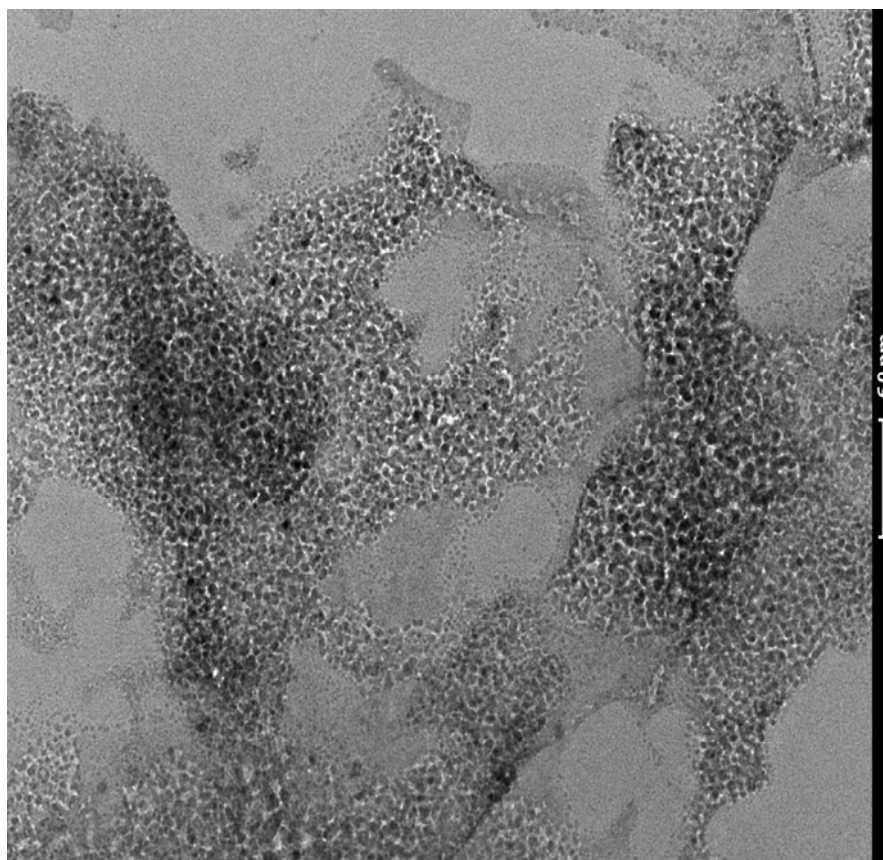
Figure VII.17 *TEM image of GCMNP3*

Finally, in Table VII.3, the surface areas of Al2, Al3, Al4, Al5 (see Table VII.2 for preparation details) and gibbsite are reported for comparison. The deposited carbon on the Al2 sample results in a lower surface area compared to Al3. The lower values for Al5 compared to Al3 are due to the metal filling, whose presence determines the micropore volume due to the spaces between the particles.

a

Isotherm Plot

[Isotherm plot, V [cc/g] vs p/po]

b

Isotherm Plot

[Isotherm plot, V [cc/g] vs p/po]

c

dVp/dDp Desorption Pore Volume Plot

[First derivative, dVp/dDp [mm3/g*nm] vs Pore diameter, Dp [nm]]

d

dVp/dDp Desorption Pore Volume Plot

[First derivative, dVp/dDp [mm3/g*nm] vs Pore diameter, Dp [nm]]

[Intensity (a.u.) vs 2Q°]
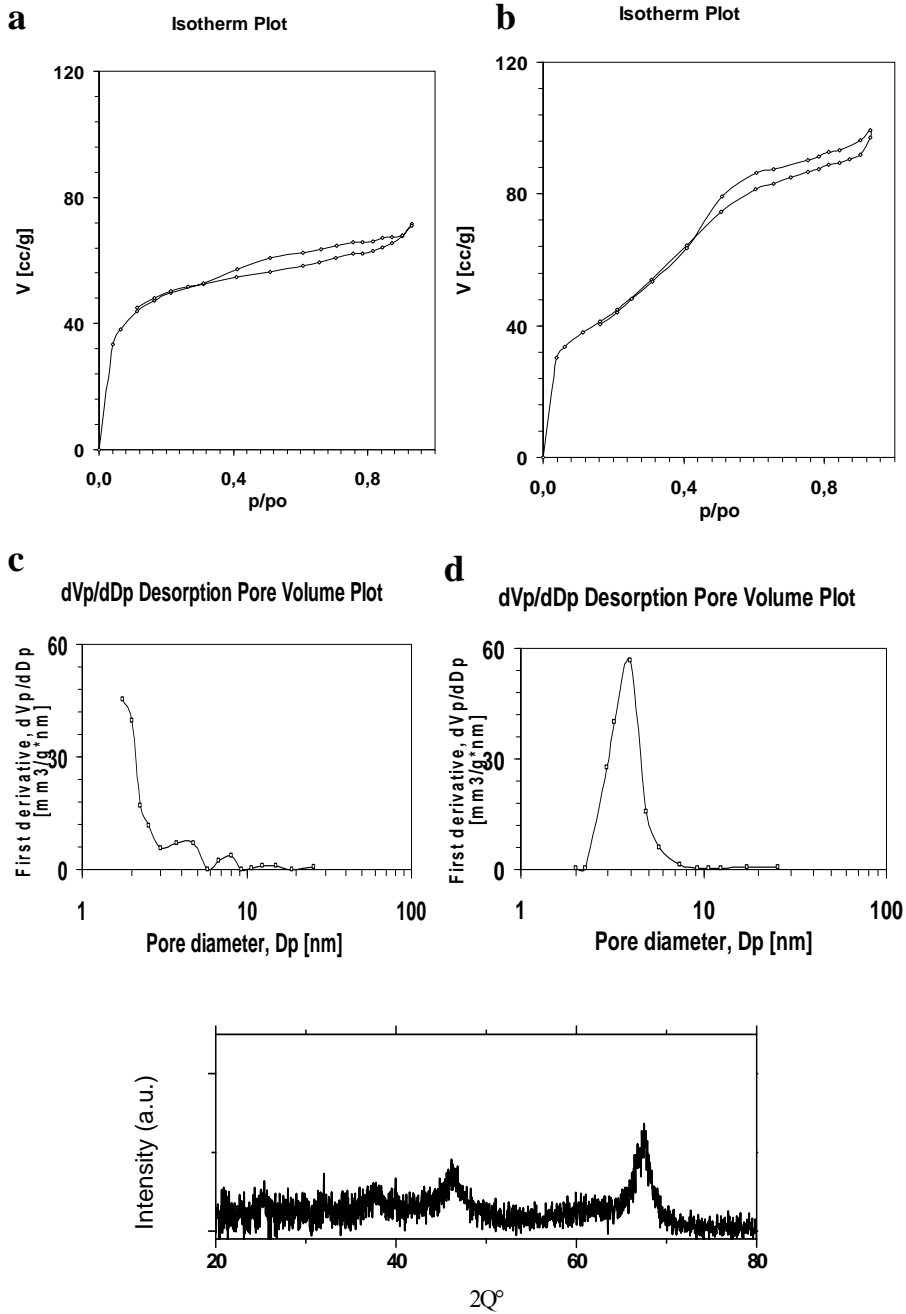
Figure VII.18. *N_2 adsorption-desorption isotherm (a) and BJH pore size distribution (c) of Al3. N_2 adsorption-desorption isotherm (b), BJH pore size distribution (d) and X-ray diffraction pattern (e) of Al4*
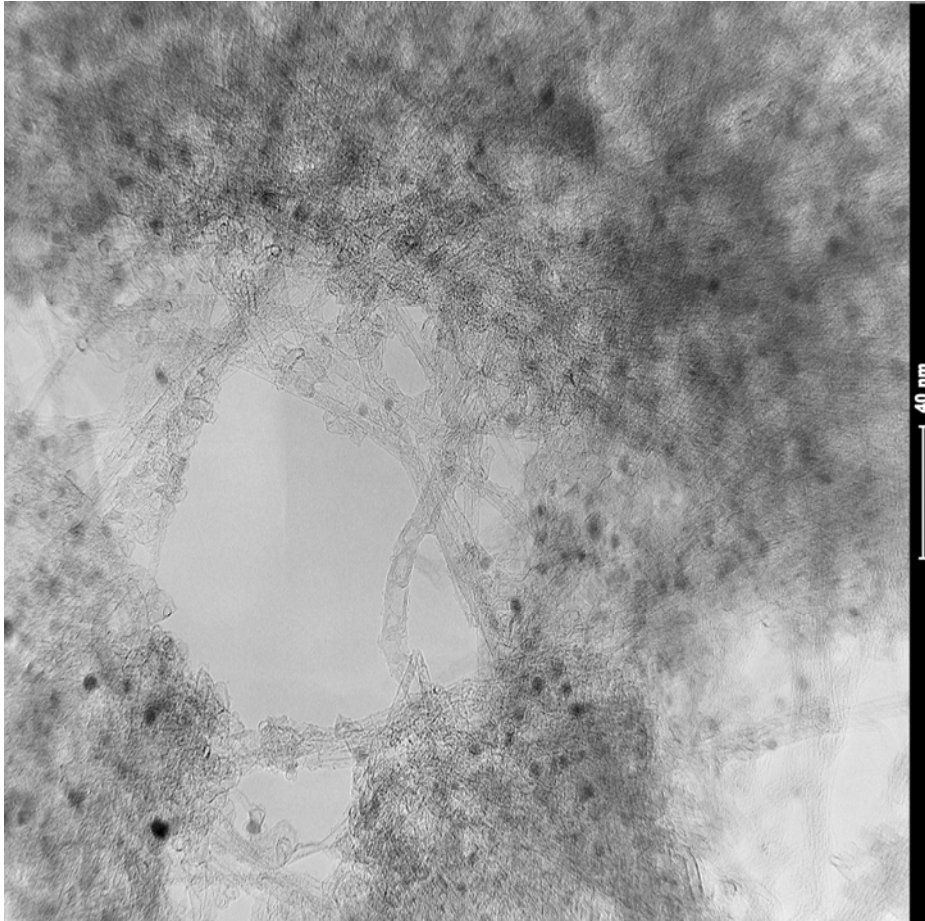
Figure VII.19 *TEM image of carbon nanotubes obtained in the same conditions GCMNP1 but metal catalyst loading*

Table VII.3 *BET and Langmuir surface areas and micropore volume*

Samples	BET Surface Area sq.m/g	Langmuir Surface Area sq.m/g	Micropore volume cub.mm/g
Al2	167.23	218.76	0.00
Al3	191.63	273.65	0.00
Al4	180.37	241.46	19.7
Al5	29.77	40.87	2.25
gibbsite	0.54	0.46	0.00

VII.4 Conclusions

Stable core-shell carbon-coated GCMNPs have been prepared by catalytic chemical vapor deposition (CCVD) in the presence of methane at atmospheric pressure on a Co/Fe catalyst. Under the experimental conditions investigated, alumina determines the GCMNP size and was used as a support to obtain very small body-centered-cubic-Co/Fe nanoparticles (4.1 nm mean diameter), with a narrow distribution of diameters.

The total flow rate, hydrocarbon partial pressure and catalyst weight are crucial to the selective coating of the nanoparticles and to the thickness of the coating. Moreover, to obtain homogeneous material, it is fundamental to control as much as possible the diffusive limitations. The use of a carrier prevents unwanted homogeneous decomposition and increases hydrocarbon conversion resulting in GCMNPs covered by two graphene layers and free of other carbon species.

Chapter VIII
Experimental V

Magnetic core-shell graphene coated Co/Fe synthesized nanoparticles

VIII.1 Introduction

In the last decades nanoparticles (NPs) have attracted great attention due to their fascinating chemical and physical properties. Because of the widespread applications of nanoparticles in biotechnology, biomedical, material science, engineering, and environmental areas, much attention has been paid to the synthesis of different kinds of NPs "Niemeyer (2001)". Among them, magnetic nanoparticles (MNPs) "Altavilla et al. (2009), Lu et al. (2007), Maaz et al. (2010) , Hütten et al. (2005), Fonseca et al. (2002), Mallick et al. (2007)" are of particular interest because the possibility to use in a wide number of fields, including catalytic, environmental, biomedical and electronic.

However, synthesizing stable MNPs and avoiding nonspecific binding are still challenging. Different strategies have been developed to solve this issue "Gaster et al. (2009), Kim et al. (2001), Nikolic et al. (2006), Yi et al. (2005), Santra et al. (2001)".

Carbon-coated MNPs due to high chemical and thermal stability, as well as biocompatibility of carbon-based materials are very promising. Moreover, carbon-coated nanoparticles are usually in the metallic state, and compared to the corresponding oxides have a higher magnetic moment "Lu et al. (2007)". Magnetic nanoparticles of Ni, Co, Fe and their alloys, coated with different carbon coating strategies and tested with respect to their magnetic properties "He et al. (2006), Dumitrache et al. (2004), Chen et al. (2012), Niemeyer (2001), Altavilla et al. (2009)", have been prepared.

CVD technique offers the advantage to be easiest scale up towards an economically viable production "Chen et al. (2012)".

Carbon-encapsulated nanoparticles, formed by CVD over Ni/Al catalyst, free of by products such as carbon nanotubes/nanofibers, carbon nanoparticles and amorphous carbon and of agglomeration phenomena have been obtained by He et al. "He et al. (2006)" in 2006. The nanoparticles have a diameter of 15 nm, the superparamagnetism ensured by the carbon coating, a saturation magnetization (Ms) value of 13.42 e.m.u./g (bulk nickel 55 e.m.u./g). Lower size MNPs synthesis has been reported by Seo et al. "Seo et al. (2006)". Co/Fe MNPs alloy formed on silica, of 7 and 4 nm, covered by 1-2 layer graphene, were tested as advanced magnetic-resonance-imaging and near–infrared agents "Seo et al. (2006)", and more recently for Few-Cells enrichment and detection "Chen et al. (2012)". They found, for their body-centered-cubic-NPs of 7 nm diameter the highest saturation magnetization (Ms=215 e.m.u./g, close to the bulk FeCo = 235 e.m.u./g) obtained for nanocrystal, and despite the smaller size a lower value for the 4 nm NPs, likely due to the presence of a mixed body-centered-cubic-FeCo and face-centered-cubic-Co phases.

A detailed study of the effects of operating conditions, such as: feed gas composition, total flow-rate, catalyst mass, metal catalyst weight, and catalyst pretreatment, on the preparation of Co/Fe nanoparticles covered by few layer graphene by catalytic chemical vapor deposition (CCVD) of methane at atmospheric pressure on Co-Fe alumina supported catalyst, has been reported by Sarno et al. "Sarno et al. (2014)". Stable core-shell graphene coated magnetic nanoparticles (GCMNPs) (~ 4.1 nm very little diameter), with a narrow distribution of size and by-product free, have been prepared "Sarno et al. (2014)".

The NMPs magnetic properties strongly depend by their size "Lu et al. (2007)". On the other hand, it was identified, in our experimental conditions, the key role of the final support porosity, that can be controlled by the catalyst pretreatment, in determining the NMPs size. In this chapter, the influence of the pretreatment conditions on the final alumina pore size distribution and GCMNPs diameter, obtained by (CCVD) of methane at atmospheric pressure, on Co Fe alumina supported catalyst was reported. The pretreatment was performed either in H_2 or in N_2. The magnetic properties of the nanoparticles in both cases, were studied, an Ms value of 230 e.m.u./g, was found, for these monodispersed 4.1 nm diameter body-centered-cubic-FeCo nanoparticles.

Different techniques were used to characterize the nanoparticles: transmission electron microscopy (TEM), scanning electron microscopy (SEM), Raman spectroscopy, X-ray diffraction analysis and N2 adsorption–desorption at 77K. The magnetic measurements have been performed by using a Quantum Design PPMS 9T equipped with the Vibrating Sample Magnetometer (VSM) option. For the first time, for Co/Fe graphene coated magnetic nanoparticles, M~H curves were presented together with M~T

profiles, to obtain deeper information about the magnetic behaviour of the nanoparticles.

VIII.2 Materials and methods

VIII.2.1 Catalyst preparation

The Co, Fe catalyst (50 wt.% of each metal) was prepared by wet impregnation of gibbsite (γ-Al(OH)$_3$) powder "Sarno et al. (2014), Sarno et al.(2012a), Giubileo et al. (2012)" with cobalt acetate and iron acetate solution and then drying at 80°C for 3h.

VIII.2.2 Carbon coated nanoparticles preparation

CCVD was carried out in a continuous flow microreactor fed by a methane–hydrogen gas mixture. The microreactor was a quartz tube (16 mm internal diameter, 300 mm length), and the catalyst (particles size in the range 38-53 μm, sieved before the syntheses) was loaded on a sintered support "Sarno et al. (2014), Sarno et al.(2012a), Giubileo et al. (2012), Sarno et al. (2013), Sarno (2012b)". An external, coaxial quartz tube (35 mm internal diameter) allowed the reactant stream to be preheated. The temperature of catalyst bed was measured with a K thermocouple located inside a third, internal, coaxial quartz tube (4 mm internal diameter). The reactor was heated by an electrical oven whose temperature was controlled by a temperature programmer–controller (Eurotherm 2408). Cylinder gases (99.998 pure methane and 99.9990 pure hydrogen) were mixed to obtain the methane/hydrogen stream that was fed to the reactor. A constant flow rate of each gas was provided by mass flow controllers. The experimental plant for the synthesis was equipped with on-line analyzers (Uras 26, ABB) that permit to monitor alternatively the inlet and outlet reactor concentrations of reactants (methane, CH$_4$ and hydrogen, H$_2$) and products (acetylene, C$_2$H$_2$; ethylene C$_2$H$_4$, and hydrogen, H$_2$), continuously during the reaction, operating a by-pass valve.

The typical procedure for preparing GCMNP particles includes: (1a) feeding the reacting gas to the analyzers to verify the steady state inlet concentration; (1b) N$_2$ is fed to the reactor by another feed line to pre-treat the catalyst; (2) the pre-treatment nitrogen flow was stopped using the bypass valve, and the reacting gas stream was started to feed the reactor; (3a) after 5 min, the reacting gas stream was stopped, and nitrogen was fed to the reactor; next, (3b) the reacting gas is fed to the analyzers; (4) the reactor was extracted

from the furnace and allowed to cool under ambient temperature conditions; (5) chemical attack to separate the GCMNPs from alumina.

The catalyst was preheated before starting the CCVD process at 70 °C/min up to the synthesis temperature either in H_2 or in N_2 (respectively named GCMNPH2 and GCMNPN2), then a $400 cm^3$/min flow rate of 10% methane in hydrogen was introduced in the reactor during 5 min.

VIII.2.3 Characterization techniques

SEM pictures were obtained with a LEO 1525 microscope. TEM images were acquired using a FEI Tecnai electron microscope operated at 200 KV with a LaB6 filament as the source of electrons. The preparation of samples for TEM observation involved sonication in ethanol for 2-5 minutes and deposition of the sample on a carbon grid.

Raman spectra were obtained at room temperature with a microRaman spectrometer (Renishaw inVia; 514 nm excitation wavelength).

XRD measurements were performed in the 2Θ range of 20-30° with a Bruker D8 X-ray diffractometer using $CuK\alpha$ radiation.

Surface area and porosity characterisation was obtained by N_2 adsorption–desorption at 77K with a Kelvin 1042 V3.12, COSTECH Instruments. Powder samples were outgassed in He flow at 250°C for 3h before measurements.

VIII.2.4 Magnetic nanoparticles characterization

All the magnetic measurements here reported have been performed by using a Quantum Design PPMS 9T equipped with the Vibrating Sample Magnetometer (VSM) option. The measurements temperature range goes form 2.5 K to 350 K, and DC magnetic fields up to about 4 T maximum have been applied, paying attention to avoid any field overshoot which could modify without control the initial magnetic state of the samples "Zola et al. (2004)". Moreover, a particular care has been put in order to delete the effect on the used material of an eventual magnetic history, by heating the sample at the temperature of 350 K for about 20 minutes before each measurement, while performing demagnetisation cycles on the superconducting magnet of the PPMS so that its trapped field is reduced to about 2 Oe.

VIII.2.4.1 ZFC and FC measurements procedure

Dc Magnetisation measurements as function of the temperature M(T) have been performed in Zero Field Cooling (ZFC) and in Field Cooling (FC) conditions. More precisely, the sample is first cooled down to a low temperature (around 2.5 K) in absence of any magnetic field, and then it is thermally stabilised for 20 minutes. After that, the field is applied and then the measurement is taken for increasing temperature (ZFC) up to a final value(around 350 K), with a rate of 1K/min. Finally, still leaving the same field on, the measurement is performed by cooling down the sample (FC) back to the starting temperature.

VIII.2.4.2 M(H) measurements procedure at different temperature

The measurements of the magnetization loops (M vs H loops) have been performed at different temperatures, and in particular at 300 K and at 5 K. In order to do this, the temperature are first fixed at a given value in zero magnetic field and the sample is thermally stabilised for about 20 minutes to avoid thermal hysteresis. Then the field is applied up to a maximum value of H_{max} and back to - H_{max} and then again to H_{max} and finally to zero, while the corresponding magnetization M is detected. After this measurements, before performing other similar measurements, the sample magnetic history is cancelled by warming it at the temperature of 350 K every time.

VIII. 3 Results

VIII.3.1 GCMNPs characterization

Figure VIII.1 shows the typical TEM pictures of purified GCMNPH2. GCMNPH2 image shows some particles with a size distribution in the range 3-7 nm and a narrower one between 7 and 10 nm. The distribution of GCMNPN2 size (Figure VIII.2) results monomodal with an average diameter of 4.1 nm, 0.79 nm standard deviation, as measured for ~400 nanocrystals). Furthermore, the contrast of the TEM image of individual particles clearly shows the GCMNP has a core-shell structure, indicating the encapsulation of the metal particles by carbon (1-2 layers graphene, see the HRTEM insert in the same figure).

SEM characterization shows that GCMNPs are constituted of particles (that are GCMNPs aggregates), with size of about 1 μm, on the alumina surface (Figure VIII.3a and Figure VIII.3b, for GCMNPH2 and GCMNPN2, respectively). To better understand the nature of these particles, in the same

figure (Figure VIII.3c-e), images of non impregnated gibbsite treated through: (i) a drying at 80°C for 3 h; (ii) followed thermal treatment under nitrogen from 25°C to 800°C, 70°C/min; and (ii) finally in isotherm for 5 min at 800°C under nitrogen (AlN2), are also reported. AlN2 is constituted of aggregates that are approximately a tens of microns in size. A low resolution TEM image of Al2 (Figure VIII.3d) (for the measurement a drop of the supernatant solution of the powder in ethanol was cast on a TEM grid) shows particles of approximately 1 μm and smaller.

Finally, in Figure VIII.3e, the hydrodynamic diameters were determined by DLS. The DLS technique measures the Brownian motion (i.e., the random movement of particles due to bombardment by the solvent molecules that surround them) and relates this motion to the size of the particles. The size of the particle is calculated from the translational diffusion coefficient using the Stokes-Einstein equation:

$$d(H) = \frac{kT}{3\pi\eta D}$$

where d(H) is the hydrodynamic diameter, D is the translational diffusion coefficient, k is Boltzmann's constant, T is the absolute temperature, and η is the viscosity.

The diameter measured by DLS refers to how a particle diffuses within a fluid. Therefore, this value is referred to as the hydrodynamic diameter (i.e., the diameter of a sphere that has the same translational diffusion coefficient as the particle). The hydrodynamic diameters, of the AlN2 powders, determined by DLS are 10.5 nm, 831 nm and 6.6 μm. Thus, the AlN2 powders have size distributions in the range 100 nm-2μm and smaller between 9 and 11 nm, a number of them joined to form larger aggregates.

In Figure VIII.4a the isotherm of a sample obtained by treating non impregnated gibbsite through: (i) a drying at 80°C for 3 h; (ii) followed by a thermal treatment under hydrogen from 25°C to 800°C 70°C/min; and (iii) finally in isotherm for 5 min at 800°C under nitrogen, is reported (AlH2). The nitrogen adsorption–desorption isotherm of this sample is of type IV of BET classification and the BJH pore size distribution, reported in Figure VIII.4c results multimodal. In the same figure (Figure VIII.4b), for comparison, the nitrogen adsorption–desorption isotherm of AlN2 is also reported. Pore distribution evaluated by the BJH method is monomodal with a relative maximum at about 4.0 nm (Figure VIII.4d), indicating that the pretreatment phase is fundamental in the controlling the final Al_2O_3 pore size distribution, and crucial for the GCMNPs final size.
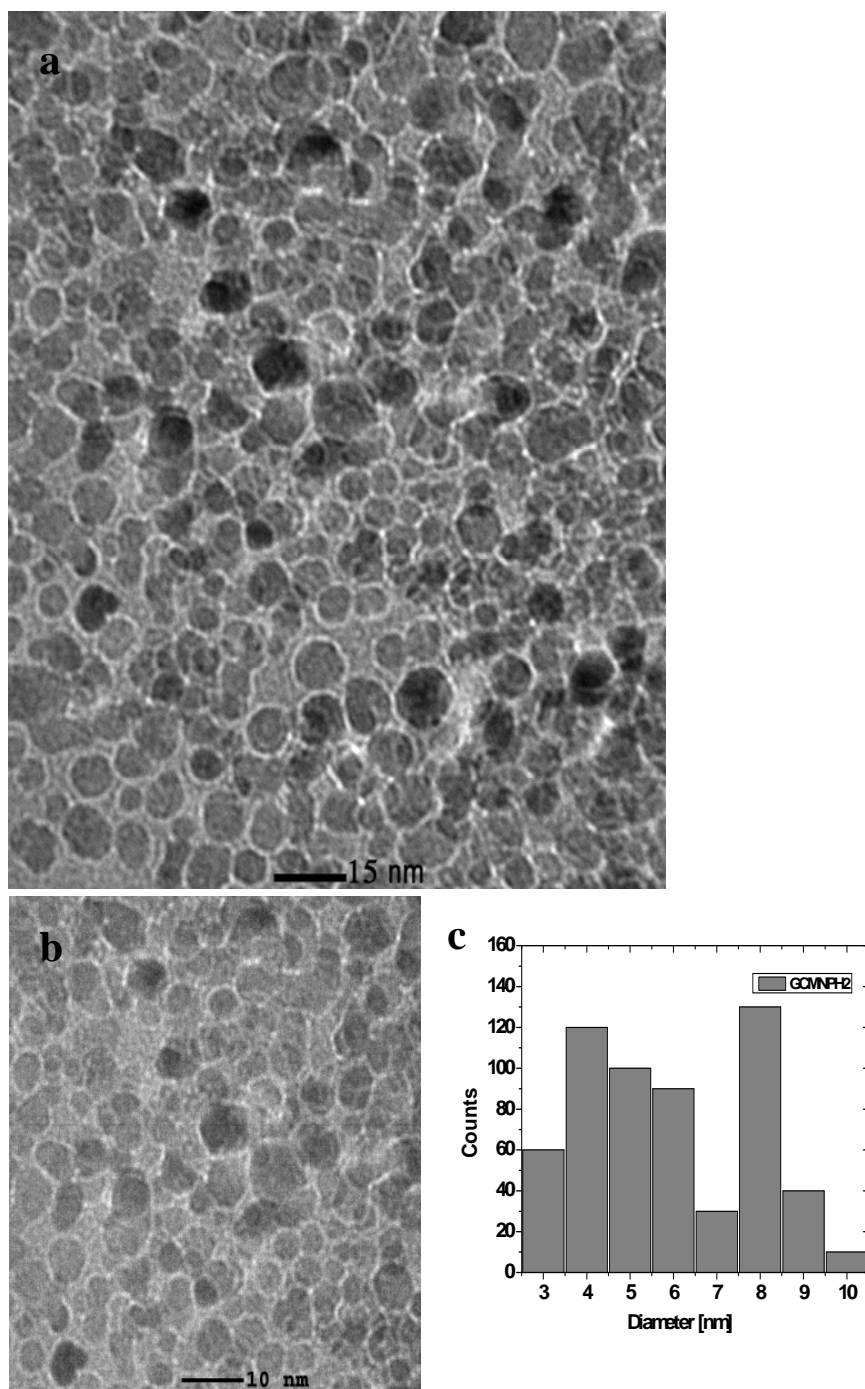
Figure VIII.1 *TEM images (a, b) and nanoparticles size distribution histograms (c), of GCMNPH2*
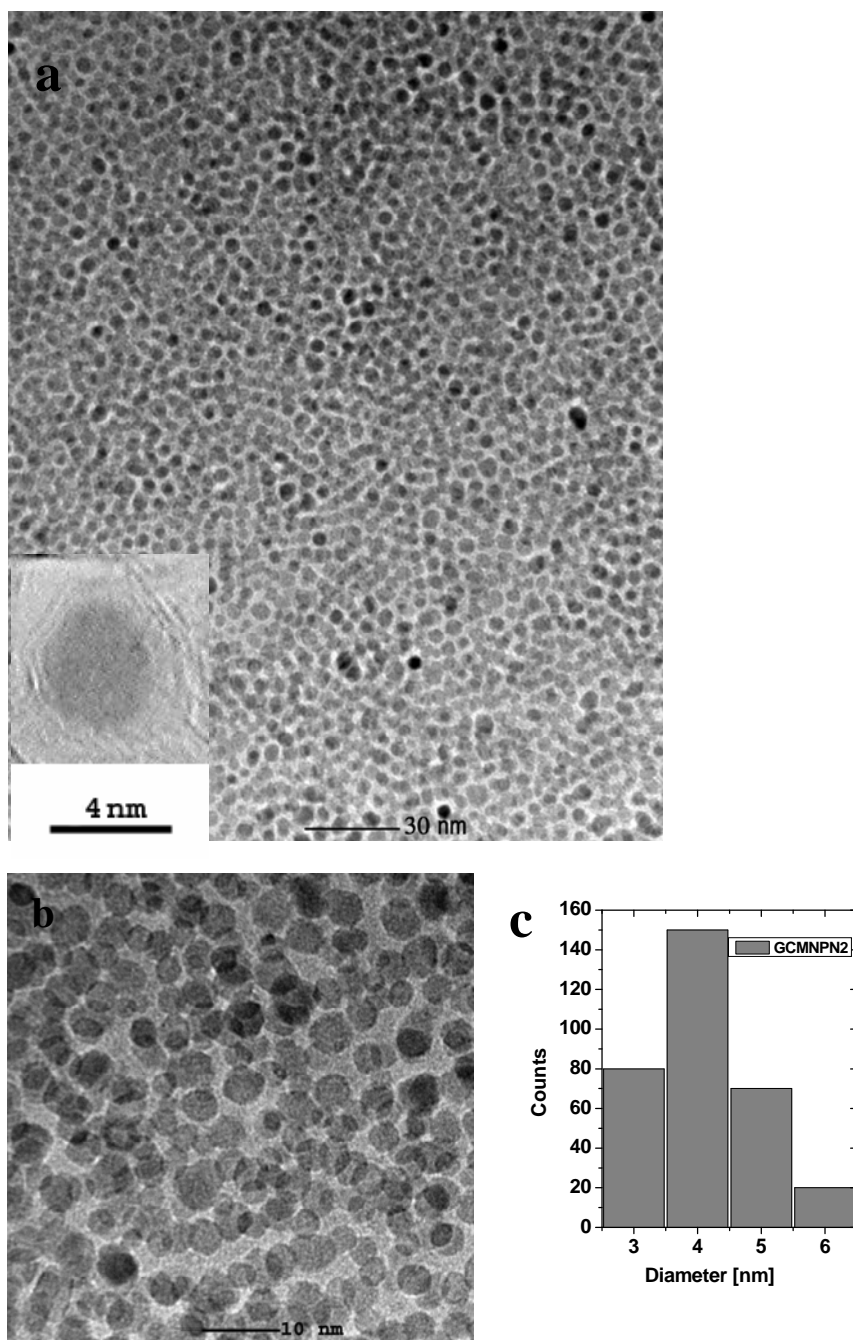
Figure VIII.2 *TEM images (a, b) and nanoparticles size distribution histograms (c), of GCMNPN2. The inserts in the figure show a nanoparticle covered by 1-2 layers graphene*
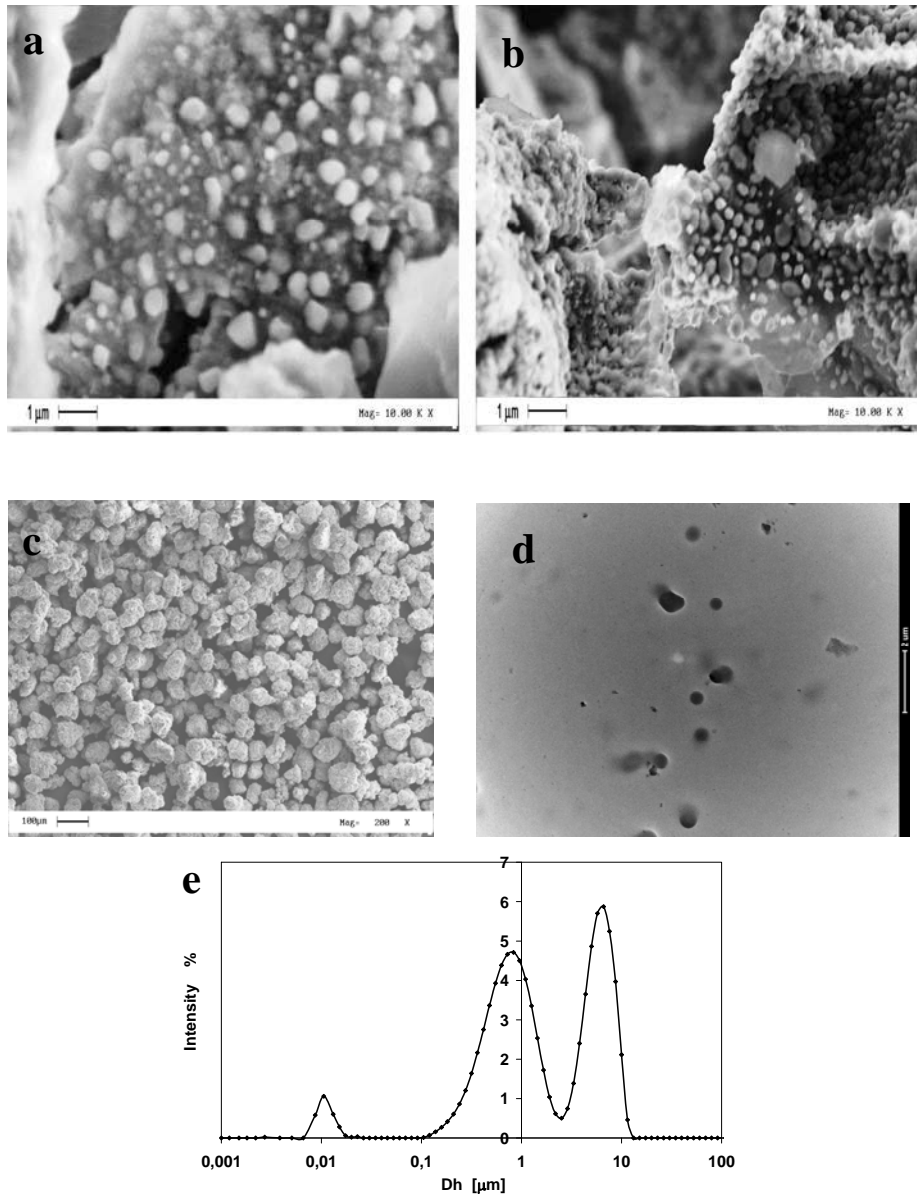
Figure VIII.3 *GCMNPH2 SEM image (a). GCMNPN2 SEM image (b). SEM image (c), low resolution TEM image (for the measurement a drop of the superrnatant solution of the powder in ethanol was casted on a TEM grid) (d) and PSD as determined by DLS technique (e), of AlN2*
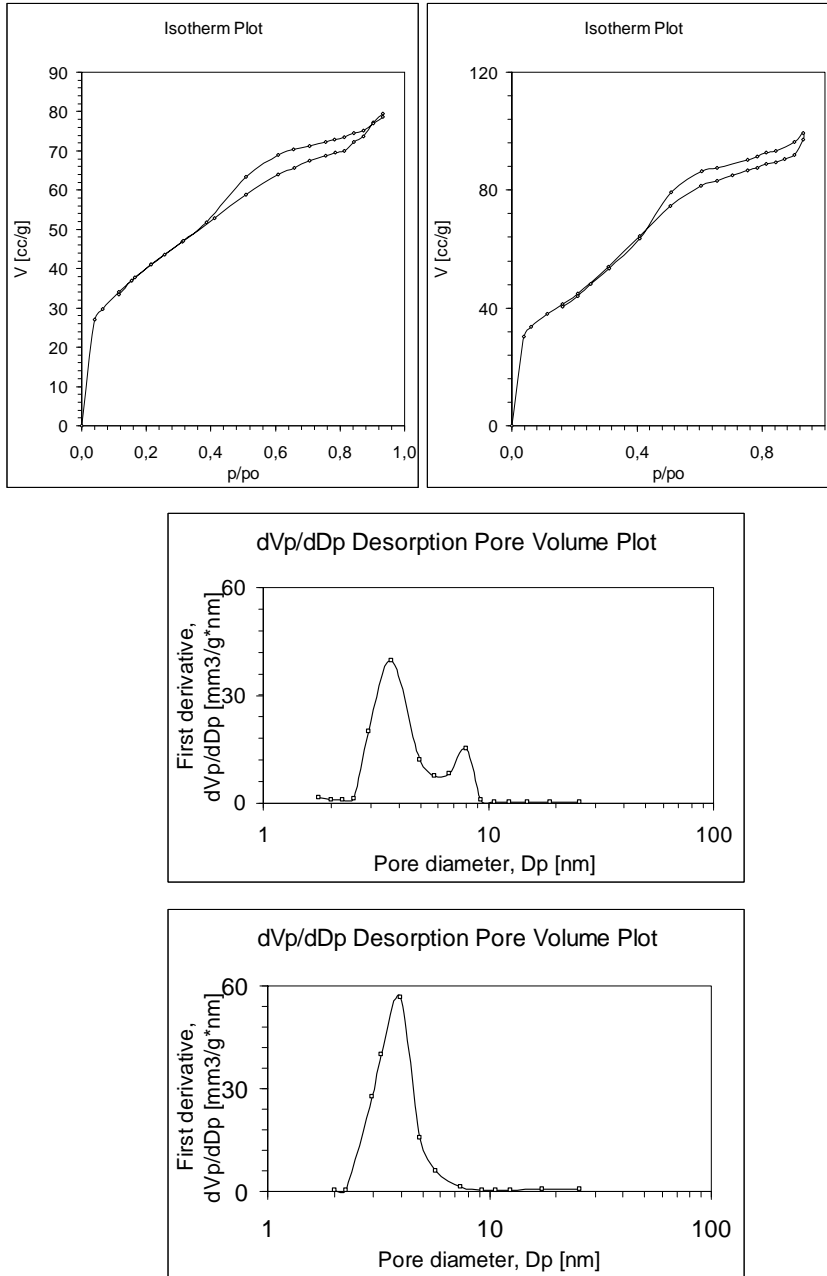
Figure VIII.4 *N₂ adsorption-desorption isotherm (a) and BJH pore size distribution (c) of AlH2. N₂ adsorption-desorption isotherm (b) and BJH pore size distribution (d) of AlN2*

In Figure VIII.5 a and b the x-ray diffraction pattern of GCMNPs are reported. Peaks at 44.87, 65.32 and 82.75 2ϑ typical of a crystalline body-centered-cubic Co/Fe alloy, are present, while it is worth to notice the absence of the (002) diffraction peak due to the stacking of AB graphite.

Finally, in Figure VIII.6 a and b the Raman spectrum of GCMNPs, are reported. In particular, in the spectrum the most prominent features "Lu et al (2007)" of sp^2 carbon materials, the so-called G band appearing at 1582 cm^{-1} and the G' or 2D band at about 2700 cm^{-1}, using 514 nm excitation wavelength, are collected. A broad 2D band (FWHM= 75cm^{-1}) and a pronounced D band, as expected for curved graphene layers "Lu et al (2007)", can be observed.
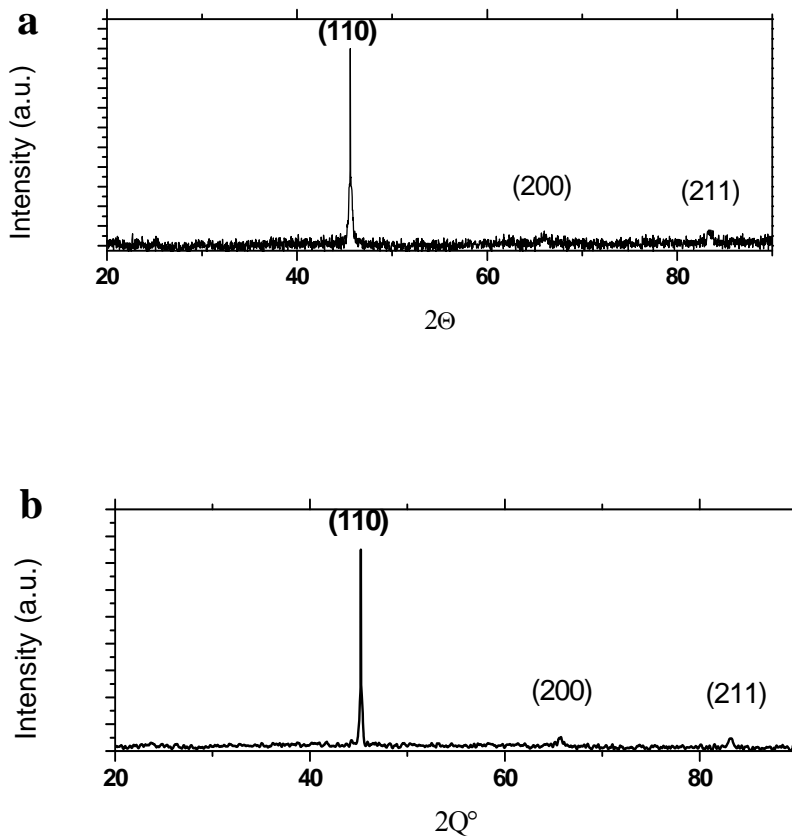
Figure VIII.5 *X.ray diffraction patterns of GCMNPH2 (a) and GCMNPN2 (b)*

a

b
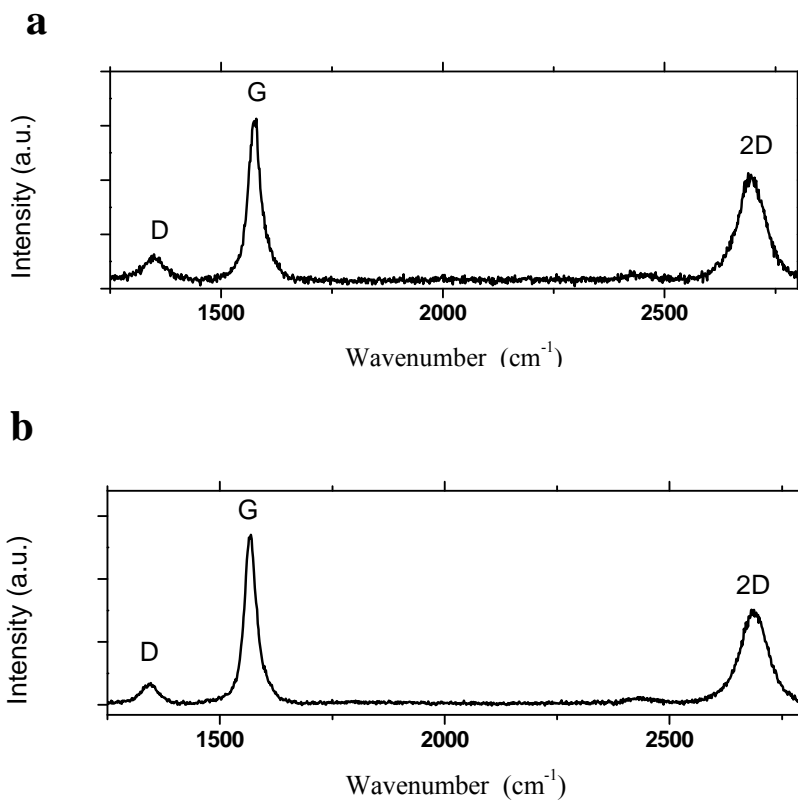
Figure VIII.6 *Raman Spectra of GCMNPH2 (a) and GCMNPN2 (b)*

Finally, the results related to the evaluation of the methane conversion, during the tests, as obtained by the evolution of the exhaust gas composition, are reported in the following.

The concentrations of CH_4, C_2H_2, C_2H_4 and H_2, in the effluent stream during the GCMNPs reactions, have been monitored by the on-line analyzers.

The relevant profiles are shown in Figure VIII.7.
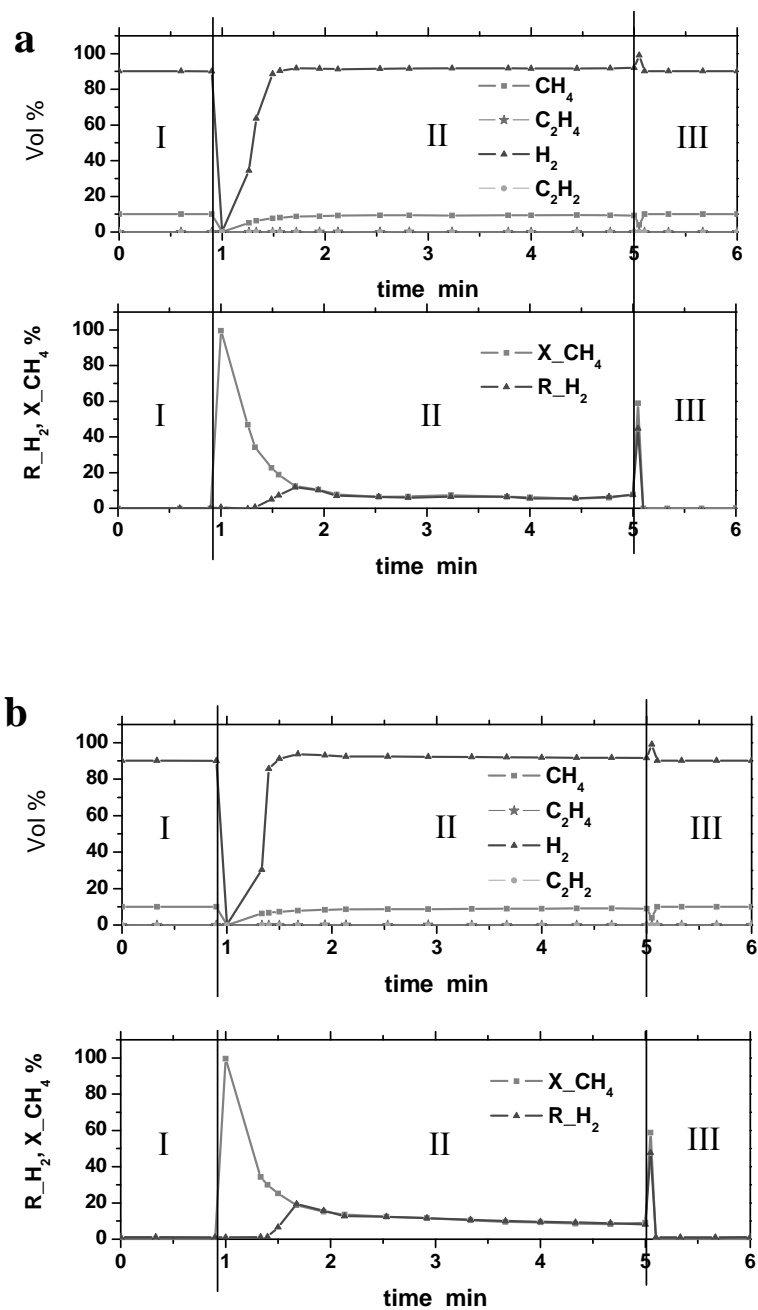
Figure VIII.7 *On line analysis and CH₄ conversion and H₂ yield during the tests: for GCMNPH2 (a) and GCMNPN2 (b) syntheses.*

We can distinguish three temporal phases:

Pre-reaction phase (I): the reaction gas is fed to the analyzers. The concentration values of C_2H_4 and C_2H_2 are close to zero, while the initial methane and hydrogen concentrations are 10% v/v and 90% v/v, respectively.

Reaction phase (II): the gases are fed to the reactor, reaching the analyzers after passing through the catalyst bed. After the time necessary to traverse the reactor and accounting for the delay time of the analyzers, methane and hydrogen concentrations stabilize reaching a plateau. No significant C_2H_4 and C_2H_2 concentrations are detected during the entire running time at the chosen temperature.

Post-reaction phase (III): the gases are sent directly back to the analyzers (by passing the reactor). The concentrations of the four gases are the same as those in the pre-reaction phase.

The methane conversion and hydrogen yield were calculated by assuming the methane conversion to carbon and hydrogen as the main reaction:

$CH_4 \rightarrow C + 2\, H_2$
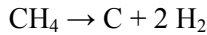
Considering this reaction and the initial feed composition, the expansion volume factor (εCH_4) can be calculated and the methane conversion and hydrogen yield can be expressed as:

$$X_{CH4} = \frac{1 - \dfrac{C_{CH4}}{C^0_{CH4}}}{1 + \dfrac{\varepsilon_{CH4} \times C_{CH4}}{C^0_{CH4}}}$$

(VIII.3)

$$R_{H2} = \frac{(1 + \varepsilon_{CH4} X_{CH4}) \times C_{H2}}{2C^0_{CH4}}$$

(VIII.4)

where C is the current concentration and C^0 the initial concentration of a single component.

The agreement between the CH_4 conversion (x_CH_4) and the H_2 yield (R_H_2) curves (see Figure VIII.7a and VIII.7b, for the profiles of CH_4 conversion and H_2 yield), visible after the transient, validates the previous hypothesis, indicating that the catalyst was selective to give carbon and hydrogen "Maaz et al. (2010)".

No carbon deposition was detected during a blank test running time, obtained by recording the evolution of the reactor's exhaust gas composition in the absence of the metal catalysts "Maaz et al. (2010)". The evolution of the concentration profiles of the exhaust gases in presence of non gibbsite impregnated, indicates an absence of homogeneous methane decomposition, while the C_2H_4, C_2H_2 were close to zero. The methane conversion reached during the GCMNPH2 results slightly lower 3.8 v/v% than that reached for GCMNPN2 4.2 v/v%, due to the different nanoparticles size distribution.

VIII.3.2 Magnetic properties

In Figures VIII.8-VIII.10 the dc magnetization M as function of temperature T in an external magnetic field of 10 KOe, are reported for GCMNPH2 (Figure VIII.8a) and GCMNPN2 (Figure VIII.8b).
The M(T) measurements were obtained by first cooling the sample in a zero magnetic field down to 4.2 K, then a dc field of 10 kOe was applied and the so-called zero field cooled (ZFC) dc magnetization was recorded as a function of the temperature up to about 350 K. The sample was then cooled down while keeping the external field constant and so the field cooled (FC) magnetizations at a 10 KOe external field were measured, as a function of the temperature. Although in both samples a blocking temperature can be identified from the M(T) measurements, two different behaviours characterize the two samples. In particular, for GCMNPH2 the ZFC curve shows an intense and narrower cusp at about 300 K and a broader one around 165 K, corresponding to two different blocking temperatures, below which the magnetic moments are experimentally seen as blocked in fixed directions. In fact, the blocking of superparamagnetic particles is related to their magnetic anisotropy. In the simple case of uniaxial anisotropy two preferred orientation can be expected for the particle magnetic moment. Both orientations are separated by an energy barrier U=KV, where K is an effective anisotropy constant and V is the particle volume. The relaxation time, needed to reverse the magnetic moment of the particle, follows the Arrhenius law τ=τ0exp(U/KBT). Larger particles will have higher energy barrier and consequently relaxation times will be longer and their magnetic moments will become blocked at higher temperature. The existence of the two maxima in the ZFC curve is indicative of the existence of two different distribution of particle size. This is in agreement with TEM results, where two different ranges of particles sizes for the nanocrystals were determined.
On the other hand, the M(T) measured on the sample GCMNPN2 shows (see Figure VIII.8b) a quite different behaviour respect to the GCMNPH2. More precisely, at a temperature around 126 K for the ZFC curve (and 132 K for the FC one) an abrupt change in the magnetisation of the sample appears, combined at lower temperatures with a linear, noisy though, temperature dependence of the magnetisation, as better visible in the insert of Figure

VIII.8b. This behaviour can be interpreted in terms of uniform excitations in the magnetic dynamics of the nanoparticle. Infact, below TB, the superparamagnetic relaxation is considered negligible, although the direction of the magnetization can still flip between the direction of the easy axis of the nanoparticles and the antiparallel one. The magnetic dynamics at these temperatures can be described in terms of excitations of spin waves, with different modes. More precisely, in the uniform mode all the atomic spins precess in unison, whereas in correspondence of higher wave vectors, the atomic spins precess such that the angle between adjacent spins increases with the wave vector.

In nanoparticles at low temperatures the magnetic dynamics is a combination of excitations of the uniform mode and of the transitions between excited states with different precession angles. These are called "collective magnetic excitations" "Mørup, et al. (1976a), Mørup et al. (1976b), Mørup (1983)", and the presence of a predominant uniform mode in the magnetic dynamics can explain the linear temperature dependence of the magnetisation in nanoparticles at low temperatures, as that reported in Figure VIII.8b " Mørup et al. (2010)". In this scenario, although further analysis are necessary, it can be speculated that also the large jumps in the curve of Figure VIII.8b below TB can be explained in the same framework, in terms of fluctuations between antiparallel collective magnetic states.

In Figure VIII.9a-b the hysteresis loops of the two samples at T= 5 K (Figure VIII.9a for the GCMNPH2 and Figure VIII.9b for the GCMNPN2) and T= 300 K (Figure VIII.10a for the GCMNPH2 and Figure VIII.10b for the GCMNPN2) is presented. The insert of all the figures shows a magnified region around the origin to make the coercivity more visible at the two temperatures for both the samples. A saturation magnetization of 230 e.m.u./g for the sample GCMNPN2, the highest Ms obtained for nanocrystal, can be measured. For GCMNPH2, the measured Ms was 185 e.m.u./g, the lower Ms due to the broader distribution, and the larger size of the nanoparticles. The presented hysteresis loops, are coherent with a superparamagnetic behaviour for both samples, with a coercive field of about 170 Oe at T=300 K (and 200 Oe at T=5K) for the sample GCMNPH2, and of about 70 Oe at T=300 K (and 85 Oe at T=5 K) for the sample GCMNPN2.

a

b
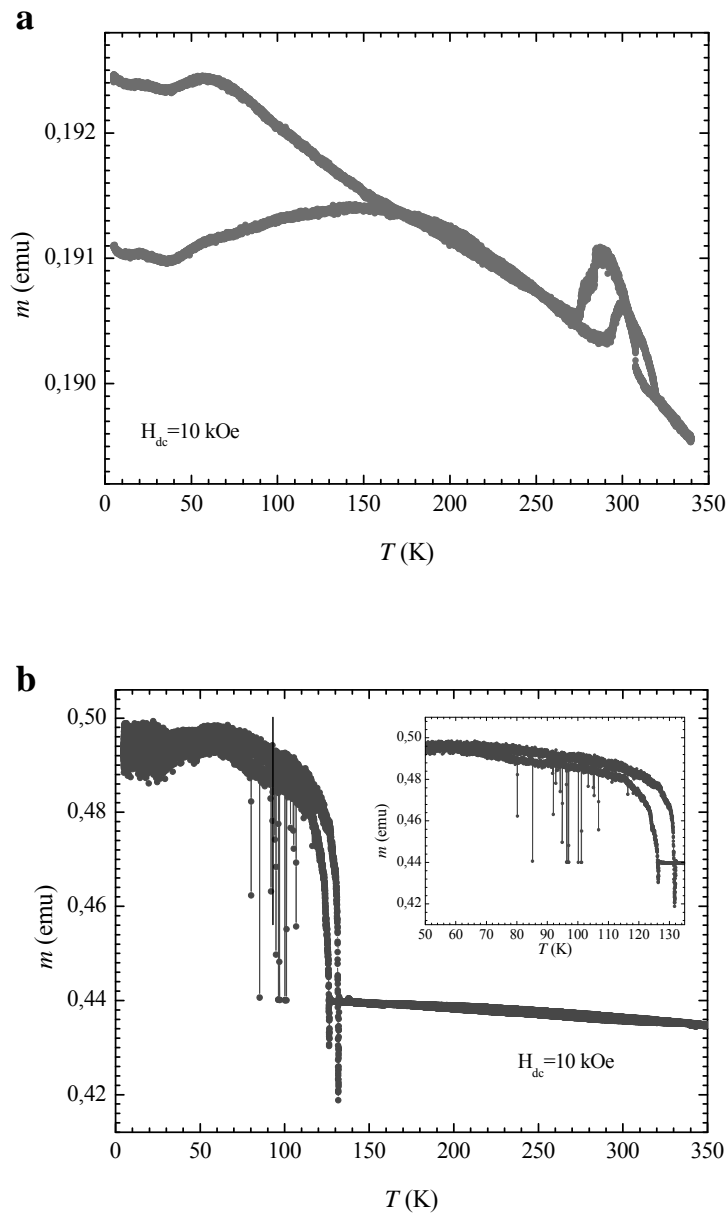
Figure VIII.8 (a,b) *ZFC/FC measurements of the magnetic moment as function of the temperature, in presence of a Hdc=10 kOe, for the sample GCMNPH2 (a) and for the sample GCMNPN2 (b). Insert of Figure VIII.8b is the magnification of the curve in the temperature range [50 ÷ 135] K*

a

b
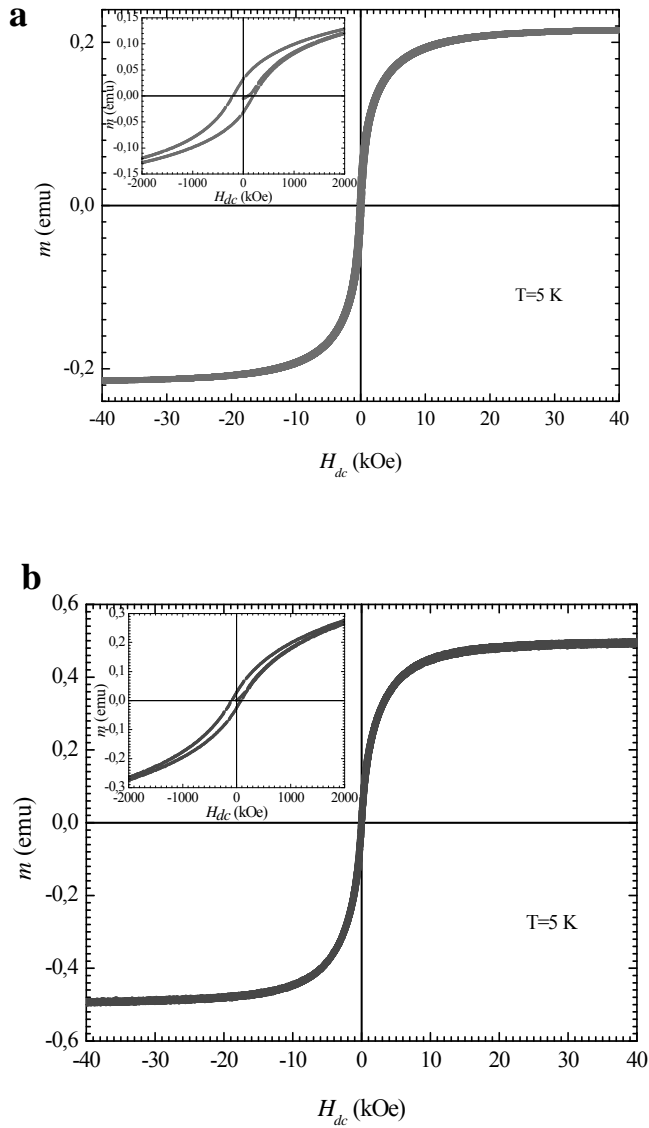
Figure VIII.9 (a,b) *Magnetic hysteresis loop at T=5 K, for the sample GCMNPH2 (a) and for the sample GCMNPN2 (b). Inserts of Figures VIII.9a-b are the magnification of the relative hysteresis loop in the low field region, to show the width of the hysteresis and the value of the coercive fields.*
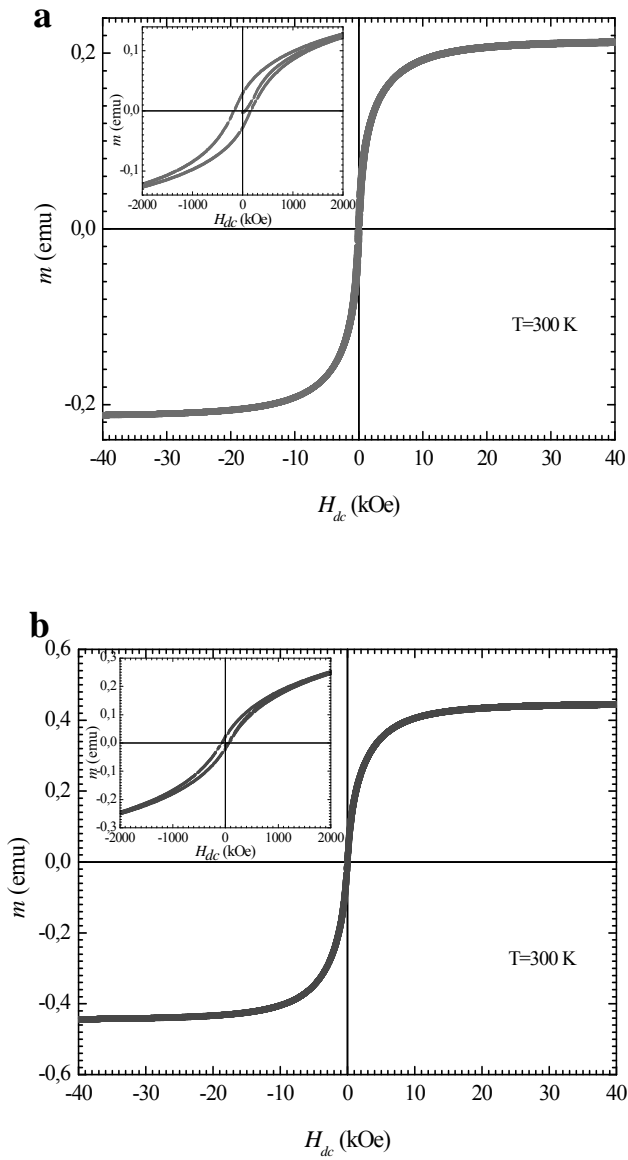
Figure VIII.10 (a,b) *Magnetic hysteresis loop at T=300 K, for the sample GCMNPH2 (a) and for the sample GCMNPN2 (b). Inserts of Figures 10a-b are the magnification of the relative hysteresis loop in the low field region, to show the width of the hysteresis and the value of the coercive fields*

VIII.4 Conclusions

Core-shell few layer graphene-coated magnetic nanoparticles (GCMNP) were synthesized by catalytic chemical vapor deposition (CCVD) of methane at atmospheric pressure. Stable core-shell graphene-coated GCMNPs have been prepared.

The pretreatment conditions determine the final alumina pore size distribution and, in the experimental conditions explored, the GCMNPs diameter. The pretreatment was performed either in H_2 or in N_2. The nanoparticles magnetic properties have been found strongly dependent by their size. A Ms value of 230 e.m.u./g, was found, for our monodispersed 4.1 nm diameter body-centered-cubic-FeCo nanoparticles.

Chapter IX
Experimental VI

Few layer graphene oxide as additive for oil lubricant

IX.1 Introduction

Friction and wear are the two major causes for energy and material losses in mechanical processes. Lubrication is a principal focus to improve energy efficiency and mechanical durability. For tribology applications, nanoparticles as additives in base oil have been investigated widespreadly. These studies refer to synthesis and preparation of nanoscale particles, and their tribological properties and mechanisms. It has been found that when the nanoparticles were added to base oil, the extreme-pressure property and load-carrying capacity were improved and friction coefficient was decreased. In the past few years, nested spherical supramolecules of metal dichalcogenide have been synthesized by reaction of metal oxide nanoparticles with H_2S at elevated temperatures. Because of their nested fullerene-like structure, these species are known as inorganic fullerene-like (IF) nanoparticles. The IF nanoparticles exhibited improved tribological behaviour compared to the micro-scale platelets for their robustness and flexibility "Yadgarov et al. (2013), Rosentsveig (2009)".
Recently, due to high load-bearing capacity, low surface energy, high chemical stability, weak intermolecular, and strong intramolecular bonding, nanocarbon materials, such as graphite "Wintterlin (2008)" and some graphite derivatives "Ramanathan et al. (2008), Bryant et al. (1964), Bernan et al. (2013)" as well as other lubricant materials "Fusaro et al. (1979);Tian et al. (1997), Hilton et al. (1992)" together, have received a great attention by tribology researchers. These materials are characterized by weak interatomic interactions between their layers (Van der Waals forces) and low-strength shearing. In recent years graphene platelets due to their unique structure and remarkable properties have been the focus of interest. However, few studies on the tribological applications of graphene platelets as lubricant additives "Huang et al. (2006), Lin et al. (2011), Zhang et al. (2011)" have been reported so far. On the other hand, the initial results are

very interesting, so it is expected that a large number of documents will be published on this subject in the next future.

Huang et al. "Huang et al. (2006)", investigated the tribological properties of graphite nanosheets (10-20 nm thick) prepared by stirring ball milling of natural flake graphite as an oil additive. They found that the frictional behaviour and anti-wear ability of the lubricating oil were improved when graphite nanosheets and dispersant were added to the paraffin oil at the optimal concentration.

Lin et al. "Lin et al. (2011)" suggested that functionalizing the graphene platelets with a proper modifier is an effective way to prevent the dispersion of the additive. They demonstrate that stearic acid and oleic acids are the most suitable modifiers for their platelets (10-15 nm thick). Contemporaneously "Zhang et al. (2011)", graphene nanosheet obtained by graphite exfoliation, modified with oleic acid and further reduced in hydrazine hydrate were investigated using a four-ball tribometer.

In this chapter, the preparation of graphene oxide (GO) nanosheets (5-6 nm thick) by a very fast modified Hummer method was reported. Due to the preparation method the nanosheets are characterized by a low level of order, while the surfaces result in rich of –OH and –COOH groups giving them a polar behaviour. We chose, at the best of our knowledge for the first time, to use as produced GO, avoiding further chemical reactions and to disperse through a methodology well known to the lubricant industry by the use of a dispersant, that with its polar head can enwrap one nanoparticle to repel another and therefore form a uniform dispersion. On the other hand, amorphous structure are much easier exfoliated than the perfect structure "Lahouij et al. (2012)", while the formation of a tribofilm on the worn steel surface is directly related to the particles exfoliation.

The tribological behaviour of a very low amount of GO mixed with a dispersant in Group I base mineral SN150 was investigated under very wide spectrum of conditions, i.e. from boundary and mixed lubrication to the elastohydrodynamic (EHL) regimes. The nanosheets were widely characterized. To explore the performances of the nanosheets in the lubricating fluid, a rotational tribometer with a ball on disc setup has been employed.

Raman analysis on the steel ball worn surfaces was performed to investigate the presence of graphitic material on the mating surfaces after tribological tests, in order to verify the formation of a protective film on the rubbing surfaces due to the additive.

IX.2 Experimental

IX.2.1 Nanosheets preparation and characterization

IX.2.1.1 Materials

Graphene Oxide (GO) nanosheets were prepared by a modified Hummer method "Hummer and Offeman (1958)". The oxidation of graphite particles were obtained from Lonza "Hummer and Offeman (1958), The history of Lonza's graphite powders. Industrial Lubrication and Tribolog." to graphitic oxide accomplished with a water-free mixture of concentrated sulfuric acid, sodium nitrate and potassium permanganate. The entire process requires less than two hours for completion at temperatures below 45 °C. With the aid of further sonication step, the oxidized graphite layers were exfoliated from each other. Then 30% H_2O_2 was added to the suspension to eliminate the excess MnO_4^-. The desired products were rinsed with deionized water. The remaining salt impurities were eliminated with resinous anion and cation exchangers. The dry form of graphitic oxide was obtained by centrifugation followed by dehydration at 40 °C.

To provide dispersion stability of the additive a polyisobutyl succinic acid-polyamine ester was sonicated with the GO nanosheet (0,01 w.t.% in base oil), the weight ratio GO/dispersant was 0.35. The dispersant attaches itself to the solid particles with its polar head, and has a very long hydrocarbon tail that keeps it suspended in oil. For the dispersion, a sonication (Hielscher UP 400S) of 30 min in 25 ml mineral oil, followed by a mixing with a Silverson L5M homogenizer for 30 min, were employed. The resulting sample is named GSN150 in the following.

IX.2.1.2 Characterization techniques

Scanning electron microscopy (SEM) pictures were obtained with a LEO 1525 microscope. The samples, without any pre-treatment, were covered with a 250 Å thick gold film using a sputter coater (Agar 108 A). Raman spectra were obtained at room temperature with a microRaman spectrometer Renishaw inVia with 514 nm excitation wavelength (laser power 30 mW) in the range 100-3000 cm^{-1}. Optical images were collected with a Leica DMLM optical microscope microscopy connected on line with the Raman instruments. XRD measurements were performed with a Bruker D8 X-ray diffractometer using CuKα radiation. Transmission electron microscopy (TEM) micrographs were obtained with a JEOL JEM 2010 electron microscope operating at 200 keV. Thermogravimetric analysis (TG-DTG) at 10 K/min heating rate in flowing air was performed with a SDTQ 500 Analyzer (TA Instruments).

IX.2.2 Tribological tests

IX.2.2.1 Test description

In this study, the investigated tribopair was composed by an upper rotating disc and a lower ball specimen completely flooded in a temperature-controlled lubricant bath in line with the features of the used tribometer, Wazau TRM100. The upper element of the tribopair was a X155CrVMo12-1 steel disc, 60 HRC, roughness Ra = 0.50 μm and 105 mm diameter, the lower one was a X45Cr13 steel ball, 52-54 HRC, 8 mm diameter.

The normal force to the ball-disc contact was delivered by a lever system and could be varied in the range of 0-100 N; its value was measured through a load cell placed under the specimen holder. The following average hertzian pressures were used at the ball/disc interface with normal load given in brackets: 1.17 GPa (30 N), 1.47 GPa (60 N), 1.68 GPa (90 N). The tests were performed for three different temperatures, 25, 50 and 80 °C, and the lubricant average temperature has been kept constant through a NiCr-Ni-thermocouple in the oil reservoir and an electric resistance driven by a digital controller. This control system allows a control range from room temperature up to 100 °C.

Speed-sweep tests at constant load on broad sliding speed range have been performed to cover different lubrication regimes with the aim of minimizing the modification of the tribopair steel surfaces. For this reason, the time extension of the each test was limited to 16 minutes. The disc speed rose up to 2.20 m/s in the first 4 minutes and dropped to zero in the following 4 minutes. This speed pattern was repeated twice. The current design of this experiment allowed obtaining a complete Stribeck frictional graph.

The tests were performed for three different temperatures, i.e. 25, 50 and 80 °C. All the samples have been stirred before each test for 20 minutes by means of a Turrax T 25 Digital homogenizer with adjustable speed. No chemical dispersant agents were used in order to explore the benefits coming from the pure addition of nanoparticles.

Tests were also carried out to analyse the influence of GO addition to the base oil on wear behaviour of the steel ball/disc tribopair through steady state rubbing tests, see section IX.3.2.2. For these tests, constant values for average hertzian pressure, temperature and speed were chosen.

IX.3. Results and Discussion

IX.3.1 Graphite and GO characterization

Graphite chips and GO nanosheets are shown in Figures IX.1a, IX.1b respectively. The images at higher magnification (inserts in Figure IX.1), evidence the loss of the chips structure of original graphite to GO transparent and thin flakes.

The TEM images in Figure IX.2 reveal the thickness of the graphene oxide nanosheets that is in the range 5-6 nm. The high resolution transmission electron image evidences the not so high level of order of the graphene nanosheets, quite permitting to measure the number of layers.

X-ray diffraction spectra of original graphite and GO are shown in Figure IX.3, in the 2θ range 20°–80°. It is clearly evident the lost of the original graphite structure for GO.

In Figure IX.4 the TG-DTG data (from 30 to 800°C at 10°C/min) of the tests performed with graphite and GO, are reported. The oxidation of the GO occurs as a one-step loss, centred at 605°C, well before the graphite oxidation temperature, likely due to the loss of the graphite original order. The thermal conversion of the dispersant in air flow occurred in two main weight loss steps (Figure IX.5), due to its decomposition (as clearly indicated by the corresponding total ion current (TIC), in particular in the figure the mass fragments peaks: m/z =58, 72, 83 coming from the NH containing group are shown), and the formation of CO_2 (m/z = 44).

The thermal oxidation of SN150, with the onset point at about 205°C, is shown in Figure IX.6. It is worthwhile that the presence of the dispersant and GO, also due to the low amount, has a no strong effect on the thermal behaviour of the base oil. The insert in the figure permits to observe the GO oxidation around 600°C.

IX.3.2 Tribological characterization: friction coefficient

The measured data are presented according to the Stribeck curves representation, i.e. friction coefficient vs. sliding speed. Results obtained for the base oil sample and the sample formulated with GO nanosheets for different level of temperature and average hertzian contact pressure are shown and discussed in this section. The main properties of SN150 base oil were: kinematic viscosity, 29.7 cSt at 40 °C, 5.1 cSt at 100 °C; density at 20ºC, 0.87 kg/dm^3.

The set of graphs in Figure IX.7 introduces the Stribeck curves exhibited in the sliding tests by the SN 150 oil with 0.01 wt.% GO nanosheets at different levels of average hertzian contact pressure and lubricant temperature, along with the error bars denoting the standard deviation around the rolling mean.

117
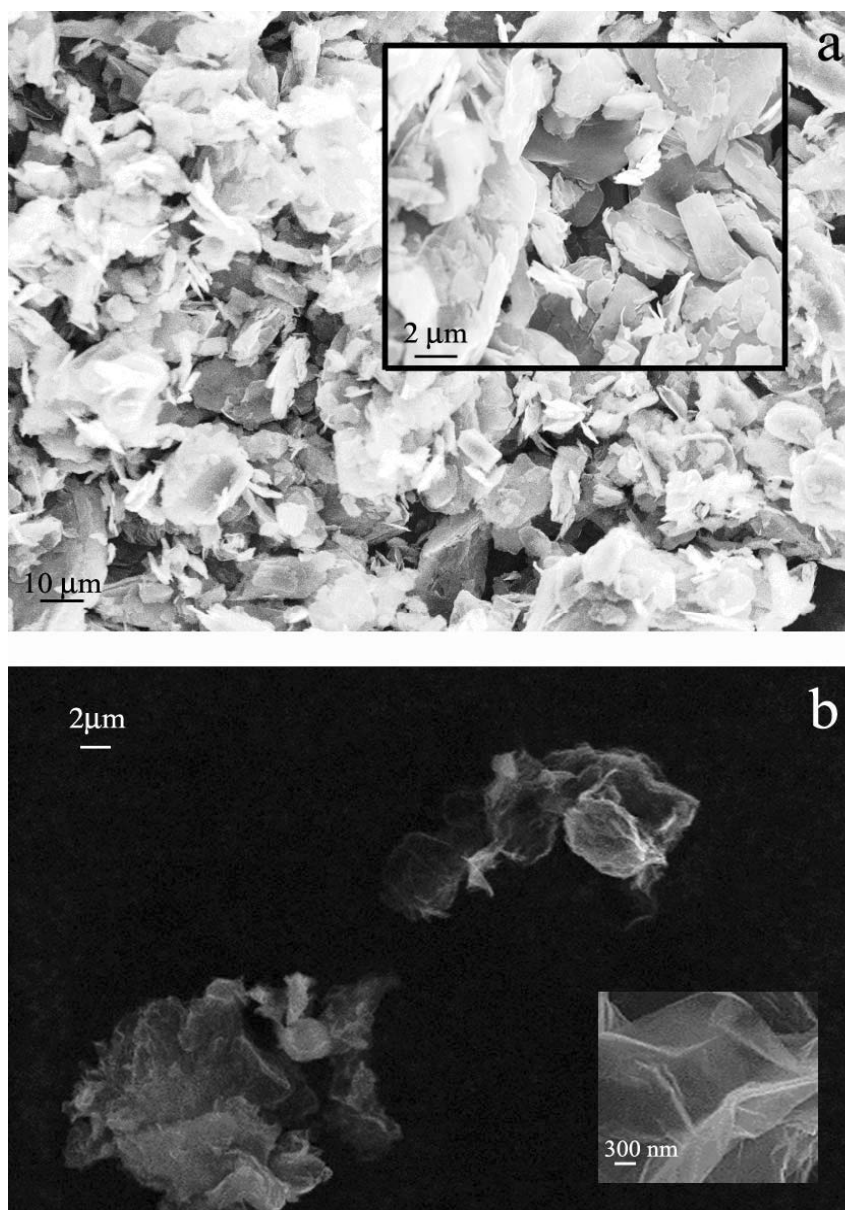
Figure IX.1. *SEM images of: graphite (a), GO (b)*
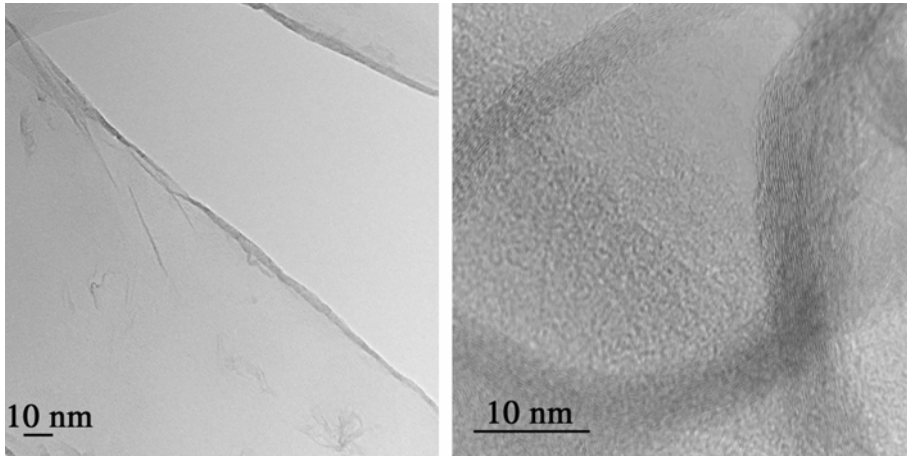
Figure IX.2 *TEM images of GO at different magnification*
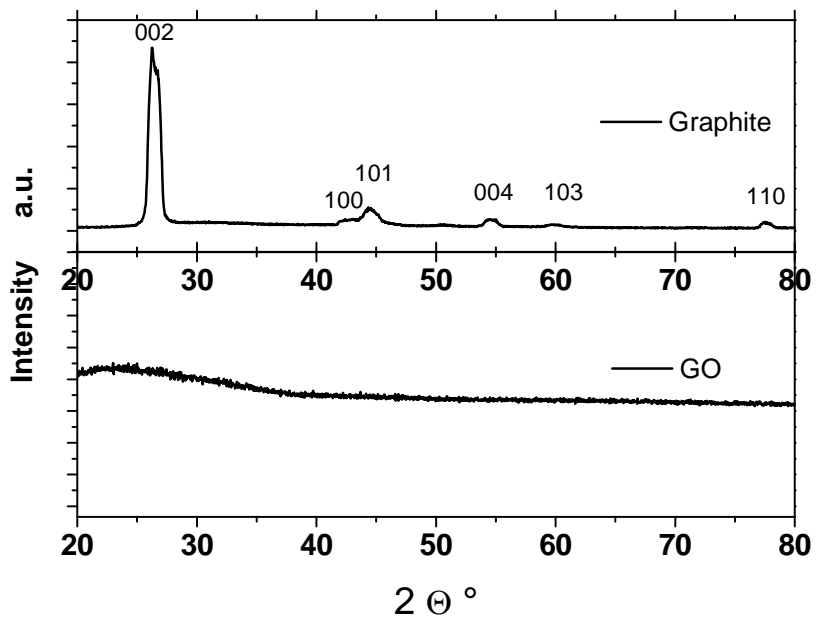
Figure IX.3 *X-ray diffraction patterns of graphite and GO*
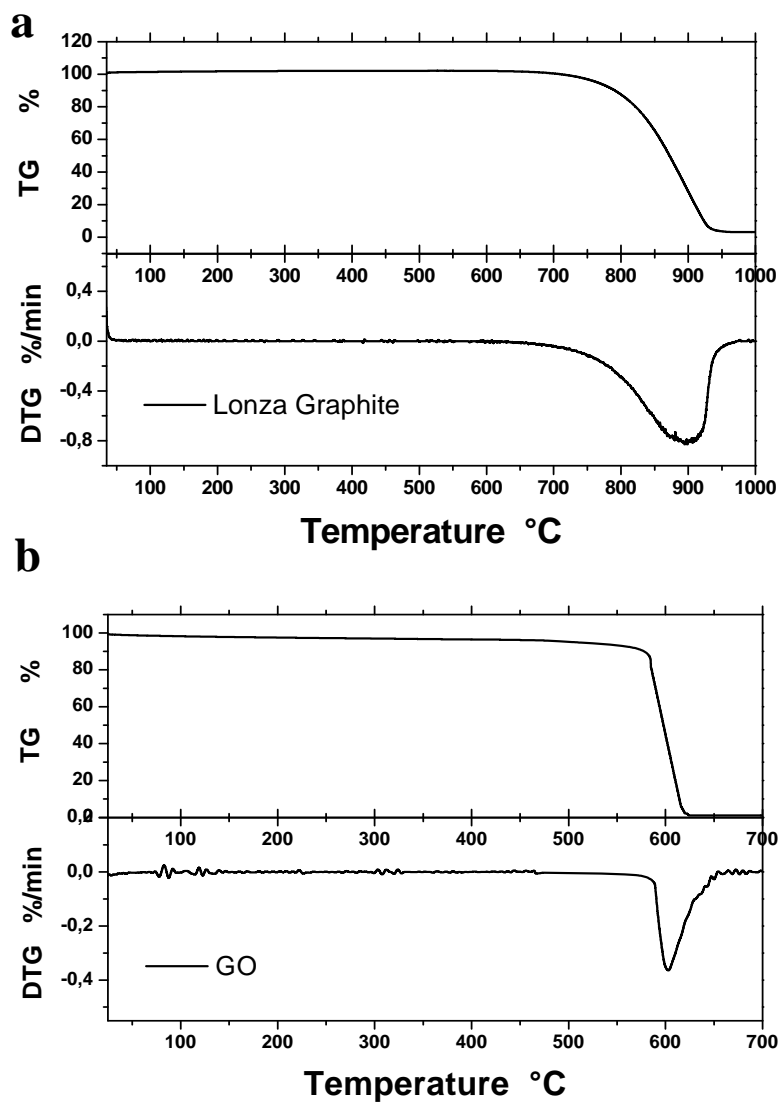
Figure IX.4 *TG-DTG analysis of graphite (a) and GO (b)*
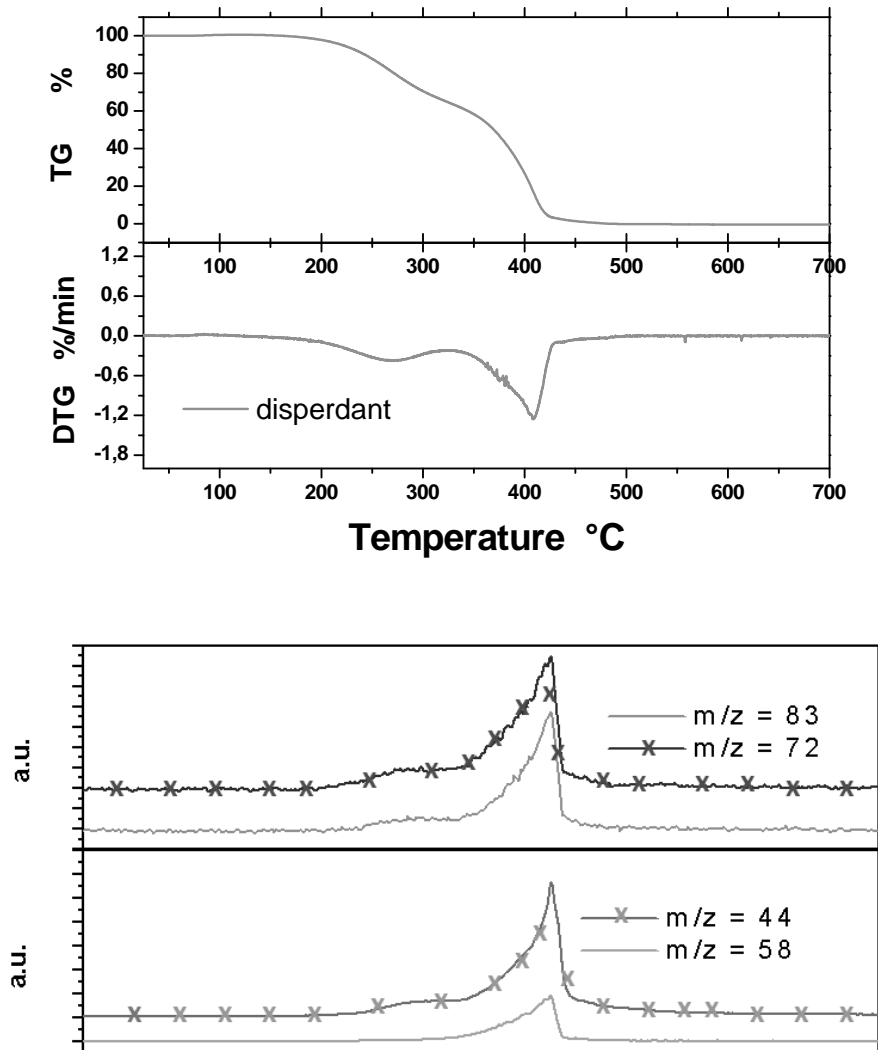
Figure IX.5 *TG-DTG analysis (top) and the MS evaluation (bottom) of the dispersant*
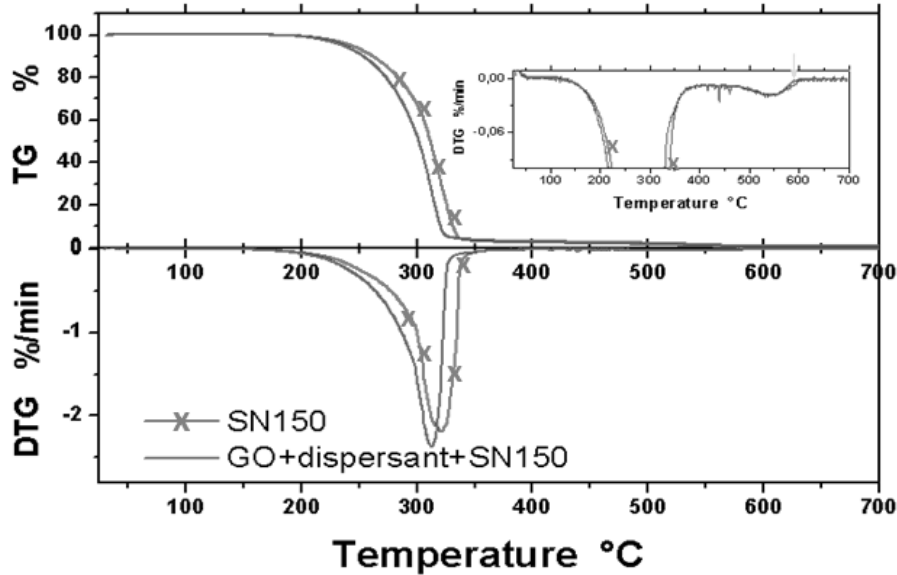
Figure IX.6 *TG-DTG analysis of SN150 base oil, and SN150 + dispersant + GO*

Those results show the decrease of the friction coefficient for increasing average hertzian contact pressure for the formulated sample; the same behaviour has been observed for the base oil according to a point-contact studied effect: the shear stress increases less in proportion to the contact pressure; this leads to a slight reduction of friction "Yadgarov, et al. (2013)". As expected, for a given sample, the minimum of the Stribeck curve moves right for increasing temperature due to the lower viscosity. Additionally, for each sample, the CoF increased with the temperature at given level of speed and contact pressure. This observation could be mainly addressed to the effect of the lower lubricant viscosity and the ensuing GO precipitation at higher temperature.

The Stribeck graphs in the Figure IX.7 for average hertzian pressure equal to 1.17 GPa, 1.47 GPa and 1.68 GPa show a shape with a well developed minimum, that is considered the transition from mixed lubrication regime to EHL regime for increasing speed "Kalin et al. (2009), Cho et al. (2006)". This frontier divides the region with concurrent phenomena of solid-to-solid contacts, adhesion and interaction between friction modifier additives and steel surface (mixed lubrication) from the other with predominant viscous stress and elastic deformation of the tribopair surfaces (EHL). For instance, the transition appears in the speed range 0.30-0.40 m/s for the test at 25 °C and 0.50-0.60 m/s at the higher temperature, 80 °C.

These tests confirm that using graphene nanoparticles in lubricants enhances the friction reduction in boundary, mixed and EHL lubrication regimes.

For instance, with contact pressure of 1.17 GPa and temperature in the range 25-80 °C, the average friction coefficient decreased by 20% of the base lubricant value; similar average reduction could be observed for all the combinations of the operating conditions. Even in the heaviest test conditions (high pressure and temperature) and in fully developed EHL regime where the viscous stresses are prevalent, the CoF reduction is greater than 8% (Figure IX.7i).

1-hour sliding tests were also performed to analyse the influence of the progressive wearing of the mating materials on the friction coefficient (Figure IX.8). The average friction coefficients measured during these steady state tests are presented in Tables 1 and 2. According to ISO/IEC Guide 98-3:2008, the average friction coefficients are presented with expanded uncertainty equal to 5 10-3, coverage factor k = 2.

The lubrication regimes in these tables and Figure IX.8 are identified according to the results of the Stribeck curves.
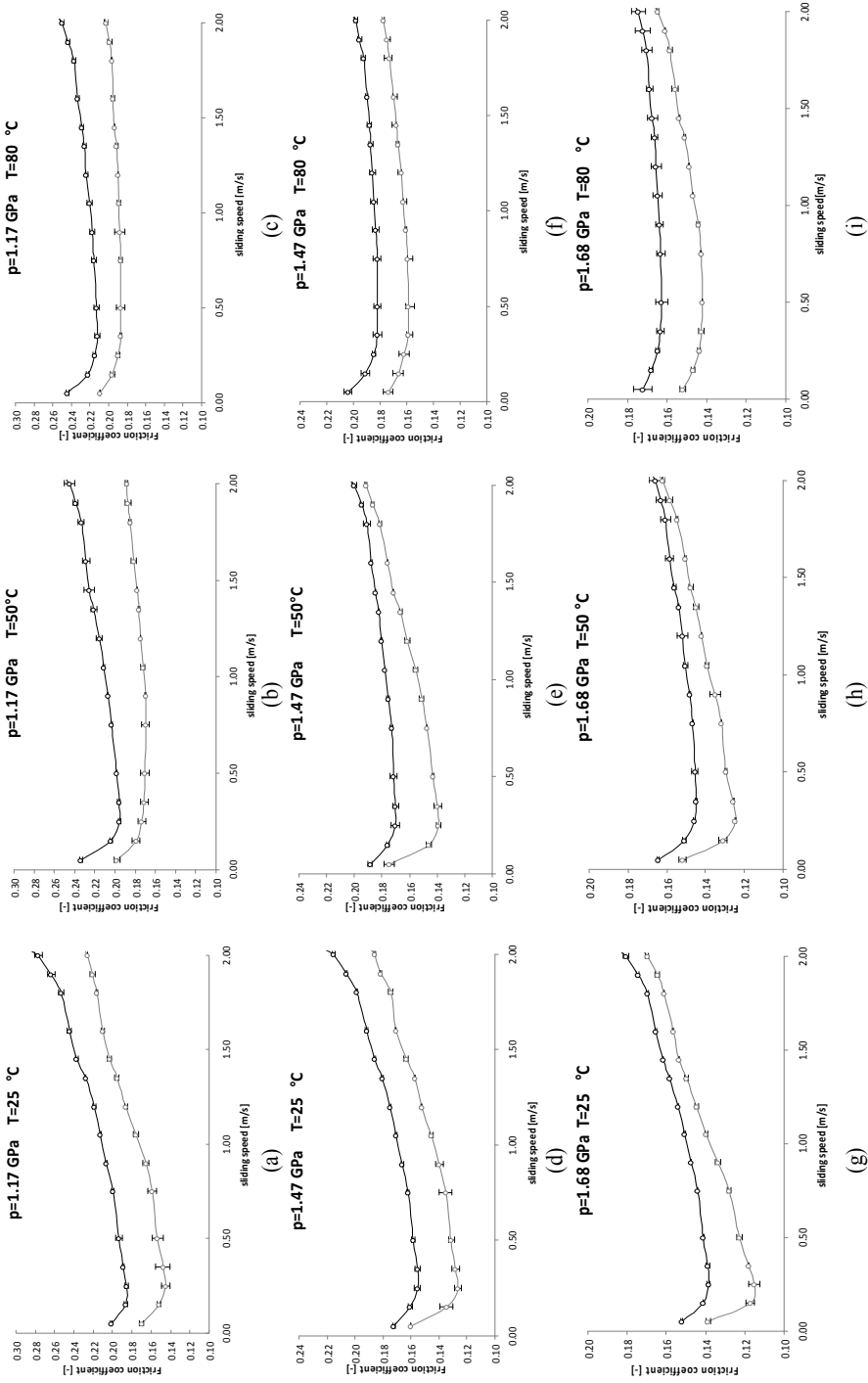
Figure IX.7 *Stribeck curves from sweep-speed tests (SN150 – the curve above, GSN150 – the curve below)*

IX.3.3 Tribological characterization: wear parameter

At the end of each 1-hour steady state test, the worn surface of the steel ball has been measured with an optical microscope to acquire the wear scar diameter (WSD). The WSD values are reported in Tables IX.3-4. According to ISO/IEC Guide 98-3:2008, the wear scar diameter (WSD) results are listed with expanded uncertainty equal to 20 μm, coverage factor k = 2.

The anti-wear property of GO as additive for liquid lubricants has been clearly exhibited in all the lubrication regimes.

Table IX.1 *Friction coefficient in steady boundary and EHL lubrication conditions at 25°C*

Sample	Average hertzian contact pressure 1.68 GPa		
	Oil temperature 25 °C		
	Average friction coefficient at 5.0 mm/s sliding speed **Boundary regime**	Average Friction coefficient at 0.50 m/s sliding speed **EHL regime**	Difference
SN150 – Base oil	0.158	0.142	Benchmark
GSN150	0.136	0.118	-14% -17%

In particular the presence of graphene oxide in the formulated samples, leading to the reduction of the ball wear scar diameter data equal to 12%, 27% and 30% in boundary, mixed and EHL regime, respectively.

Table IX.2 *Friction coefficient in steady boundary and mixed lubrication conditions at 80°C*

Sample	Average hertzian contact pressure 1.68 GPa		
	Oil temperature 80 °C		
	Average friction coefficient at 5.0 mm/s sliding speed	Average friction coefficient at 0.50 m/s sliding speed	Difference
	Boundary regime	**Mixed regime**	
SN150 – Base oil	0.173	0.163	Benchmark
GSN150	0.141	0.139	-18% -15%

IX.3.4 Raman spectra of the worn surface

In Figure IX.9 the Raman spectra of graphite and graphene oxide nanosheets are reported. In particular, in the spectrum of graphite, the most prominent features "Sarno et al.(2013)", the so-called G band appearing at 1582 cm^{-1} and the G' or 2D band at about 2700 cm^{-1}, using 514 nm excitation wavelength, are collected. The G' band at room temperature can be fitted with two Lorentzian lines. A broad D-band due to disorder or edge of a graphite sample can be also seen at about half of the frequency of the G' band (around 1350 cm^{-1} using 514 nm laser excitation). The oxide graphene shows, as expected, an improved D band intensity and flattening of the 2D line and displays a shift to higher frequencies (blue-shift) of a broader G band "Kudin et al (2008)". In Figure IX.9, the Raman Spectrum collected on the ball wear after a 1 hour test at p=1.68 GPa, T=25 °C, v=0.5 m/s (in the following GSN150_1h) is also reported (more than 40 measurements have been collected on the worn surface).

A notable fact is that the G band of this spectrum is located almost at the same frequency as that in graphite, while the G' band exhibits a single Lorentzian feature and D-band results reduced, evidencing a further exfoliation of the GO and the formation of a thin carbon film ("tribo-film") on the wear scar surface.

In Figure IX.10, the Raman spectra of GO, SN150, GSN150_1h, and GO on the ball wear scar after the 1 hour test at p=1.68 GPa, T=25 °C, v=0.5 m/s, are also reported for comparison. For the Raman measurement, of the oil and GSN150_1h, a drop was casted on a glass slide.

Table IX.3 *Wear scar diameter (WSD) after 1-hour boundary and EHL regime test at 25 °C*
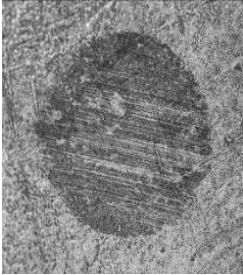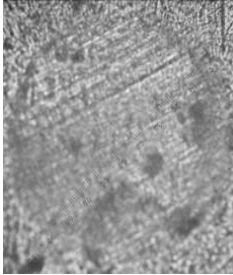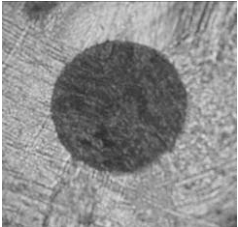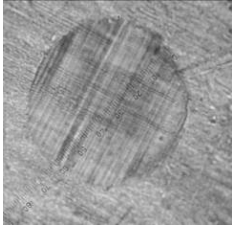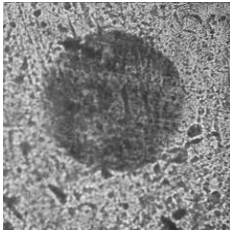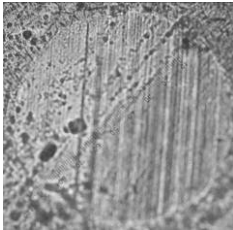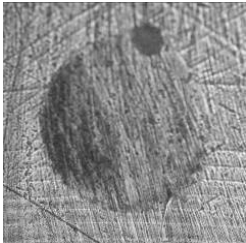
Sample	Average hertzian contact pressure		
	1.68 GPa		
	Oil temperature 25 °C		
	Ball wear scar diameter [µm] at 5.0 mm/s sliding speed	Ball wear scar diameter [µm] at 0.50 m/s sliding speed	Difference
	Boundary regime	**EHL regime**	
SN150 – Base oil	600	900	*Benchmark*
GSN150	530	630	-12% -30%
		Pictures not to scale	

Table IX.4 *Wear scar diameter (WSD) after 1-hour boundary and mixed regime test at 80 °C*

Sample	Average hertzian contact pressure 1.68 GPa		
	Oil temperature 80 °C		
	Ball wear scar diameter [μm] at 5.0 mm/s sliding speed **Boundary regime**	Ball wear scar diameter [μm] at 0.50 m/s sliding speed **Mixed regime**	Difference
SN150 – Base oil	620	910	*Benchmark*
GSN150	540	660	-13% -27%
	Pictures not to scale		

a
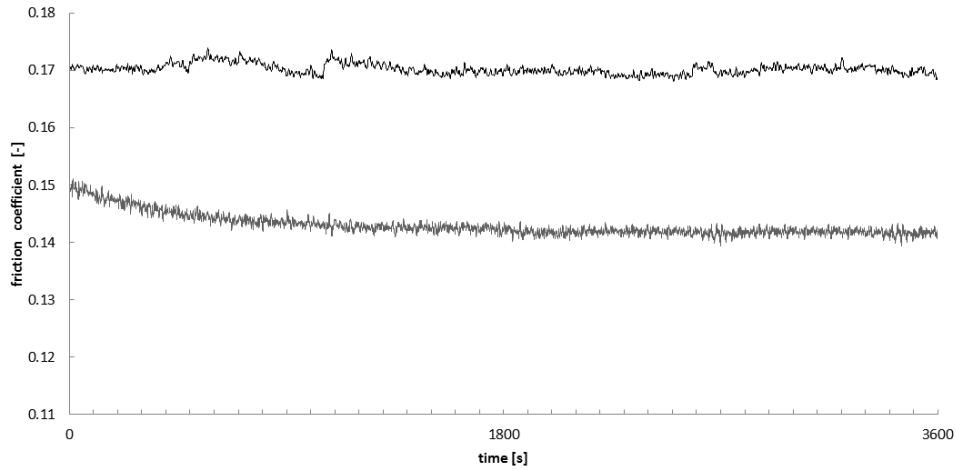
b
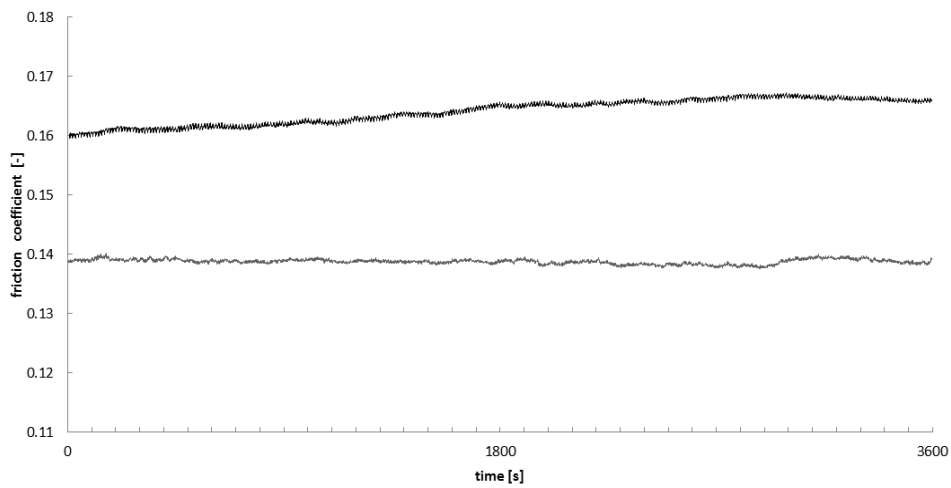
Figure IX.8 *Friction coefficient in 1-hour steady state test with average hertzian contact pressure 1.68 GPa and oil temperature 80 °C: (a) sliding speed 5.0 mm/s, boundary regime; (b) sliding speed 0.50 m/s, mixed regime (SN150 – the curve above, SN150 with 0.01 w.t.% GO – the curve below)*

All the typical D, G, and 2D of carbon can be observed (green arrow in the Figure IX.10) in the spectrum of GSN150_1h, indicating that inside the oil at the end of the 1h test, GO further exfoliated as that found on the ball wear scar (see in particular the presence of the 2D band as shown in the insert of Figure IX.10), is also present.
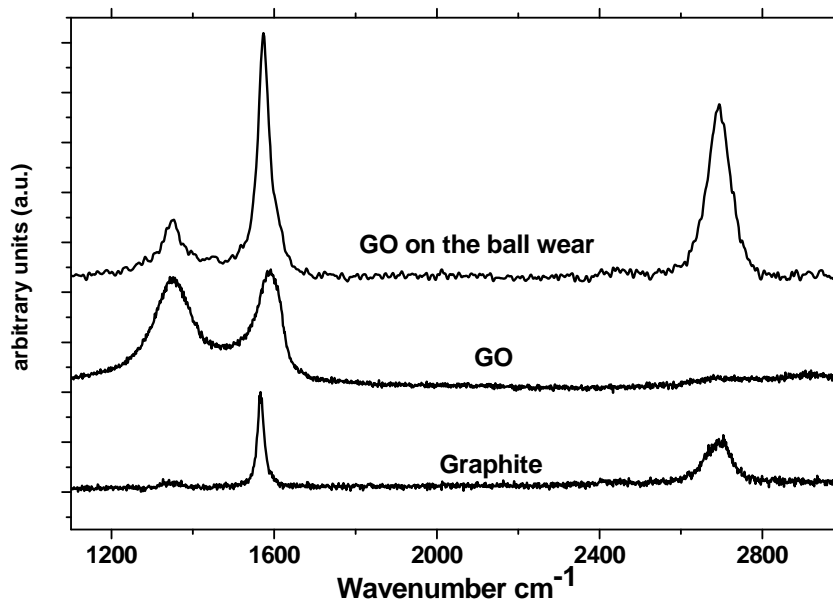
Figure IX.9 *Raman spectra of graphite, GO and further exfoliated GO on the ball wear after 1 hour test at p=1.68 GPa, T=25 °C, v=0.5 m/s.*

IX.3.5 Optical profiler of the rubbed surfaces

Figure IX.11 shows the 3D surface morphologies, obtained by means of an optical profiler with confocal technology, of the rubbed surfaces, tested with pure SN150 (a) and GSN150 (b), after 1 hour test in boundary lubrication regime: p=1.68 GPa, T=25 °C, v=5.0 mm/s. As shown, the rubbed surface after the test with the pure oil is rough with wide and deep furrows together with large and tall ridges. Addition of 0,01% of GO results in a reduced roughness from 552 nm to 424 nm. On the other hand, not only the

roughness is decreased, but the morphology of the wear scar surface has changed, on which it is possible to observe a succession of ridges and valleys of about 15 μm wide.
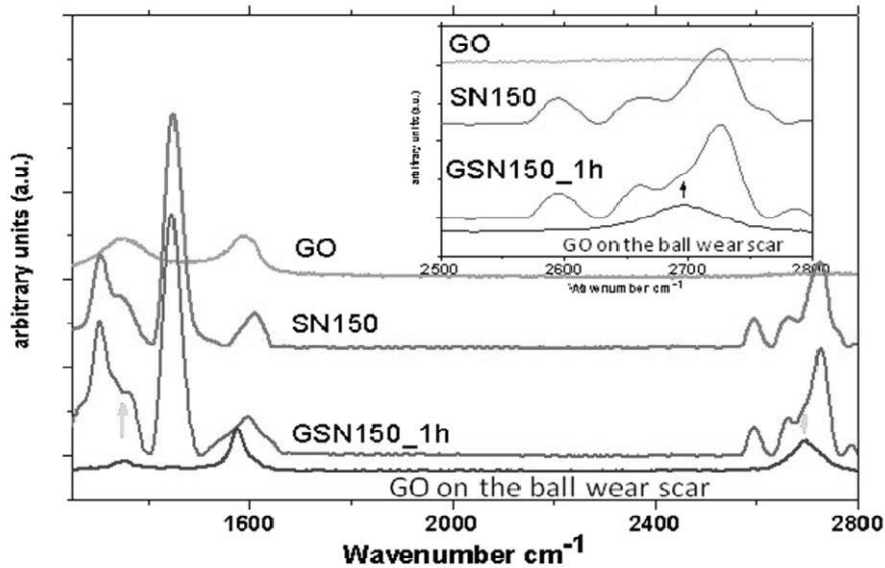
Figure IX.10 *Raman spectra of GO, SN150, GSN150_1h and GO on the ball wear scar after 1 hour test at p=1.68 GPa, T=25 °C, v=0.5 m/s*

To better understand the lubrication mechanisms, the surface of the wear scar after the test with the GSN150_1h has been submitted to a thermal oxidation in air at 200°C for 2h to remove GO.

The roughness so measured is 500 nm (Figure IX.11c), which suggests a GO filling of the deeper valleys and the formation of a thinner film on the asperities, since if the entire surface had been covered with a uniform exfoliated GO thickness, the same roughness would be measured before and after the oxidation. On the other hand, the surface morphology in Figure IX.11b and IX.11c are quite closed.

IX.3.6 Discussion

The incessant literature dispute on the friction reduction mechanism introduced by nanoparticles as lubricant additives finds in the following list the more convincing physical explanations: rolling-sliding "rigid" motions together with flexibility properties "Tevet et al. (2011)", nanoadditive

exfoliation and material transfer to metal surface to form the so called "tribofilm" or "tribolayer" "Yadgarov (2013)", electronic effects in tribological interfaces "Seifert et al. (2000)", surface roughness improvement effect or "mending" "Liu et al. (2004); along with the more classical hypothesis of surface sliding on lower shear stress layers due to weak interatomic forces, valid also for micro-scale additives used from decades.

Our observation of the surface morphologies indicate that the addition of GO considerably leads to smoother surface, by reducing the surface r.m.s. roughness: the tribopair surface sliding on lower shear stress layers due to weak interatomic forces of GO sheets allows modified interaction between the asperities of the tribopair steel parts even from the qualitatively point of view. Exfoliated GO fills the deeper scratches and covers with a thinner film the surface peaks.

The experimental evidences of this paper represent a proof of the presence of a tribological film of reduced graphene oxide which covers the whole worn surface of the steel ball, together with a mending effect "Wintterlin and Bocquet (2009)".

The since-start reduction of friction coefficient in both the Figures IX.7 can be addressed to the surface rubbing through the low shear stress GO layers.

The GO 0.01 w.t.% concentration is quite lower than the usual one for inorganic nanoadditives "Yadgarov et al. (2013)" and carbon nanotubes and in line with previous studies in which oleic acid-modified graphene was used "Lin et al. (2011)". This feature is welcomed in the preparation of fully formulated engine or gearbox lubricants since the GO addition could only slightly modify the delicate equilibrium achieved by oil manufacturers between the essential and ubiquitous additives as antioxidant, viscosity modifier, pour-point depressant and other minors.
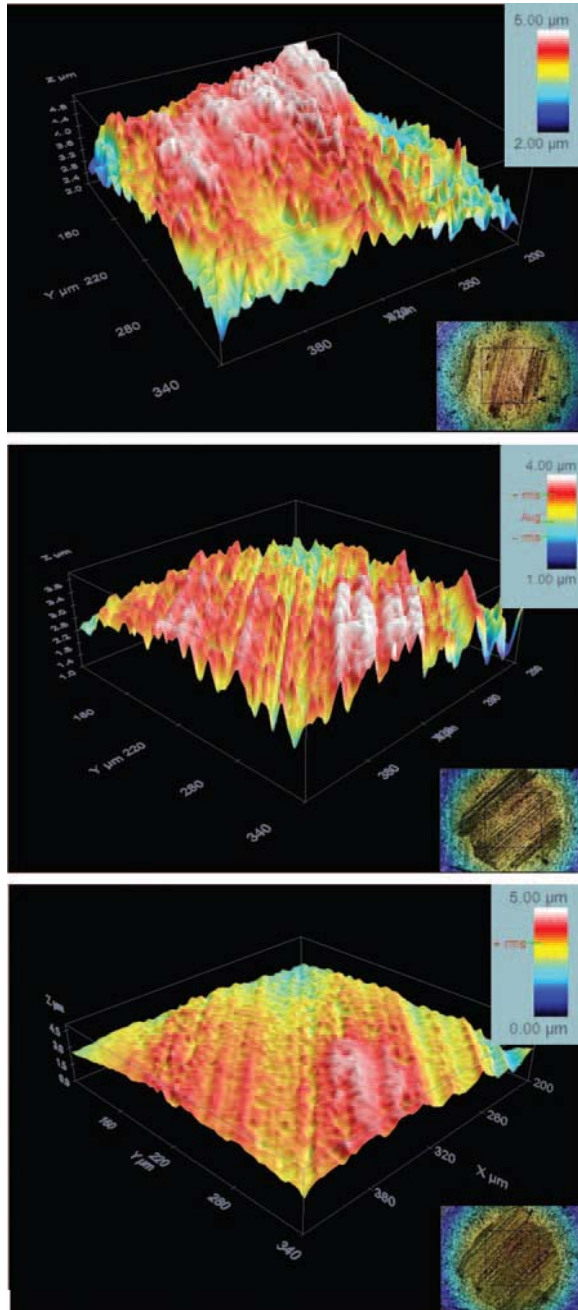
Figure IX.11 *3D surface morphologies of the wear scars: (a) base oil SN150, (b) GSN150, (c) on the same wear scar in (b) after thermal oxidation to remove GO*

133

IX.4 Conclusions

The tribological tests confirm good reduction of friction and wear parameters in boundary lubrication, mixed lubrication and EHL regimes achieved with mineral oils formulated with Graphene Oxide (GO) nanosheets. For instance, with average contact pressure of 1.17 GPa and temperature in the range 25-80 °C, the average CoF decreased by more than 20% compared with the base lubricant value. The sliding tests in steady state conditions have shown an average reduction of CoF equal to 16%. The frictional reduction benefit has been proven at any level of oil temperature, contact pressure and sliding speed.

The best anti-wear result has been observed on the ball surface in the mixed lubrication and EHL regime, with a marked average decreasing around 30%. A tribological film of reduced GO nanosheets after the tribological test covers the ball wear scar.

The good friction and anti-wear properties of graphene sheets may possibly be attributed to their small structure and extremely thin laminated structure, which offer lower shear stress and prevent interaction between metal interfaces.

The results clearly prove that graphene platelets in oil easily form protective deposited films to prevent the rubbing surfaces from coming into direct contact and, thereby, improve the entirely tribological behaviour of the oil.

Chapter X
Experimental VII

Preparation of high quality graphene sheets by a Liquid Phase Exfoliation

X.I Introduction

Among different method for the fabrication of graphene, exfoliation of graphite results to be the much more efficient approach for bulk production of graphene sheets.

A number of papers described the exfoliation of graphite to graphene oxide (GO) "Chen et al. (2010), Eda et al. (2008), Sarno et al. (2013 Accepted)". This material consists of graphene-like sheets, chemically functionalized with compounds such as hydroxyls and epoxides, which stabilize the sheets in water "Stankovicha et al. (2007). However, GO has poor quality and requires reduction, so far this leaves a significant number of defects "Chen et al. (2010), Stankovicha et al.". On the other hand, defect free, unoxidized graphene can be obtained by a non-covalent method. Hernandez et al. "Hernandez et al. (2008)" showed that high-quality monolayer graphene can be produced at significant yields (1 wt%) by non-chemical, liquid-phase exfoliation of graphite by sonication in certain organic solvents.

In this chapter, the production of graphene and multilayer graphene by a liquid phase exfoliation in N-methylpyrrolidone (NMP) was reported. The sonication parameters have been modulated to treat a high concentration graphite solution to obtain an high graphene yield and a one step massive thin sheets production.

X.2 Materials and methods

X.2.1 Materials

The graphite powder used was purchased from Alfa Aesar (microcristalline, -300 mesh, 7% ash). N-methylpyrrolidone was purchased from Sigma Aldrich (spectrophotometric grade> 99.0%).

X.2.2 Sample preparation

Among the number of experiments performed, the best result obtained dispersing graphite in N-methylpyrrolidone (NMP) (cylindrical vial, 10-25 ml solvent) at a concentration of 10 mg/ml for 1 h at the maximum power of ultrasound (Hielscher UP 400S, 400 W, 24 kHz), was reported in the following. The product of sonication was a liquid consisting of a greyish homogeneous phase and containing a number of macroscopic aggregates that can be removed by centrifugation for 90 minutes at 500 rpm.

Graphene and multilayer graphene sheets (G+MLG) were recovered by vacuum filtration of the supernatant solution from centrifugation (the supernatant contains about the 30 wt% of the original graphite - TG evaluation, see the results and discussion section below), onto porous alumina membranes (pore size: 20 nm).

X.3 Characterization techniques

SEM images were captured with a LEO 1525 microscope. TEM images were acquired using a FEI Tecnai electron microscope operating at 200 kV with a LaB6 filament as the source of electrons. The samples for the TEM observation were casted from NMP solution on the TEM grid.
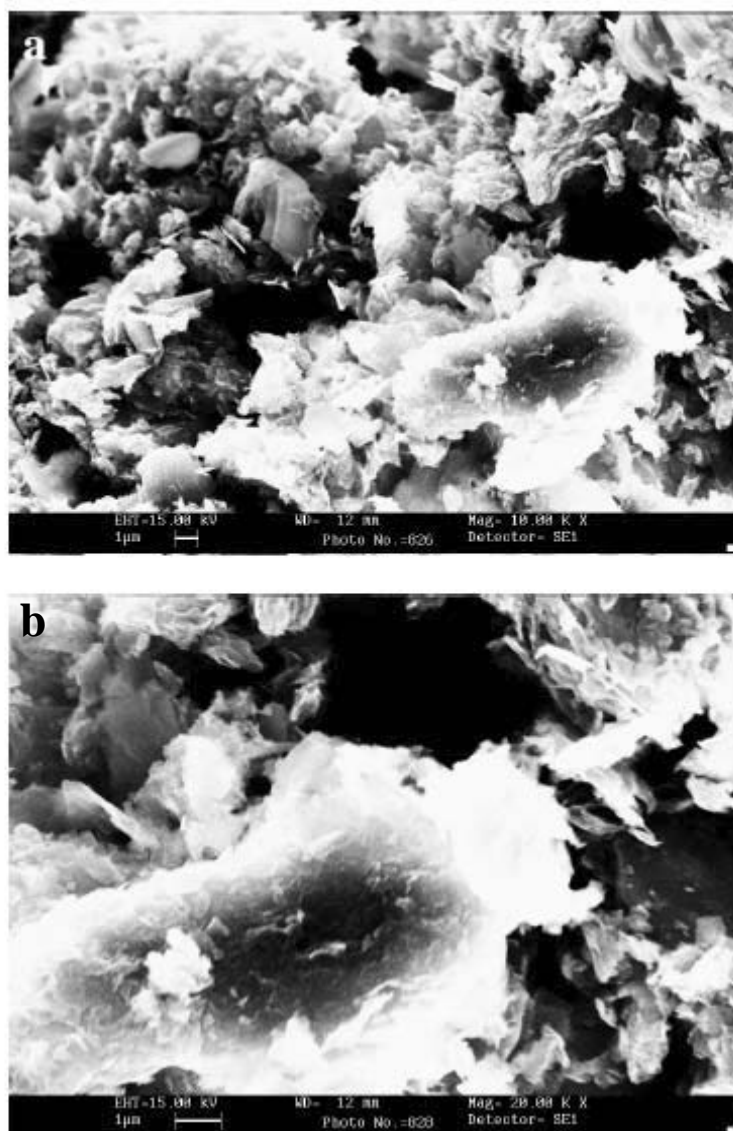
Figure X.1 (a,b) *SEM images of the flakes, of graphene and multilayer graphene sheets, at increasing magnification*

Raman spectra of both the supernatant and precipitate upon centrifugation, casting on a glass slip and NMP drying were obtained at room temperature with a microRaman spectrometer (Renishaw inVia; 514 nm excitation wavelength). About 100 measurements for each sample have been carried out. A number of typical Raman spectra are reported in the figures. The laser spot diameter was 10 μm, a value higher than the size of the obtained flakes.

XRD measurements of the thin carbon film obtained after filtration were performed with a Bruker D8 X-ray diffractometer using CuKα radiation.
The thermal behaviour was investigated with a thermo-analyzer (Q600, TA Instruments) online connected to a quadrupole mass detector (Quadstar 422, Pfeiffer Vacuum). The measurement was carried out in air flow.

X.4 Results and discussion

Scanning electron microscopy (SEM) images at increasing magnification of the flakes obtained are shown in Figure X.1, the powder consists of flakes of few micron in size.
To investigate the state of the material remaining dispersed in the supernatant solution after the centrifugation, TEM images have been obtained by dropping a small amount of the dispersion onto holey carbon grids. Figure X.2 shows two bright-field TEM images, at two different magnifications, of the objects typically observed. The TEM images reveal the presence of flakes of graphene and multilayer graphene sheets in the sample. In all cases, these objects have lateral sizes typically of a few micrometers. In many cases the sheet edges tend to scroll and fold slightly. The corresponding electron diffraction pattern (insert in the green area) and the EDX spectrum (insert in red area) confirm the carbon sp^2 nature of the sheets. The FFT recorded in the blue area evidences different orientations of packed multilayer with the typical interlayer graphite spacing of about 0.34 nm. The high resolution TEM images in the inserts of Figure X.2b permit to count the number of layers of the sheets which edges are in the areas highlighted by colored rectangles: 15 and 12, 2 and 1 in orange, in light green and in yellow, respectively.
 By analyzing a large number of TEM images, paying attention to the uniformity of the flake edges and from a statistic analysis of over 200 objects for each image, we generated sheets thickness statistics as shown in Figure 2c (normalized on 100 objects). From these data the percentage of monolayer graphene was estimated in NMP dispersions, *number of monolayers/total number of sheets observed* equal to 22%, corresponding to a monolayer mass fraction, *mass of monolayers/mass of all sheets observed* of 5.5 wt%, leading to an overall yield of 1.8 wt. % (the supernatant contains about the 30 wt% of the original graphite, TG evaluated see in the following). In Figure X.2d an higher resolution TEM image and the electron diffraction pattern, collected in the pink area of the figure, are also reported. The electron diffraction pattern exhibits the typical sixfold symmetry expected for graphite/graphene "Meyer et al. (2007), Bae et al. (2011)", permitting the definitive identification of graphene in the area in pink.
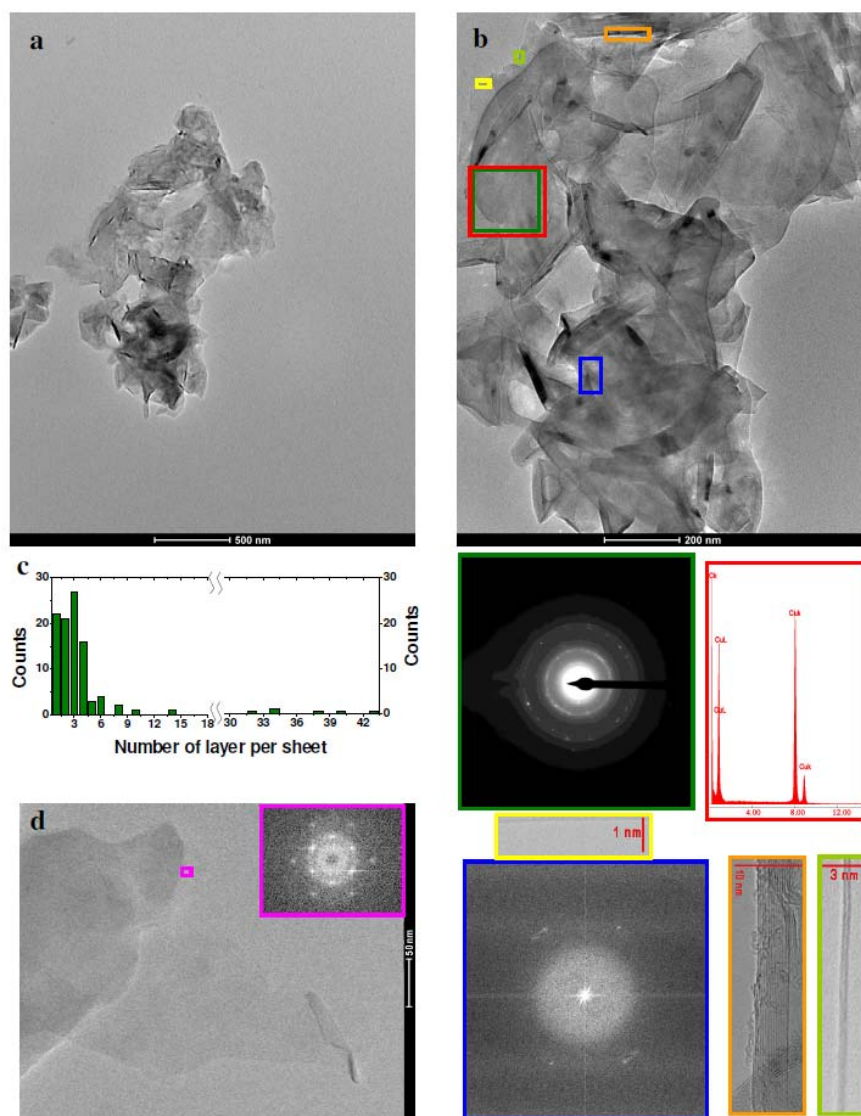
Figure X.2 *TEM images at two different magnifications of graphene and multilayer graphene sheets (a, b). The inserts in Figure 2b are: electron diffraction pattern, in the green area; EDAX analysis, in the red area; FFT in blue area; high resolution TEM images, in orange, light green and yellow areas. Histogram of the number of layer per sheet (c). Higher resolution TEM image and electron diffraction pattern collected in the pink area (d)*
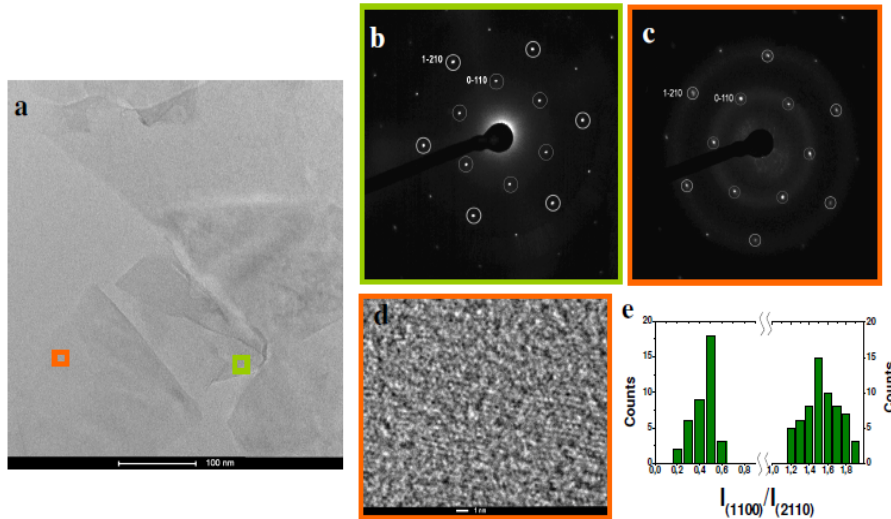
Figure X.3 *TEM image of the graphene and multilayer graphene (a); electron diffraction pattern of multilayers in the green are (b); electron diffraction pattern and high resolution TEM image of a monolayer in the orange area (c,d). Histogram of the intensity ratio I(1100)/I(2110) obtained on 100 thin flakes (c)*

In particular, in Figure X.3a, a TEM image containing several sheets including monolayer, was reported together with the electron diffraction patters obtained in the areas in orange and green respectively. Labelling the two sixfold symmetry with the Miller–Bravais (hkil) indices and considering that for the multilayers, the (2110) spots appear to be more intense with respect to the (1100) spots (computational studies have shown that the intensity ratio for multilayer, with Bernal (AB) stacking, is $I(1100)/I(2110)<1$, whereas for monolayers it is $I(1100)/I(2110)>1$ "Hernandez et al. (2008)" it's possible identify graphene in the orange area and multilayer graphene in the green area. Starting from this considerations, the histogram reported in Figure X.3e was obtained by measuring the diffraction pattern of 100 thin sheets and the relative intensity ratio $I_{(1100)}/I_{(2110)}$, finding that on the respect more thinner sheets, the monolayer fraction is about 40%.
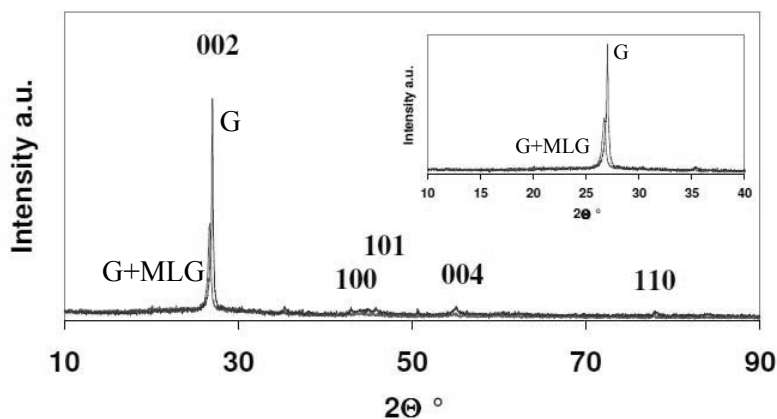
Figure X.4 *X-ray diffraction pattern of the flakes of graphene and multilayer graphene sheets, as recorded on the thin film obtained after vacuum filtration (G+MLG) and of graphite (G)*

The XRD diffraction patterns of graphite and G+MLG obtained, were been compared in Figure X.4, in order to evidence structural changes due to exfoliation treatment, as shown by modification of the characteristic reflection (002). The peak intensity of pristine graphite results higher than that of G+MLG indicating a delamination of the graphite into more thinner graphene and multilayer graphene sheets "Bae et al. (2011)". The downshift from 27.0° to 26.7° 2θ of the (002) reflection indicates a slightly higher interlayer distance (from 3.0 to 3.3 nm) between the graphene layers in the sheets upon the graphite exfoliation.

Figure X.5a shows Raman spectra of the precipitate obtained after the centrifugation and drying. The two most intense features are the G peak at ~1570 cm^{-1} and a band at ~2700 cm^{-1}, named 2D, since it is the second most prominent peak always observed in graphite samples "Casiraghi et al. (2005)". The G peak is due to the doubly degenerate zone center E2g mode "Ferrari et al. (2003)", while the 2D band is the second order of zone-boundary phonons. Such phonons give rise to a peak at about 1350 cm^{-1} due to disorder or edge in graphite, called D band "Ferrari et al. (2003)". The G band for both spectra of Figure X.5a is centered at 1565 cm^{-1}. The 2D band in one case (profile in brown) is that typical of graphite consisting of the two components 2D1 and 2D2, the second with a higher intensity than the first one "Meyer et al. (2007)"; the profile in orange have the same brown width, a flat apex and can be easily deconvolved with almost two peaks. A broad D-band can be seen in both the spectra reported in Figure X.5a.

141

Hernandez et al. "Hernandez et al. (2008)" have demonstrated that this exfoliation process does not introduce any significant structural defect. On the other hand our laser spot diameter was 10 μm, a value higher than the size of the obtained sheets suggesting the presence of edges within the analyzed area. Additionally, the so-called G* band "Malard et al. (2009)" can be seen at 2450 cm^{-1}.
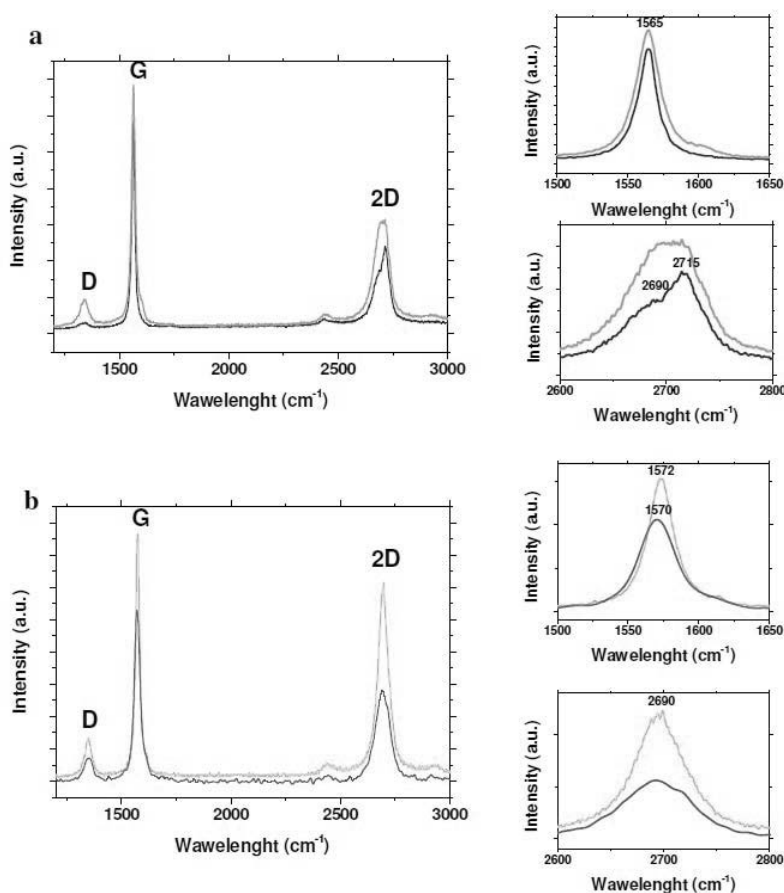
Figure X.5 *Raman spectra of the: centrifugation precipitate (a) and of the flakes of graphene and multilayer graphene in the supernatant after centrifugation (b).*

Spectra in Figure X.5b refer to thin films of G+MLG prepared by vacuum filtration onto alumina of the supernatant. Figure X.5b shows a significant change in shape and intensity of the spectrum collected from the supernatant compared to the precipitate. An up shift of about 7 cm^{-1} of the G band and a

downshift of the 2D band, typical of thinner graphite sheets, was observed "Ferrari (2007)".

The oxidation of pristine graphite and G+MLG after drying can be characterized by thermal analysis in air flow (see Figure X.6). The oxidation occurred as single weight loss step in the temperature range 530–875°C, with a DTG peak centered at 702°C for graphite, that results slightly downshifted to 695°C for MLG. The TG residue of the graphite being due to its original purity degree.
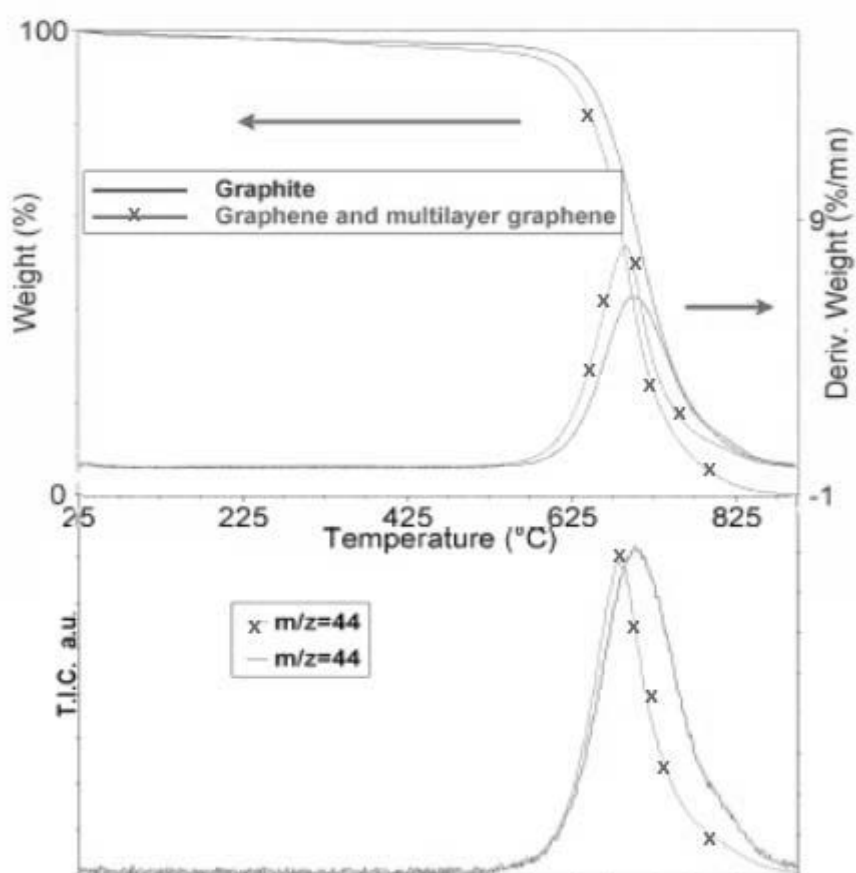
Figure X.6 *TG-DTG and relevant total ion current signals of graphite and G+MLG*

For both the samples the oxidation step was characterized by CO_2 release (see m/z=44), while no fragments from NMP or other impurities can be seen

during the thermogravimetric test indicating the high degree of purity of the obtained sample. The absence of a thermogravimetric residue confirms this result. In Figure X.7 the thermal conversion of NMP was reported, showing a weight loss in the range 25-150°C. The decomposition of the solvent is clearly indicated by the corresponding TIC of the most intense mass fragment peaks (m/z=15, 18, 27, 28, 30, 39, 41, 42, 44, 56, 71, 72, 98, 99). The detector of the spectrometer continues to see the typical fragments of NMP, even after the oxidation event was finished, probably due to the high saturation level of the oxidation chamber.
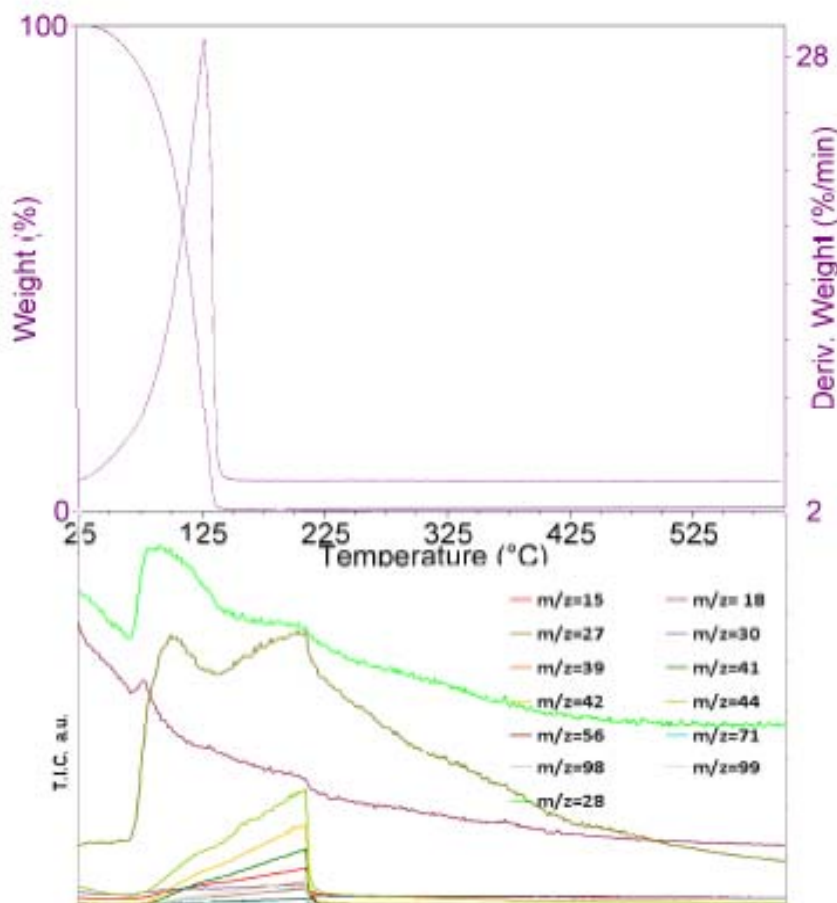
Figure X.7 *TG-DTG and relevant total ion current signals of NMP*

The thermogravimetric profiles of the precipitate before drying was finally reported in Figure 8. It has been used to evaluate the amount of graphitic carbon in the precipitate, previously opportunely weighted, for quantitative evaluation. The TG profile shows two weight loss: the first one, in the temperature range 25-200 °C, due to NMP as confirmed by corresponding TIC of the most intense mass fragment peaks also shown in the figure; the second one due to the graphite content. NMP constitute the 75 wt% of the precipitate, the increased endset temperature observed was probably due to the interaction between the graphite layers and the solvent.
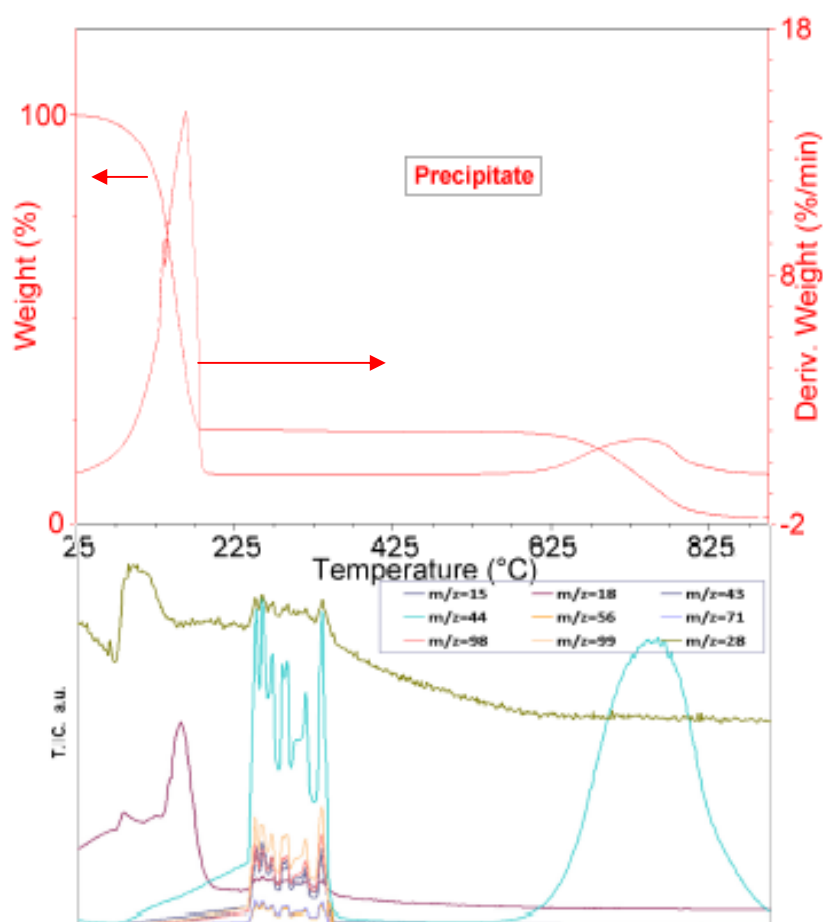
Figure X.8 *TG-DTG and relevant total ion current signals of the precipitate*

X.5 Conclusions

Graphene and multilayer graphene by a liquid phase graphite exfoliation in N-methylpyrrolidone (NMP) have been prepared. The sonication concentration solution, time and ultrasound power have permitted to obtain a one step massive very pure thin flakes production with a monolayer yield of about 1.8 wt.%.

Conclusions

The goal of this thesis work has been to develop industrial scalable processes starting from research at lab scale on graphene formation. Depending on the specific application can be used single- or few-layer graphene. Therefore, alternative techniques for graphene formation have been studied.

(i) The first part of investigation has been addressed to fabrication of high-quality graphene films on Ni foil using CVD at ambient pressure. The reactor geometry and the position of the catalyst in the reactor are very important parameters to control graphene formation. The bottom Ni surface shows an increased carbon deposition with respect to the top surface. This behaviour could be due to carbon diffusion from top to bottom during the synthesis, which results in a greater availability of carbon in the zones adjacent the bottom surface during cooling. An increase of the segregation and precipitation phenomena under Ni thickness increase was observed. In the same operating conditions but cooling rate a lower carbon deposition was observed on both Ni surfaces when the sample remains at high temperature in the first minutes after the synthesis. This indicates a phenomenon of carbon rearrangment in the metal bulk, at this slower cooling rate in the high-temperature region, resulting in reduced the segregation and precipitation phenomena. By decreasing the synthesis time, it is possible to obtain few-layer graphene on the nickel surface, which also contains 1 L on areas showing an increased Ni(1 1 1) diffraction peak intensity, but without homogeneity. By increasing the hydrogen concentration it is possible to control the final graphene formation on the nickel surface, despite the thickness and roughness of the film, the crystallographic orientation of the different zones, the high solubility of carbon in nickel, and the cooling rate. In particular quite uniform 2–3-layer graphene has been obtained on the bottom Ni surface during cooling, leaving no excess carbon.

(ii) Once synthesized, CVD graphene on metal foil (Ni and Cu) was transferred on a suitable substrates (like polymer, silicon wafer, glass), making the technique versatile for many applications.

(iii) Subsequently, stable core-shell carbon-coated GCMNPs have been prepared by catalytic chemical vapor deposition (CCVD) in the presence of methane at atmospheric pressure on a Co/Fe catalyst. Under the

experimental conditions investigated, alumina determines the GCMNP size and was used as a support to obtain very small body-centered-cubic-Co/Fe nanoparticles (4.1 nm mean diameter), with a narrow distribution of diameters.

The total flow rate, hydrocarbon partial pressure and catalyst weight are crucial to the selective coating of the nanoparticles and to the thickness of the coating. Moreover, to obtain homogeneous material, it is fundamental to control as much as possible the diffusive limitations. The use of a carrier prevents unwanted homogeneous decomposition and increases hydrocarbon conversion resulting in GCMNPs covered by two graphene layers and free of other carbon species.

(iv) The influence of the pretreatment conditions (H_2 or N_2) on the final alumina pore size distribution and GCMNPs diameter and magnetic properties of the cobalt and iron nanoparticles were studied. The pretreatment conditions determine the final alumina pore size distribution and, in the experimental conditions explored, the GCMNPs diameter. The pretreatment was performed either in H_2 or in N_2. The nanoparticles magnetic properties have been found strongly dependent by their size. A saturation magnetization value of 230 e.m.u./g, was found, for the monodispersed 4.1 nm diameter body-centered-cubic-FeCo nanoparticles.

(v) The tribological tests confirm good reduction of friction and wear parameters in boundary lubrication, mixed lubrication and EHL regimes achieved with mineral oils formulated with Graphene Oxide (GO) nanosheets.

The good friction and anti-wear properties of graphene sheets may possibly be attributed to their small structure and extremely thin laminated structure, which offer lower shear stress and prevent interaction between metal interfaces.

The results clearly prove that graphene platelets in oil easily form protective deposited films to prevent the rubbing surfaces from coming into direct contact and, thereby, improve the entirely tribological behaviour of the oil.

(vi) Graphene and multilayer graphene by a liquid phase graphite exfoliation in N-methylpyrrolidone have been prepared. The sonication concentration solution, time and ultrasound power have permitted to obtain a one step massive very pure thin flakes production with a monolayer yield of about 1.8 wt.%.

References

- Aleman, B., W. Regan, S. Aloni, V. Altoe, N. Alem, C. Girit, B.Geng, L. Maserati, M.Crommie, F. Wang, A. Zettl, ACS Nano 4 (2010) 4762-4768.
- Altavilla C., Sarno M., Ciambelli P., Chem. Mater. 21 (2009) 4851-4858.
- Al-Temimy A., Riedl C., Starke U., Applied Physics Letters, 95 (2009) 231907.
- Ang K.H., Alexandrou I., Mathur N.D., Amaratunga G.A.J., Haq S., Nanotechnology 15 (2004) 520-524.
- Bae S., Kim H., Lee Y., Xu X.F., Park J.S., Zheng Y., Balakrishnan J., Lei T., Kim H.R., Song Y.I., Kim Y.J., Kim K.S., Ozyilmaz B., Ahn J.H., Hong B.H., Iijima S., Nature Nanotechnology 5 (2010) 574–578.
- Bae S.Y., I.Y. Jeon, J. Yang, N. Park, H. Suk Shin, S. Park, R.S. Ruoff, L. Dai, J.-B. Baek, ACS Nano 5 (2011) 4974–4980.
- Bai, J. and Wang, J.P.Appl. Phys. Lett. 87(2005) 152502 .
- Baraton L., He Z., Lee C.S., Maurice J.L., Cojocaru C.S., Gourgues-Lorenzon A.F., Lee Y.H., Pribat D., Nanotechnology 8 (2011) 085601.
- Berger C., Song Z., Li X., Wu X., Brown N., Naud C., Mayou D., Li T., Hass J., Marchenkov A.N., Conrad E.H., First P. N., de Heer W.A., Science, 312 (2006) 1191–1196.
- Bernan D., Erdemir A., Sumant A. V., Carbon 54(2013) 454.
- Bernardo C.and Trimm D.L., Carbon 14 (1976) 225–228.
- Bhaviripudi S., Jia X., Dresselhaus M.S., Kong J., Nano Lett. 10 (2010) 4128–4133.
- Blake P., Brimicombe P.D., Nair R.R., Booth T.J., Jiang D., Schedin F., Ponomarenko L.A., Morozov S.V., Gleeson H.F., Hill E.W., Geim A.K., Novoselov K.S., NanoLett. 8 (2008) 1704–708.
- Blake P., P.D. Brimicombe, R.R. Nair, T.J. Booth, D. Jiang, F. Schedin, L.A. Ponomarenko, S.V. Morozov, H.F. Gleeson, E.W. Hill, A.K. Geim, K.S. Novoselov, Nano Lett. 8 (2008) 1704–1708.

References

- Boehm H. P., Clauss A., Hofmann U., Fischer G. O., Zeitschrift Für Naturforschung **B 17** (1962) 150.
- Bonaccorso F., Lombardo A., Hasan T., Sun Z., Colombo L., Ferrari A. C., Materials Today, 15 (2012) 564-589.
- Bonaccorso F., Sun Z., Hasan T., Ferrari A.C., Nature Photonics 4 (2010) 611–622.
- Brodie, B.C. Ann. Chim. Phys. 59 (1860) 466–472.
- Bryant P. J., Gutshall P. L., Taylor L. H., Wear 7(1964) 118.
- Bystrzejewski M. and Rümmeli M.H., Polish J. Chem. 81 (2007) 1219–1255.
- Bystrzejewski M., Klingeler R., Gemming T., Buchner B., Rummeli M. H., Nanotechnology 22 (2011) 315606.
- Cai, W., R. D. Piner, F.J. Stadermann, S. Park, M. A. Shaibat, Y.Ishii, D. Yang, A.Velamakanni, S. J. An, M.Stoller, J. An, D. Chen, R.S. Ruoff, Science 321(2008)1815–1817.
- Casiraghi C., A.C. Ferrari, J. Robertson, Phys. Rev. B 72 (2005) 085401.
- Chae S.J., Günes F., Kim K.K., Kim E.S., Han G.H., Kim S.M., Shin H.J., Yoon S.M., Choi J.Y., Park M.H., Yang C.W., Pribat D., Lee Y.H., Adv. Mater. 21 (2009) 2328–2333.
- Chen G., Weng W., Wu D., Wu C., Lu J., Wang P., Chen X., Carbon, 42 (2004) 753–759.
- Chen H., Muller M.B., Gilmore K.J., Wallace G.G., Li D., Advanced Materials 20 (2008) 3557–3561.
- Chen Z., Hong G., Wang H., Welsher K., Tabakman S.M., Sherlock S.P., Robinson J.T., Liang Y., Dai H., ACS Nano, 6 (2012) 1094–1101.
- Chen Z., Ren W., Liu B., Gao L., Pei S., Wu Z.S., Zhao J., Cheng H.M., Carbon 48 (2010) 3543–3550.
- Cho M. H., Ju J. K., Seong J. J. H., Wear 260 (2006) 855.
- Choi D., Choi M.Y., Choi W.M., Shin H.J., Park H.K.,. Seo J.S, Park J., Yoon S.M., Chae S.J., Lee Y.H., Kim S.W., Choi J.Y., Lee S.Y.,. Kim J.M, Advanced Materials 22 (2010) 2187–2192.
- Ciambelli P., Sannino D., Sarno M., Leone C., Lafont U., Diamond Relat. Mater. 16 (2007) 1144–1149.
- Dai L., Chang D.W. , Ba J.B., Lu W., Small 8 (2012) 1122.
- de Parga A.L.V., Calleja F., Borca B., Passeggi M.C.G., Hinarejos J.J. Jr., Guinea F., Miranda R., Phys. Rev. Lett. 100 (2008) 1–4.
- Derbyshire F.J. and Trimm D.L., Carbon 13 (1975) 189–192.
- Dikin D.A., S. Stankovich, E.J. Zimney, R.D. Piner, G.H.B. Dommett, G. Evmenenko, S.T. Nguyen, R.S. Ruoff, Nature 448 (2007) 457–460.

- Dumitrache F., Morjan I., Alexandrescu R., Morjan R.E., Voicu I., Sandu I., Soare I., Ploscaru M., Fleaca C., Ciupina V., Prodan G., Rand B., Brydson R., Woodword A., Diam. Relat. Mater. 13 (2004) 362–370.
- Echtermeyer T.J., Lemme M.C., Baus M., Szafranek B.N., Geim A.K., Kurz H., IEEE Electron Dev. Lett. 29 (2008) 952–954.
- Echtermeyer T.J., M.C. Lemme, M. Baus, B.N. Szafranek, A.K. Geim, H. Kurz, IEEE Electron Dev. Lett. 29 (2008) 952–954
- Eda G., Fanchini G., Chhowalla M., Nat. Nanotechnol. 3 (2008) 270–274.
- Eizenberg M. and Blakely J.M., J. Chem. Phys. 71 (1979) 3467–3477.
- Emtsev K.V., Bostwick A., Horn K., Jobst J., Kellogg G.L., Ley L., McChesney J. L., Ohta T., Reshanov S.A., Roehrl J., Rotenberg E., Schmid A.K., Waldmann D., Weber H.B., T. Seyller, Nature Materials, 8 (2009) 203–207.
- Ferrari A.C., Meyer J.C., Scardaci V., Casiraghi C., Lazzeri M., Mauri F., Piscanec S., Jiang D., Novoselov K.S., Roth S., Geim A.K., Phys. Rev. Lett. 97 (2006) 187401.
- Ferrari A.C., S.E. Rodil, J. Robertson, Phys. Rev. B 67 (2003) 155306.
- Ferrari A.C., Solid State Commun. 143 (2007) 47–57.
- Fonseca F. C., Goya G. F., Jardim R. F., Muccillo R., Carreno N. L. V., Longo E., Leite E. R., Phys Rev B 66 (2002) 104406.
- Forbeaux I., Themlin J., Debever J., Physical Review, B 58 (1998) 16396.
- Gall' N., Rutkov E., Tontegode A., Phys. Solid State 46 (2004) 371–377.
- Gaster R.S., Hall D.A., Nielsen C.H., Osterfeld S.J., Yu H., Mach K.E., Wilson R.J., Murmann B., Liao J.C., Gambhir S.S., Wang S.X., Nat. Med. 15 (2009) 1327–1332.
- Geim A.K. and Novoselov K.S., Nat. Mater. 6 (2007) 183–191.
- Geng J., Jefferson D. A.,. Johnson B. F. G, Chem. Commun. 23 (2004) 2442-2443.
- Grudzinski I.P., Bystrzejewski M., Cywinska M. A., Kosmider A., Poplawska M., Cieszanowski A., Fijalek Z., Ostrowska A., Parzonko A., J. Appl. Toxicol, (2013) DOI 10.1002/jat.2947
- Grudzinski I.P., Bystrzejewski M., Cywinska M.A., Kosmider A., Poplawska M., Cieszanowski A., Ostrowska A., J. Nanopart. Res. 15 (2013) 1835.
- Guéret C., Daroux M., Billaud F., Chem. Eng. Sci. 52 (1997) 815-827.

References

- Hayashi T., Hirono S., Tomita M., Umemura S., Nature 381 (1996) 772-774.
- He C.N., Du X.W., Ding J., Shi C.S., Li J.J., Zhao N.Q., Cui L., Carbon 44 (2006) 2330–2356.
- He, H., Klinowski, J., Forster, M., Lerf, A. Chem. Phys. Lett. 287 (1998)53–56.
- Hernandez Y., Nicolosi V., Lotya M., Blighe F., Sun Z., De S., McGovern I., Holland B., Byrne M., GunKo Y. et al., Nature Nanotechnology, 3 (2008) 563–568.
- Hilton M. R., Bauer R., Didziulis S. V., Dugger M. T., Keem J. M., Scholhamer J., Surf. Coat Technol. 53 (1992) 13.
- Huang H. D., Tu J. P., Gan L. P., Li C. Z., Wear 261(2006) 140.
- Hummers W. S., and Offeman, R. E., J. Am. Chem. Soc. 80 (1958) 1339–1339.
- Hütten A., Sudfeld D., Ennen I., Reiss G., Wojczykowski K., Jutzi P., J. Magn. Magn. Mater. 293 (2005) 93–101.
- Johansson A.S., Lu J., Carlsson J.O., Thin Solid Films 252 (1994) 19–25.
- Juang Z.Y., Wu C.Y., Lu A.Y., Su C.Y.,. Leou K.C, Chen F.R., Tsai C.H., Carbon 48 (2010) 3169–3174.
- Kalin M., Velkavrh I., Vizintin J., Wear 267 (2009) 1232.
- Kang, J., Hwang S, Kim JH, Kim MH, Ryu J, Seo SJ, Hong BH, Kim MK, Choi JB., ACS Nano 6 (2012) 5360-5365.
- Karu A.E., Beer M.J., Appl. Phys. 37 (1966) 2179–2181.
- Katsnelson M. I., *Materials Today*, **10** (2007) 20.
- Kehrer V.J. Jr.and Leidheiser H. Jr., J. Phys. Chem. 58 (1954) 550–555.
- Kim D.K., Zhang Y., Voit W., Rao K.V., Muhammed M., J. Magn. Magn. Mater. 225 (2001) 30–36.
- Kim H., Abdala A.A., Macosko C.W., Macromolecules 43 (2010) 6515–6530.
- Kim K.S., Y. Zhao, H. Jang, S.Y. Lee, J.M. Kim, K.S. Kim, J.H. Ahn, P. Kim, J.Y. Choi, B.H. Hong, Nature 457 (2009) 706–710.
- Kong J., Cassell A.M., Dai H.. Chemical Physics Letters, 292 (1998) 567–574.
- Kong J., Soh H.T., Cassell A.M., Quate C.F., Dai H.J., Nature, 395 (1998) 878–881.
- Kudin K. N., Ozbas B., Schniepp H. C., Prud'homme R. K., Aksay I. A., Car R., Nano Lett. 8 (2008) 36.
- Kumar S., McEvoy N., Lutz T., Keeley G.P., Nicolosi V., Murray C.P., Blau W.J., Duesberg G.S., Chem. Commun. 46 (2010) 1422–1424.

- Lahouij I., Vacher B., Martin J. M., Dassenoy F., Wear 296 (2012) 558
- Lebedeva I.V., Knizhnik A.A., Gavrikov A.V., Baranov A.E., Potapkin B.V., Aceto S.J., Bui P.A., Eastman C.M., Grossner U., Smith D.J., Sommerer T.J., Carbon 49 (2011) 2508–2521.
- Lee Y., Bae S., Jang H., Jang S., Zhu S.E., Sim S.H., Song Y.I., Hong B.H., Ahn J.H., Nano Lett. 10 (2010) 490–493.
- Li X., Cai W., An J., Kim S., Nah J., Yang D., Piner R., Velamakanni A., Jung I., Tutuc E., S. K. Banerjee, Colombo L., Ruoff R.S. Science, 324 (2009) 1312–1314.
- Li X., Cai W., Colombo L., Ruoff R.S., Nano Lett. 9 (2009) 4268–4272.
- Li X., Wang X., Zhang L., Lee S., Dai H., Science, 319 (2008) 1229.
- Li, X., Y.Zhu, W. Cai, M.Borysiak, B.Han, D.Chen, R.D. Piner, L.Colombo, R.S. Ruoff, Nano Lett 9 (2009) 4359-4363.
- Liang G.C., Neophytou N., Lundstrom M.S, Nikonov D.E., Journal of Applied Physics 102 (2007) 054307.
- Liang X., Z. Fu, S.Y. Chou., Nano Letters, 7 (2007) 3840–3844.
- Lightcap I.V., Kosel T.H., Kamat P.V., Nano Letters 10 (2010) 577–583.
- Lin J., Wang L., Chen G., Tribol Lett. 41 (2011) 209.
- Liu G., Li X., Qin B., Xing D., Guo Y., Fan R., Tribol Lett. 17, 961 (2004).
- Lu A.H., Salabas E.L., Schüth F., Angew. Chem. Int. Ed. 46 (2007) 1222-1244.
- Lu W., Liu S., Qin X., Wang L., Tian J., Luo Y., Asiri A.M., Al-Youbi A.O., Sun X., J. Mater. Chem., 22 (2012) 8775-8777
- Ma L.P., Wu Z.S., Li J., Wu E.D., Ren W., Cheng H.M., International Journal of Hydrogen Energy 34 (2009) 2329–2332.
- Maaz K., Mumtaz A., Hasanain S.K., Bertino M.F., J. Magn. Magn. Mater. 322 (2010) 2199–2202.
- Malard L.M., Pimenta M.A., Dresselhaus G., Dresselhaus M.S., Phys. Rep. 473 (2009) 51–87.
- Malard L.M., Pimenta M.A.. Dresselhaus G., Dresselhaus M.S., Physics Report 473 (2009) 51-87.
- Mallick K. K., Shepherd P., Green R. J., J. Magn. Magn. Mater. 312 (2007) 418–429.
- Mattevi, C., G.Eda, S.Agnoli, S.Miller, K. A. Mkhoyan, O. Celik, D. Mastrogiovanni, G. Granozzi, E. Garfunkel, M. Chhowalla,.Adv. Funct. Mater. 19 (2009) 2577–2583.
- McAllister M. J., Li J.L., Adamson D. H., Schniepp H. C., Abdala, A. A.,Liu J., Herrera-Alonso M., Milius D. L.,Car R., Prud'homme R. K., Aksay I. A., Chem. Mater. 19 (2007) 4396–4404.

References

- Meric I., Han M.Y., Young A.F., Ozyilmaz B., Kim P., Shepard K.L., Nature Nanotechnology 3 (2008) 654–659.
- Meyer J. C., A.K. Geim, M.I. Katsnelson, K.S. Novoselov, T.J. Booth, S.Roth, Nature 446, (2007) 60–63.
- Mørup S., Frandsen C., Hansen M. F., Beilstein J. Nanotechnol. 1 (2010) 48–54.
- Mørup S., J. Magn. Magn. Mater. 37 (1983) 39–50.
- Mørup S., Topsøe H., Appl. Phys. 11 (1976) 63–66.
- Mørup S., Topsøe H., Lipka J., J. Phys. Colloq. 37 (1976) C6-287 - C6-290.
- Mrtensson P. and Owman, F., Surface Science, 369 (1996) 126–136.
- Nesper R., Ivantchenko A., Krumeich F., Adv. Funct. Mater. 16 (2006) 296-315.
- Niemeyer C.M., Angew. Chem. Int. Ed. 40 (2001) 4128–4158.
- Nikitenko S. I., Koltypin Y., Palchik O., Felner I.,. Xu X. N, Gedanken A., Angew. Chem. 113 (2001) 4579-4581; Angew. Chem. Int.Ed. 40 (2001) 4447-4449.
- Nikolic M.S., Krack M., Aleksandrovic V., Kornowski A., Förster S., Weller H., Angew. Chem. Int. Ed. 45 (2006) 657719–658018.
- Nobel Physics Laureates (2010)
- Novoselov K. S., Geim A. K., Morozov S. V., Jiang D., Zhang Y., Dubonos S. V., Grigorieva I. V., Firsov A.A., Science, 306 (2004) 666–669.
- Novoselov K. S., Geim A. K., Morozov S. V., Jiang D., Zhang Y., Dubonos S. V., Grigorieva I. V., Firsov A. A., *Science*, **306** (2004) 666.
- Novoselov K.S., Angew. Chem. Int. Ed. 50 (2011) 6986-7002.
- Obraztsov A.N., Obraztsova E.A., Tyurnina A.V., Zolotukhin A.A.. Carbon, 45 (2007) 2017– 2021.
- Olietea P.B., Rojasb T.C., Fernándezb A., Gedankenc A., Koltypinc Y., Palacioa F., Acta Mater. 52 (2004) 2165–2171.
- Oshima C., Itoh A., Rokuta E., Tanaka T., Solid State Communications 116 (2000) 37.
- Park H.J., Meyer J., Roth S., Skákalová V., Carbon 48 (2010) 1088–1094.
- Pimenta M.A., Dresselhaus G., Dresselhaus M.S., Cancado L.G., Jorio A., Saito R., Phys. Chem. Chem. Phys. 9 (2007) 1276–1291.
- Pollard A.J., Nair R.R., Sabki S.N., Staddon C.R., Perdigao L.M.A., Hsu C.H., Garfitt J.M., Gangopadhyay S., Gleeson H.F., Geim A.K., Beton P.H., J. Phys. Chem. C 113 (2009) 16565–16567.
- Presland A.E.B. and Walker P.L. Jr., Carbon 7 (1969) 1–4.

154

- Presland A.E.B., Roscoe C., Walker P.L. Jr., in: J.G. Gregory (Ed.), Proc. Third Industrial Carbon and Graphite Conf., Society of Chemical Industry, London, 1971, p. 116.
- Pumera M., The Chemical Record 9 (2009) 211–223.
- R. L. Fusaro, Wear 53, 303 (1979).
- R.S. Gaster, D.A. Hall, C.H. Nielsen, S.J. Osterfeld, H. Yu, K.E. Mach, R.J. Wilson, B. Murmann, J.C. Liao, S.S. Gambhir, S.X. Wang, Nat. Med. 15 (2009) 1327–1332.
- Ramanathan T., Abdala A. A., Stankovich S., Dikin D. A., Herrera-Alonso M., Piner R. D. et al., Nat. Nanotechnol. 3, 327 (2008).
- Regan W., Alem N., Alemán B., Geng B., Girit Ç., Maserati L., Wang F., Crommie M., Zettl A., Appl. Phys. Lett. 96 (2010) 113102.
- Reina A., Jia X., Ho J., Nezich D., Son H., Bulovic V., Dresselhaus M.S., Kong J., Nano Letters, 9 (2009) 30–35.
- Reina A., Thiele S., Jia X., Bhaviripudi S., Dresselhaus M.S.,. Schaefer J.A, Kong J., Nano Res. 2 (2009) 509–516.
- Rivas J., SXnchez R. D., Fondado A., Izco C., Garcia-Bastida A. J., Garcia-Otero J., Mira J., Baldomir D., GonzXlez A., Lado I., LWpez-Quintela M. A., Oseroff S. B., J. Appl. Phys. 76 (1994) 6564-6566.
- Rosentsveig R., Gorodnev A., Feuerstein N., Friedman H., Zak A., Fleischer N. et al., Tribol Lett. 36 (2009) 175.
- Santra S., Tapec R., Theodoropoulou N., Dobson J., Hebard A.,Tan W., Langmuir 17 (2001) 2900–2906.
- Sarno M., Sannino D., Leone C., Ciambelli P., J. Mol. Catal. A: Chem. 357 (2012) 26-38.
- Sarno M., Sannino D., Leone C., Ciambelli P., J. Nat. Gas. Chem. 21 (2012) 639-646.
- Sarno M., Tamburrano A., Arurault L., Fontorbes S., Pantani R., Datas L., Ciambelli P., Sarto M.S., Carbon 55 (2013) 10-22.
- Sarno M., A.Senatore, C.Cirillo, V.Petrone, P.Ciambelli, J.Nanosci. Nanotechnol 2013 (Accepted)
- Sarno M., C. Cirillo, P. Ciambelli, Chem. Eng. J. 2014 Accepted
- Sarno M., Cirillo C., Ciambelli P., Chem. Eng. Journal (2014) Accepted.
- Schniepp H.C,; Li J.L., McAllister M. J., Sai H., Herrera-Alonso M., Adamson D. H., Prud'homme R. K., Car R., Saville D. A., Aksay I. A., J. Phys. Chem. B 110 (2006) 8535–8539.
- Scott J. H. J. and Majetich S. A., Phys. Rev. B 52 (1995) 12564-12571.
- Seifert G., Terrones H., Terrones M., Jungnickel G., Frauenheim T., Phys. Rev. Lett. 85 (2000) 146.

References

- Seo W.S., Lee J.H., Sun X., Suzuki Y., Mann D., Liu Z., Terashima M., Yang P.C., Mcconnell M.V., Nishimura D.G., Dai H., Nat. Mater. 5 (2006) 971–976.
- Shon Y. S., Dawson G. B., Porter M., Murray R.W., Langmuir 18 (2002) 3880-3885.
- Song L., Ci L., Gao W., P. M. Ajayan, ACS Nano, 3 (2009) 1353–1356.
- Stankovich S., D.A. Dikin, R.D. Piner, K.A. Kohlhaas, A. Kleinhammes, Y. Jia, Y.Wu, S.T. Nguyen, R.S. Ruoff, Carbon 45 (2007) 1558–1565.
- Stankovich S., Dikin D.A., Dommett G.H.B., Kohlhaas K.M., Zimney E.J., Stach E.A., Piner R.D., Nguyen S.T., Ruoff R.S., Nature 442 (2006) 282–286.
- Stankovich, S. D.A. Dikin, G.H.B. Dommett, K.M. Kohlhaas, E.J. Zimney, E.A. Stach, R.D. Piner, S.T. Nguyen, R.S. Ruoff, Nature 442 (2006) 282–286.
- Stankovicha S., D.A. Dikina, R.D. Pinera, K. A. Kohlhaasa, A. Kleinhammesc, Y.Jiac, Y. Wuc, S.T. Nguyen, R.S. Ruoff, Carbon 45 (2007) 1558–1565.
- Starr D.E., Pazhetnov E.M., Stadnichenko A.I., Boronin A.I., Shaikhutdinov S.K., Surf. Sci. 600 (2006) 2688–2695.
- Stoller M.D., Park S., Zhu Y., An J., Ruoff R.S., Nano Lett. 8 (2008) 3498–3502.
- Szabo T., Berkesi O., Forgo P., Josepovits K., Sanakis Y., Petridis D., Dekany I., Chem. Mater. 18 (2006) 2740–2749.
- Tan P., Dimovski S., Gogotsi Y., Philos. Trans. A Math. Phys. Eng. Sci. 362 (2004) 2289-2310.
- Teunissen W., de Groot F. M. F., Geus J., Stephan O., Tence M., Colliex C., J. Catal. 204 (2001) 169-174.
- Tevet O., Von-Huth P., Popovitz-Biro R., Rosentsveig R., Wagner H. D., Tenne R., Proceedings of the National Academy of Sciences, 108 (2011) 19901–6.
- The history of Lonza's graphite powders. Industrial Lubrication and Tribology 27 (1948) 59-69.
- Thiele S., Reina A., Healey P., Kedzierski J., Wyatt P., Hsu P.L., Keast C., Scaefer J., Kong J., Nanotechnology 21 (2010) 015601.
- Tian J. and Xue Q. J., Tribol Int. 30, 571 (1997).
- Vaari J., Lahtinen J., Hautojärvi P., Catal. Lett. 44 (1997) 43–49.
- Van Bommel A.J., Crombeen J.E., Van Tooren A., Surface Science, 48 (1975) 463–472.
- Viculis L., Mack J., Kaner R., Science, 299 (2003) 1361.
- Wang X., Zhi L.J., Mullen K., Nano Letters 8 (2008) 323–327.

156

- Wang X., Zhi L.J., Tsao N., Tomovic Z., Li J.L., Mullen K., Angew. Chem. Int. Ed. 47 (2008) 2990–2992.
- Wanga S., Huanga X., Hea Y., Huanga H., Wub Y., Houc L., Liua X., Yanga T., Zoub J., Huanga B., Carbon 50 (2012) 2119–2125.
- Wei Z., Ming Z., Hongwei Z., Yu T., Kunlin W., Jinquan W.et al., J. Phys. D Appl. Phys. 44, (2011) 205303.
- Williams G., Seger B., Kamat P.V., ACS Nano 2 (2008) 1487–1491.
- Wintterlin J. and Bocquet M.L., Surf. Sci. 603 (2009) 1841–1852.
- Wu Z.S., Pei S., Ren W., Tang D., Gao L., Liu B., Li F., Liu C., Cheng H.M., Advanced Materials 21 (2009) 1756–1760.
- Yadgarov L., Petrone V., Rosentsveig R., Feldman Y., Tenne R.,. Senatore A, Wear 297, 1103 (2013).
- Yazyev O.V., Katsnelson M.I., Physical Review Letters 100 (2008) 047209.
- Yi D.K., Selvan S.T., Lee S.S., Papaefthymiou G.C., Kundaliya D., Ying J.Y., J. Am. Chem. Soc. 127 (2005) 4990–4991.
- Yu Q., Lian J., Siriponglert S., Li H., Chen Y.P., Pei S.S., Appl. Phys. Lett. 93 (2008) 1–3, 113103.
- Zhang Y., Gomez L., Ishikawa F.N., Madaria A., Ryu K., Wang C., Badmaev A., Zhou C.J., Phys. Chem. Lett. 1 (2010) 3101–3107.
- Zhu X.Y.and White J.M., Surf. Sci. 214 (1989) 240–256.
- Zhu Y., Murali S., Cai W., Li X., Suk J. W., Potts J. R., Ruoff R. S., Adv. Mater., 20 (2010) 1–19.
- Zhu Y., Murali S., Cai W., Li X., Suk J. W., Potts J.R., Ruoff R.S., Adv. Mater. 22 (2010) 3906–3924.
- Zola D., Polichetti M., Senatore C., Pace S., Phys Rev. B 70 (2004) 224504.